MULTIPHYSICS ANALYSIS AND OPTIMIZATION OF 3 DIMENSIONAL PRINTING TECHNOLOGY USING NANO FLUIDIC SUSPENSIONS

by

Salil S. Desai

B.S. in Mechanical Engineering, University of Bombay (Mumbai), 1998

M.S. in Industrial Engineering, University of Pittsburgh, 2001

Submitted to the Graduate Faculty of

the School of Engineering in partial fulfillment

of the requirements for the degree of

Doctor of Philosophy

University of Pittsburgh

2004

UNIVERSITY OF PITTSBURGH

SCHOOL OF ENGINEERING

This dissertation was presented

by

Salil S. Desai

It was defended on

June 8, 2004

and approved by

Dr. Bopaya Bidanda, Professor and Chairman, Industrial Engineering

Dr. Marlin Mickle, Professor, Electrical Engineering

Dr. Laura Schaefer, Assistant Professor, Mechanical Engineering

Dr. Ming En Wang, Assistant Professor, Industrial Engineering

Dissertation Director: Dr. Michael Lovell, Associate Dean for Research and
Associate Professor, Industrial & Mechanical Engineering

ABSTRACT

MULTIPHYSICS ANALYSIS AND OPTIMIZATION OF 3 DIMENSIONAL PRINTING
TECHNOLOGY USING NANO FLUIDIC SUSPENSIONS

Salil S. Desai, PhD

University of Pittsburgh, 2004

Fabrication of micro and nano devices is of prime significance to the area of Micro-Electro-Mechanical Systems (MEMS). Attempts have been made to accommodate high performance devices in compact units, thus reducing their overall size. There exist a variety of microfabrication techniques including lithography, chemical vapor deposition, and LIGA that are used today. Manufacturing costs associated with these processes can be prohibitive due to cycle time and the precious material loss that occurs during etching operations. These drawbacks become more significant problem when building curved traces and support structures that most occur in 3D space.

To address the problems associated with building 3-dimensional circuits and devices in free space, a unique manufacturing process has been developed. This process utilizes conductive Nano-Particulate Fluid Jets (NPFJ) that are deposited onto a substrate by a Continuous Inkjet (CIJ) printing methodology. In this method, a fluid jet consists of colloidal suspensions of conductors and carrier fluids that are deposited onto a substrate and later sintered at high temperatures to form a homogeneous material. The major contribution of the present research is

the investigation, development and optimization of the NPFJ. In this work, a Computational Fluid Dynamics (CFD) model has been developed to simulate the fluid jet and CIJ process. The modified CIJ printing process involves interaction of three domains namely, electrostatics, structural and fluidics. A coupled field analysis of the piezoelectric membrane that exists in the CIJ print head is conducted to establish the perturbation characteristics applied to the fluid. Interaction of the above three domains is captured within a single model using a (FSI) fluid-structural algorithm which staggers between domains until convergence is attained. A Design of Experiments approach was used to determine trends for the drop formations based on various exciting parameters. Results from these simulations have been validated using an ultra-high-speed camera featuring exposure/delay times from 100 nanoseconds at full sensor resolution.

The results of present research will give manufacturers the freedom to construct 3D devices and circuits that conform to the desired shapes and sizes of products, rather than being limited to present 2D components such as printed circuit boards.

DESCRIPTORS

3D Printing	CFD
Coupled Field	Design of experiments
Finite Element	Multiphysics
Nano Particulate	Optimization
Response Surface	Ultra-high speed photography

TABLE OF CONTENTS

LIST OF TABLES

LIST OF FIGURES

ACKNOWLEDGEMENTS

It gives me immense pleasure and gratitude to thank Dr. Michael Lovell for entrusting me with a challenging research project. This Ph.D. degree and dissertation would not have been possible without his generous support during the most critical phase of my doctoral program.

I would like to thank Dr. Bidanda for his mentoring towards my academic career and professional development. I would like to express my deep sense of gratitude towards Dr. Mickle whose visionary ideas have kindled innovative inspiration within me. I would also like to thank Dr. Laura Schaefer and Dr. Alex Wang for their valuable comments and critique. I am thankful to Dr. James T. Cain, Executive Director - Swanson Center for Micro and Nano Systems for the financial support of this research over the past year.

I would like to thank my wife Yogeeta for her unwavering support and constant encouragement all along my Ph.D. sojourn. Special thanks to Mr. Stephen Heston, Junfeng Mei, Joshua Maina and Randolph Maruschock for their contributions and assistance during the experimentation phase. I would like to extend my thanks to the fellow researchers and staff for providing a vibrant research atmosphere. Finally, I am grateful to my parents for their love and understanding.

1.0   INTRODUCTION

Fabrication of micro and nano devices is of prime significance to the area of Micro-Electro-Mechanical Systems (MEMS). Attempts have been made to accommodate high performance devices in compact units thus reducing the overall size of the product. Microfabrication is the research area for developing technologies to manufacture such devices.

Microfabrication is among the top priority research areas in the United States and will continue to be so during the next decade [1]. Federal agencies such as National Aeronautics and Space Agency (NASA), National Science Foundation (NSF), U.S. Department of Defense (DOD), Defense Advanced Research Project Agency (DARPA) have identified MEMS as the "Core Enabling Technology of the Future" and blessed it with substantial research funding [2]. In addition to the U.S. Government funding, U.S. industry investments in MEMS research, development and production capability are currently estimated to be over $100 million per year. Most of the industrial R&D investments are directed towards applications of replacing conventional technology (e.g., data storage, fluid regulation, optical switches, etc.) with a comparable MEMS device in order to reduce cost, increase functionality, and improve reliability [3]. The Japanese and European Governments have invested around $600 million a year for MEMS R&D [4]. Growth of MEMS opportunities continues at an accelerated pace, as microfabrication technology is applied to a wider range of industrial, medical and scientific

applications. Market projections of $10 billion by the end of 2003 to $30 billion by 2004 are an indication of the potential for this far-reaching technology [4].

1.1   TECHNOLOGY OVERVIEW

Micro-Electro-Mechanical Systems (MEMS) is the integration of mechanical elements, sensors, actuators, and electronics on a common silicon substrate through microfabrication technology [5]. In the last few decades, miniaturization has been an important aspect in the development of technology. Smaller components make the systems faster, more reliable, cheaper and capable of incorporating more complex functions. These miniature parts also tend to be rugged, respond rapidly, use minimal power, occupy compact spaces, and are often economical than conventional macro parts. One of the main goals of miniaturization through microengineering is to be able to integrate the well-developed technology in microelectronic circuitry into the novel technology in micromachined three-dimensional structures, in order to produce completely integrated Micro-Electro-Mechanical Systems (MEMS).

MEMS have found applications in diverse areas ranging from avionics, inertial sensors, micro-optics, RF microchips, automotive safety and sensory equipment, space applications, biochips for detection of hazardous chemical and biological agents, and microsystems for high-throughput drug screening to name a few. Many MEMS are geometrically complicated, electro-mechanically coupled, and inherently three-dimensional. The solution of multi-domain physics problems includes electrical, mechanical, chemical, magnetic, thermal, and fluidic effects, which need to be accurately simulated to correctly predict device performance.

The strategy in advancing MEMS technologies is to continue the movement towards greater levels of integration. The motivation is to reduce cost, achieve unprecedented levels of system functionality, and to push further the performance levels enabling vast new application areas. Figure 1 shows a miniature gear at the claws of an ant [6].

Figure 1: Eye catching example of an ant holding a LIGA fabricated gear in its claw

1.2 PROBLEM STATEMENT

There exists a variety of microfabrication techniques such as lithography, dry etching, wet etching, chemical vapor deposition, bulk micromachining, LIGA, etc. in use today. Many are

largely borrowed from the integrated circuit industry, in addition to a few others developed specifically for silicon micromachining.

Lithography is a photographic process for the printing of images onto a layer of photosensitive polymer (photoresist) that is subsequently used as a protective mask against etching. Wet and dry etchings, including deep reactive ion etching, form the essential process base to selectively remove material. Figure 2 [7] shows the basic process flow in micromachining; layers are deposited, photoresist is lithographically patterned, and then used as a mask to etch the underlying materials. The process repeats until completion of the microstructure.
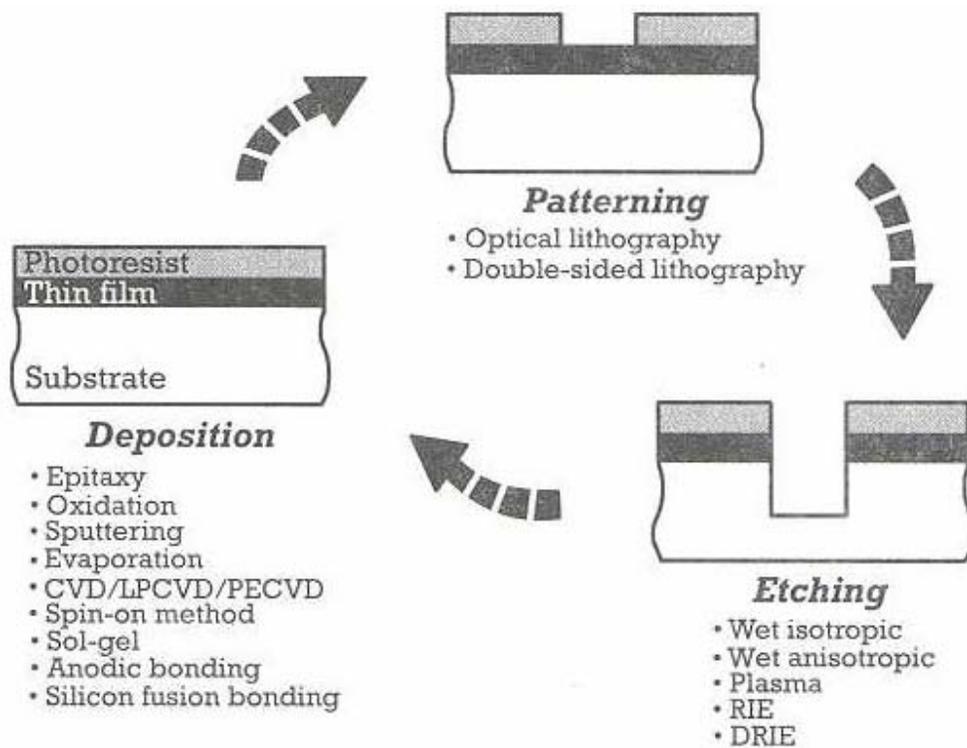
Figure 2: Illustration of basic process flow in micromachining

The above techniques are limited to building 2D circuits and resulting devices. Moreover there is a high turnover time associated between drafting the CAD drawing and obtaining the finished device. Manufacturing costs can be prohibitive due to precious material loss during etching operations. Chemical pollutants are a serious environmental concern during etch disposal. Pre and post processing operations make it a cumbersome and time consuming process [8]. The above-mentioned issues limit application of lithography based technologies for high production rates. The problem gets aggravated when an additional third dimension is accounted for, during manufacturing the devices. Issues regarding building of curvatures in 3D space and support structures to hold the circuits or devices in place have limited research work to the 2D space.

Rapid prototyping (RP) is a popular 3D additive technology. RP technologies such as FDM, 3D Printing, SLA, etc., have limitations in the size of components manufactured. There has been limited success to manufacture micro devices due to process limitations. Moreover being a progressive layered freeform prototyping technology limits its rate of production. There have also been shortcomings on the material usages to build multiple material components.

A research team at Media Lab - MIT, has demonstrated use of an inkjet printer for printing conductive traces in 2D [9]. Researchers at Xerox Palo Alto Research Center use an Ultrasonic beam for Acoustic Printing [10]. The former is limited to 2D surfaces while the later is confined by use of aqueous and wax based inks.

Though MEMS have received significant attention and numerous microfabrication techniques attempted, its fabrication still lies in the embryonic stage. Building 3 dimensional circuits and devices using additive Nano Particulate Fluid Jets (NPFJ) is a unique way of

addressing the above issue. This research fathoms a direct write technology extending the Continuous Inkjet (CIJ) printing concept for MEMS fabrication.

1.3   RATIONALE FOR A 3D MICROFABRICATION TECHNOLOGY

With pressing needs to develop 3D microfabrication techniques, a novel method is proposed for MEMS and other miniaturized devices. The current research will focus on developing a printing technology to build 3 dimensional devices in free space. The method is to develop a fluid jet system, which deposits nanoscale materials in a fluid on a substrate. The fluid jet consists of colloidal suspensions of conductors depending on the device to be built. These materials will be deposited on a substrate and sintered at high temperatures to form a homogeneous material. There are added benefits of using nano particulate fluids over micro sized fluid suspensions. The proposed delivery technique is a modified CIJ system with a micron-sized orifice. It has been observed with experimentation that micro sized particles tend to agglomerate and clog the orifice impending fluid delivery. The use of a nano particulate colloid resolves this problem. Also the melting point for nano-sized materials is as low as 1/10 the temperatures for macro-sized materials. The inter-particulate voids for these materials are minimal enabling them to bond readily into a homogeneous material at far lower temperatures as compared to macro-sized materials.

Working devices such as 3D microchips conforming to the products shape can be built. Such a versatile technique will assist in compressing the space requirements for devices within a product. The critical component of this technology is investigating, developing and optimizing

the NPFJ. To this effect a Computational Fluid Dynamics (CFD) model is developed to simulate the fluid jet and optimize the process parameters for optimal print quality.

1.4   RESEARCH OBJECTIVE

The principal objectives of this research are:

- Develop a Coupled-Field Finite Element model of the Piezoelectric disc within the print head to establish the perturbation characteristics applied to the fluid

- Capture the interaction of the three domains within the CIJ print head namely, electrostatics, structural and fluidics with a Multiphysics model

- Develop a Computational Fluid Dynamic (CFD) model of the drop formation mechanism

- Conduct ultra high speed photographic experiments to validate the CFD model

- Utilize Design of Experiments to investigate input parameters that affect droplet formations

- Optimize significant input parameters based on a Response Surface Methodology for optimal print quality

1.5   RESEARCH CONTRIBUTION

The development of a 3D printing technology using Nano Particulate Fluid Jets (NPFJ) requires a detailed understanding of the interaction of different fields within the CIJ system. This research will aid in explaining the coupled-field behavior of the piezoelectric disc under static and transient input conditions. A Multiphysics analysis is conducted that explores the Fluid-Structural Interaction (FSI) between the PZT disc and fluid media such as water, Methyl Ethyl

7

Ketone (MEK) and a nano particulate fluid suspension. The PZT displacement from the Multiphysics analysis is superimposed on a Computational Fluid Dynamic analysis to shed light on the drop formation mechanism.

Ultra-high speed photographic experiments are conducted to identify the significant factors affecting droplet volume and velocity. A Response Surface design is used to optimize the droplet volume based on significant input parameters. The above research compliments numerical simulation and experimental insights to give a detailed understanding of the droplet formation mechanism in the CIJ printing method. These results will lend ability to fine tune the proposed 3D printing technology to print nano fluidic suspensions.

2.0   LITERATURE REVIEW

Fabrication is a critical issue for MEMS based products. The best a MEMS based product can achieve is the performance of its MEMS components [10]. Thus if the MEMS part is unreliable, it could render the entire product inoperable. Currently MEMS manufacturing technology is the most underdeveloped segment of the entire MEMS field [11]. Existing MEMS fabrication technologies have major shortcomings, which jeopardize their successful commercialization. MEMS based technologies derive their genesis from microelectronics fabrication technology. Microelectronics fabrication is 2D while MEMS is a 3D process [10]. The mechanical properties unimportant to microelectronics are vital to MEMS fabrication. A Complementary Metal Oxide Semiconductor (CMOS) fabrication process is independent of the circuit under manufacturing (product); while a MEMS process must be custom designed for a specific product [10]. Therefore, innovative techniques are needed for the fabrication processes to achieve the goal of making complex and reliable MEMS devices inexpensively. This chapter presents an overview of the evolution of the Microfabrication techniques.

2.1   HISTORY OF MICROFABRICATION

Microfabrication has its root embedded in the manufacture of Integrated Circuits (IC) and transistors around 1950's. The genesis of MEMS technology, spurred out of a presentation given

9

by a brilliant physicist, Dr. Richard Feynman [12]. On December 26, 1959 at the California Institute of Technology, Dr. Feynman tried to incite interest in the development of "innovative miniature fabrication techniques for micromechanics". Eventually in 1969 Westinghouse developed the first Resonant Gate FET. The next step occurred in the 1970s when bulk etched silicon wafers were used as pressure sensors [13].

In 1982 Kurt published an important reference for silicon's materials properties as well as etching data called "Silicon as a Structural Material" [12]. The first actuators produced by microfabrication were electrostatic comb drivers and micro positioning disk drive heads.

In the early 1990's, Government agencies such as DARPA, Air Force Office of Scientific Research (AFOSR), National Institute of Standards and Technology (NIST) supported research in materials, micromachining and application of MEMS based technologies.

2.2   EXISTING MICROFABRICATION TECHNIQUES AND LIMITATIONS

2.2.1   Bulk Micromachining

Bulk Micromachining is the process in which the design is etched out of the bulk of the silicon substrate. This technique allows one to selectively remove material to form membranes, holes, trenches, or other structures on one side of a wafer. Bulk micromachining can be broken down into two types, wet and dry, depending on the etching medium being used.

2.2.2   Wet Micromachining

Wet micromachining is done using liquid etchants, such as alkali hydroxide (KOH). The wet etching occurs by dipping the silicon into a bath of etchant or spraying the wafer with

etchants [14]. There are two categories for etching, isotropic etching and anisotropic etching. In isotropic etching, the chemical eats away at the material at the same rate in every direction. In anisotropic etching, different silicon crystalline planes are etched at different rates. Figure 3 below shows the Anisotropic Wet Etching of Silicon [15].
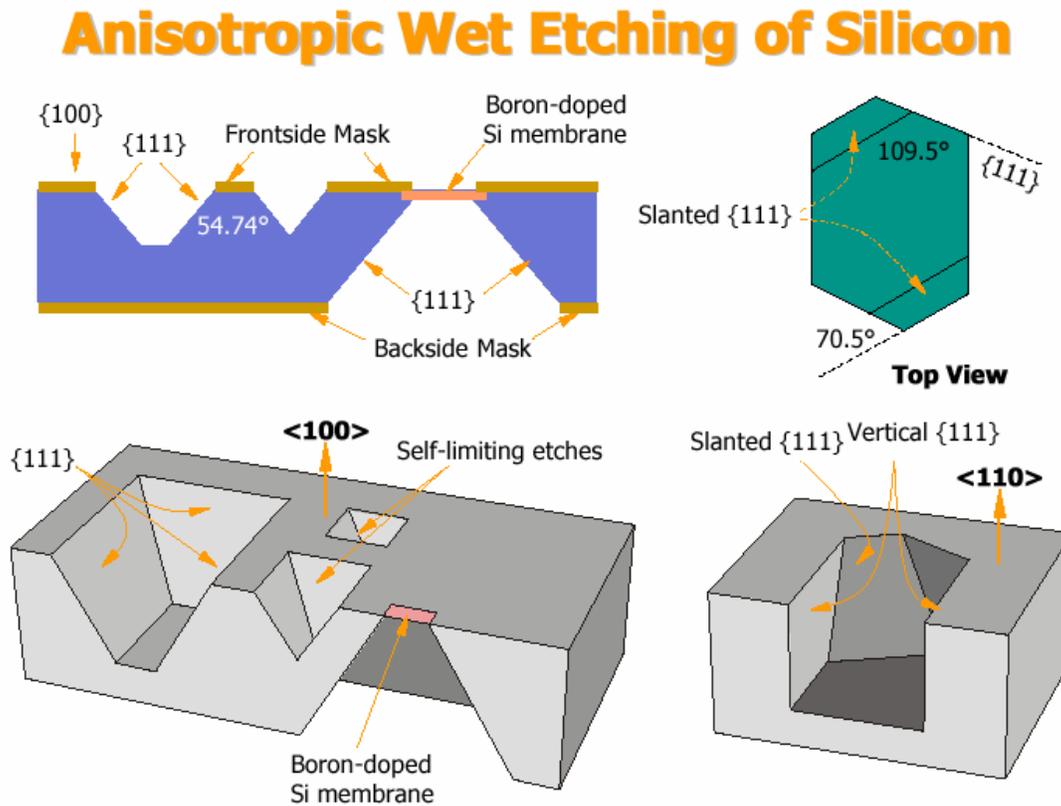
Figure 3: Anisotropic Wet Etching Process

2.2.3   Dry Micromachining

Dry micromachining involves etchants consisting of vapors and plasmas. This etching occurs through chemical or physical interactions between the gas and the silicon. In most cases, fluorine-based gases (CF4, SF6) react with the exposed silicon surface, forming SiF2 or other compounds, which evaporate and are pumped away [13]. The dry etching process is used more

often because it can create more flexible geometry and has less chemical contamination when compared to the wet etching. The most popular form of dry etching is reactive ion etching (REI), which works by accelerating ions towards the material [13]. The material is then etched due to the ions and in the direction of their travel. REI is an anisotropic type of etching that creates "deep trenches and pits (up to ten or a few tens of microns) of arbitrary shape and with vertical walls". Figure 4 shows a DREI process.

Figure 4: Deep Reactive Ion Etching (DRIE) process

The advantage of using a dry anisotropic etching technique is that REI is not limited to certain shapes because of the crystalline structure and makeup of the wafer. Dry etching is more compatible with typical electronics processing than wet etching. In many cases, dry etching was developed specifically for electronics circuit applications.

2.2.4   Surface Micromachining

Surface Micromachining, unlike bulk machining, does not shape the silicon. Rather, it builds layers on the surface of the silicon. The process commonly begins by placing two layers of material on the silicon wafer. The layers are a structural material, usually polysilicon, and a sacrificial material, usually oxide. Both of these "are deposited and dry etched in sequence" then sacrificial material is wet etched away to release the structure". More layers can be added to the structure but more layers only add to the complexity of the structure and the difficulty of producing the structure.

When compared to surface micromachining, the dimensions of bulk machining are relatively smaller. One of the main advantages of this process is the ease to which it can be used with the microelectrical components of MEMS. Typical materials that are used in surface micromachining are Silicon Dioxide, Aluminum, Silicon Nitride, and Tungsten. Figure 5 shows a Surface Micromachining process.
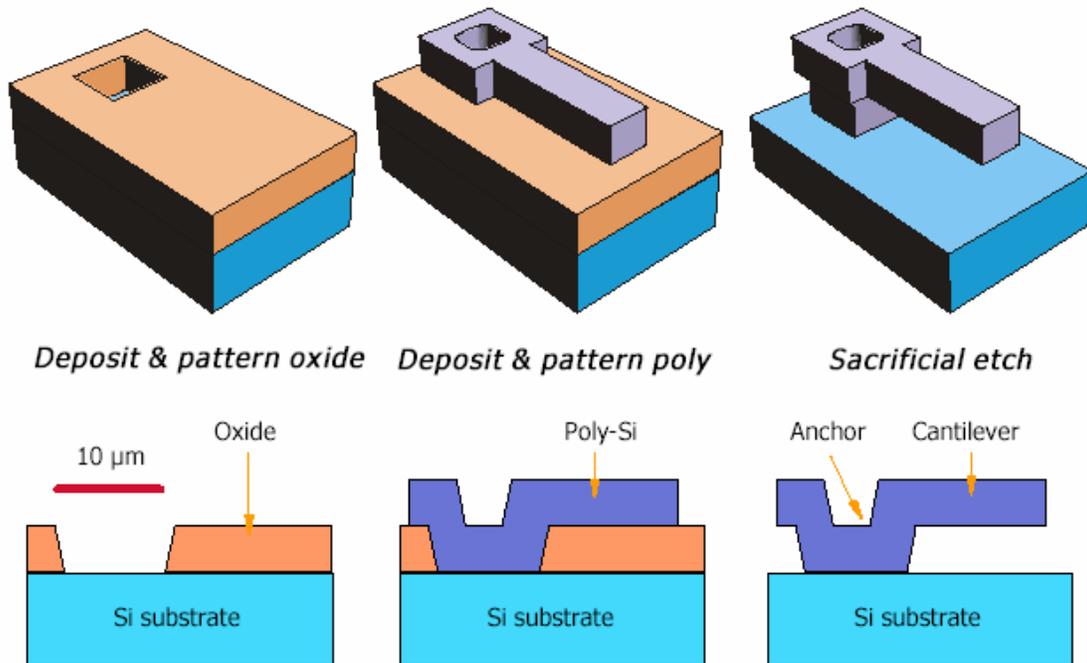
Figure 5: Surface Micromachining Process

2.2.5   LIGA

The acronym LIGA comes from the German name for the process (Lithographie, Galvanoformung, Abformung). LIGA uses lithography, electroplating, and molding processes to produce microstructures. It is capable of creating very finely defined microstructures of up to 1000µm high. In the process as originally developed, a special kind of photolithography using X-rays (X-ray lithography) is used to produce patterns in very thick layers of photoresist. Figure 6 shows the LIGA process.

Figure 6: LIGA Process

The X-rays from a synchrotron source are shone through a special mask onto a thick photoresist layer (sensitive to X-rays), which covers a conductive substrate. This resist is then developed. The pattern formed is then electroplated with metal. The metal structures produced can be the final product, however it is common to produce a metal mold. This mould can then be filled with a suitable material, such as a plastic, to produce the finished product in that material.

The above techniques use some form of masking, photo exposure and etching process, which consumes time, labor and cost. Moreover some of these processes release hazardous chemicals difficult to handle and dispose. Loss of precious metals and high lead times limit use of these techniques for mass fabrication.

2.3 INKJET TECHNOLOGIES AND MICROFABRICATION

Ink-jet is a non-impact dot-matrix printing technology in which droplets of ink are ejected from a small aperture directly to a specified position on the substrate to create an image. Inkjet printing has been used in many different designs and has a wide range of potential. Primarily, inkjet printing is divided into the continuous (CIJ), drop-on-demand piezoelectric (DOD) and thermal (TIJ) ink-jet methods [16].

Researchers at MIT have manufactured MEMS components using DOD inkjets in the two dimensional domain, namely linear and rotary electrostatic-drive motors [17]. Similar Drop-On-Demand (DOD) ink-jet method for printing of horizontal circuit interconnects has been demonstrated by using nano-particle fluid suspension (NPFS) by Szczech et al [18]. Both groups propose building 3D MEMS devices, but attempts have been restricted to the 2D domain due to lack of 3D deposition technology.

Researchers at Xerox Palo Alto Research Center use Acoustic Ink Printing (AIP), to produce photographic quality prints at speeds that compare favorably against the state of the art [10]. In AIP an ultrasonic beam is focused on the free surface of the ink to eject discreet droplets of controlled diameter. The advantage being that the printing process is "nozzleless", which enables generation of extremely small drops without sensitivity to defects in nozzle geometry. Though AIP assists in micro drop formation, it is restricted to printing of aqueous and wax-based inks.

The team at UCLA use thermally driven microinjector to eliminate satellite droplets [19]. Through a special heater and chamber design, bubbles are generated to surround the nozzle in such as way that they cut off the droplet tail and eliminate satellite droplets. Extending their

microinjector design to eject solvents and fluids, they have achieved droplet volumes smaller than 1 picoliter, 10 times smaller than present day commercial inkjet printers [20].

A field-effect transistor (FET) fabricated from polymer materials using printing techniques shows high current output and insensitivity to mechanical treatments such as bending or twisting [21]. The MIT Media Lab reports use of cadmium selenide nanocyrstals to print inorganic thin-film transistors with field effect mobilities up to 1 square centimeter per volt second [22].

Carr et al recognized the role of substrate properties on printing quality [23]. His team at Georgia Institute of Technology has studied the interaction of single droplet with textile media to yield a better understanding of the fundamentals affecting print quality.

MicroFab Technologies, Inc. has developed a print head that accurately dispenses solder to polymeric formulations at operating temperatures up to 300°C [24]. They have extended their design to print intrinsically conductive polymer, thermosetting resin loaded with conductive particles and ferrite-powders [25].

2.4   PIEZOELECTRIC DISC MODULATIONS IN CIJ SYSTEMS

Li and Chen [26] have presented a closed form analytical equation based on linear strain assumptions to analyze the passive plate deflection in a piezoelectric microactuator. Reiss and Smith [27] have modeled the ultrasonic characteristics and low frequency actuator characteristics of a deformable array transducer using both 2D and 3D finite element analysis. Morris and Forster [28] have used a finite element method to optimize the deflection of a circular bimorph consisting of a single piezoelectric actuator, bonding material and elastic plate of finite

dimensions. Li et al [29] present a concise analytical solution for the displacement distribution of a piezoelectric heterogeneous bimorph. They formulated key influence factors, such as the geometry, material properties, and mechanical parameters into a single expression for the beam's displacement.

Zhou [30] at Spectra Inc. has conducted a coupled field analysis of an ink jet print head with shear mode piezo transducer. However this analysis is focused on the drop on demand printing concept, which has a relatively simpler drop formation mechanism as compared to the CIJ system. Further the commercial application of piezoelectric-based microactuator in hard disk drives is simulated using the finite element method (FEM) by Jun and Zhaowei [31]. A theoretical dynamic and electrostatic analysis is performed to investigate the resonant frequency and displacement sensitivity.

Analytical solutions of piezoelectric device performance generally examine simple shapes (e.g. discs) under static or at resonant conditions. Analytical solutions of complex geometries (as in geometries of actual devices) often involve assumptions, which simplify the stress state and electric field distribution within the device. Invariably, this leads to inaccurate predictions of the observed response.

2.5   FLUID DYNAMICS MODELING AND EXPERIMENTATION

Lord Rayleigh (1878 [32]) described the mechanism by which a liquid stream breaks up into droplets. In 1951, Elmqvist of Siemens patented the first practical Rayleigh break-up ink-jet device [33]. This invention led to the introduction of the Mingograph, one of the first commercial inkjet chart recorders for analog voltage signals.

Richards et al provide a theoretical model for steady state laminar flow of two immiscible liquids with closer density and viscosity values (liquid-liquid) interaction [34]. The model deviates slightly from experimental results when highly varying density and viscosity fluids (liquid-gas) interactions are taken into consideration.

CFD simulations of inkjet printer at Lexmark International Inc. have saved up to one person-year in development time [35]. Yeh has simulated DOD inkjet printing process using (Volume of Fluid) VOF concept [36]. VOF is a program developed by the Los Alamos National Laboratory for the solution of two-dimensional transient fluid flow with free boundaries [37]. In this technique, a function $F(x,y,t)$ is defined whose value is unity at any point occupied by fluid and zero elsewhere. The fluid equations solved are the finite difference approximations of the Navier-Stokes equations.

Experimental setup to study aero-dynamical motion of CIJ charged droplets revealed that coalescence could easily occur in droplet train proceeding in air and it makes disorder of successive droplet train [38]. Keur and Stone describe the mechanism of drop formation, drop charging, drop deflection, aerodynamic interactions between drops, and limiting factors for a CIJ [39]. Wnek and Johnson from American Ink Jet Corp. have used nonlinear programming to optimize the physical properties of an ink-jet ink [40]. Kalaaji et al [41] perform non-sinusoidal piezoelectric excitation experiments for various values of voltages and phase angle under stable and unstable conditions.

2.6 RECOMMENDATIONS FOR A MODIFIED CIJ SYSTEM

The shortcomings in conventional lithography based techniques and DOD inkjet method can be overcome by leveraging the CIJ printing method. Continuous ink jet (CIJ) technology has emerged as an industrial workhorse in a wide variety of applications from production serial number printing, to sophisticated "drop-on-demand" printing applications [42].

The ability to deflect a train of charged droplets to desired target regions on the substrate is the key advantage of the CIJ technology over other competing inkjet methods. Thus conductive materials can be deposited at the will of a device designer. Moreover as opposed to single drop-on-demand technique the CIJ train of droplets makes it a rapid deposition technology. The entire train of droplets can be deposited for faster output or a portion of the train could be salvaged back into the system for selective deposition.

This research focuses on developing the CIJ technology to build 3 dimensional miniaturized devices in free space. The critical aspect to be investigated is the Piezoelectric disc behavior when in contact with the fluid. The displacement outputs from the Fluid-Structural Interaction (FSI) analysis are further utilized for the fluid model. Finally, the CFD model developed will assist in explaining relevant input parameters for optimal printing.

3.0   METHODOLOGY

The use of CIJ based technology for accomplishing high-speed 3D printing using nano particulate fluidic suspensions has been stressed earlier. The approach is to modify the commercial CIJ head to accommodate conductive suspensions for printing. Description of the CIJ technology as a background for model development in the upcoming chapters is presented in here.

3.1   CIJ TECHNOLOGY

In the early 1960s, Dr. Sweet of the Stanford University demonstrated that, by applying a pressure wave pattern to an orifice, the ink stream could be broken into droplets of uniform size and spacing [43]. When the drop break-off mechanism was controlled, an electric charge could be impressed on the drops selectively and reliably as they formed out of the continuous ink stream. The charged drops when passing through the electric field were deflected to form an image on the substrate and the uncharged ones were captured by the gutter and recirculated in the system. This printing process is known as the Continuous Inkjet (CIJ) printing [44].

The CIJ control system consists of an ink tank, which holds the ink to be printed. The tank is connected to a pump which, pumps ink through a filter to clear the ink from any debris. A valve manifold controls the flow to the print head. The pressure transducer monitors the ink pressure in the system and signals addition of solvent to the ink.

Higher pressure in the system is an indication of higher viscosity of ink, which may eventually clog the nozzle orifice. A venturi generates vacuum to suck the salvaged uncharged droplets from the gutter. The schematics of the control system and print head are shown in Figure 7 [45].
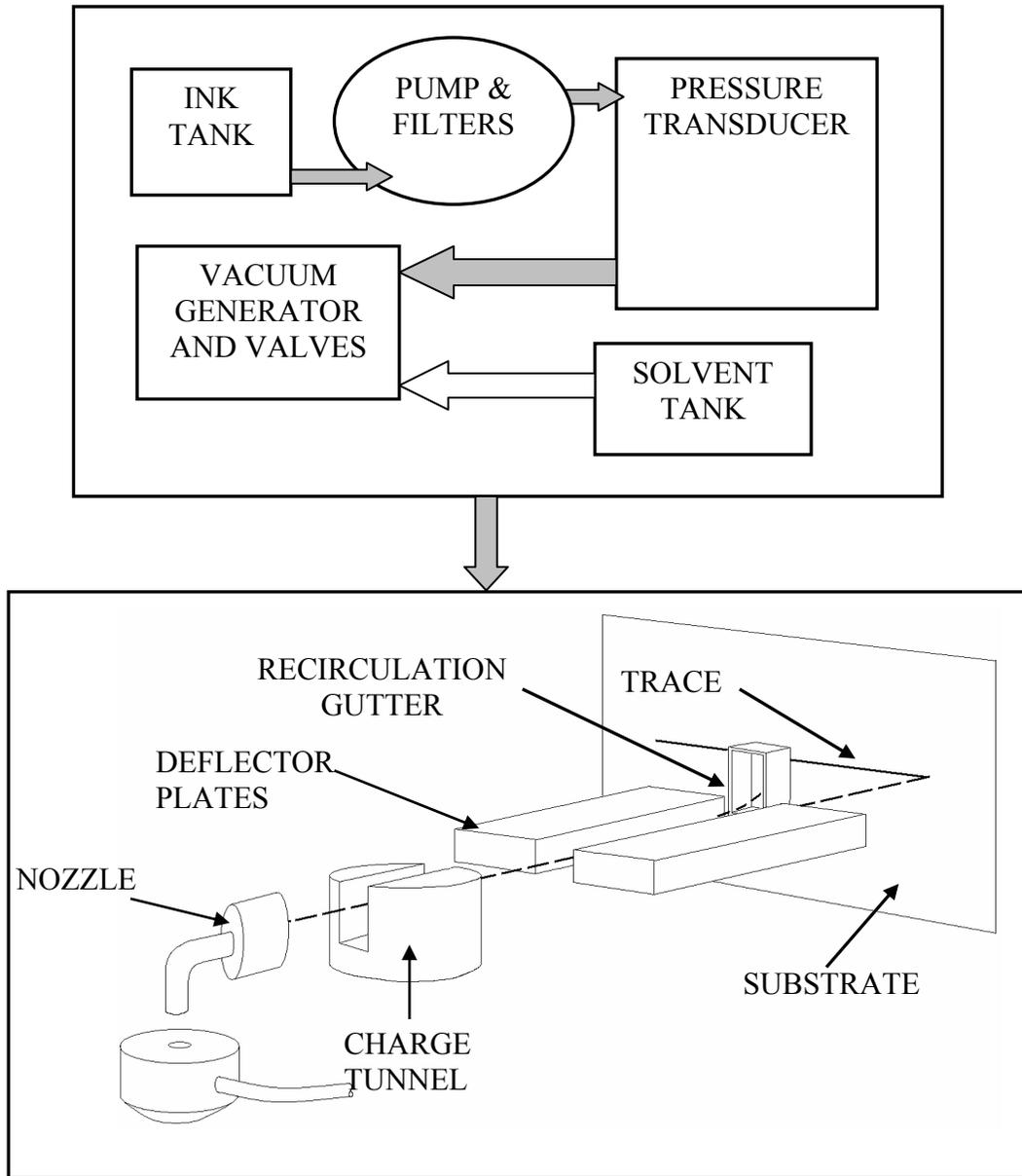
Figure 7: Control System and Print Head Schematics

3.2   OPERATION OF A CIJ HEAD

A conducting ink is supplied under pressure (5 to 50 psi) to an ink gun and forced out through a small nozzle of typically 35 to 110 microns in diameter [46]. As it passes through the nozzle, the liquid is piezoelectrically pulsed (modulated) and the stream breaks up into a continuous series of drops which are equally spread and are of the same size.

A voltage is applied between the charge tunnel (electrode) and the drop stream, when the drop breaks off from the stream. The drop carries a charge proportional to the applied voltage at the instant it breaks off. By varying the charge electrode voltages at the same rate as the drops are produced, it is therefore possible to charge every drop to a predetermined level. The drop stream continues its flight and passes between two deflector plates, which are maintained at a constant potential, typically plus and minus 3 kilovolt. In the presence of this field, a drop is deflected towards one of the plates by an amount proportional to the charge carried. Drops that are not being printed only receive a small charge. This causes them to enter a gutter to be recycled into the ink reservoir, instead of being deflected towards the substrate. Drops with sufficient charge are deflected on the substrate. Droplet formations are shown in Figure 8 [46].
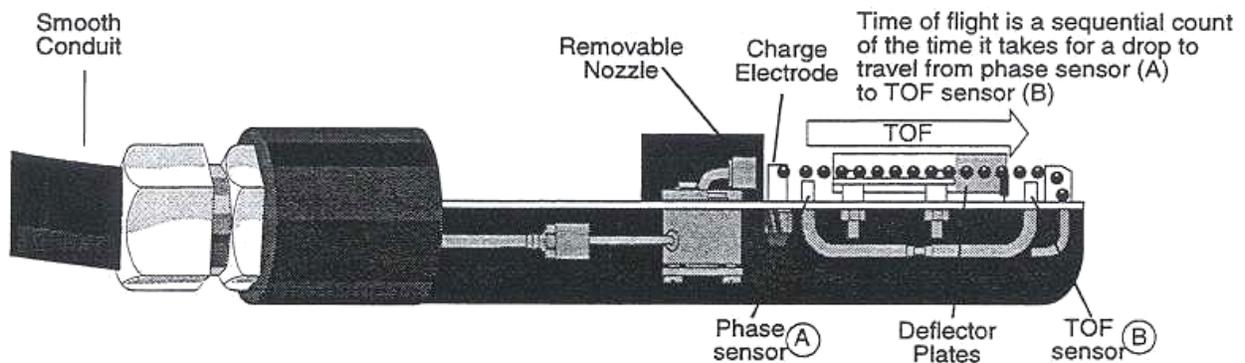
Figure 8: Side view of CIJ print head with drop formations

By varying the charge on the individual drops, different patterns including alphanumeric characters may be printed. A series of drops deflected across the substrate is known as a raster.

3.3   JET BREAKUP AND RAYLEIGH INSTABILITY

A stream of liquid will naturally break up into approximately equal sized droplets due to the influence of aerodynamic drag and noise. The drop break up however, can be accurately controlled by applying a disturbance in the fluid. This is achieved by oscillating a Piezo crystal in contact with the fluid, oscillating at a frequency that determines the frequency of drop break up. The method used is shown in Figure 9 [46].
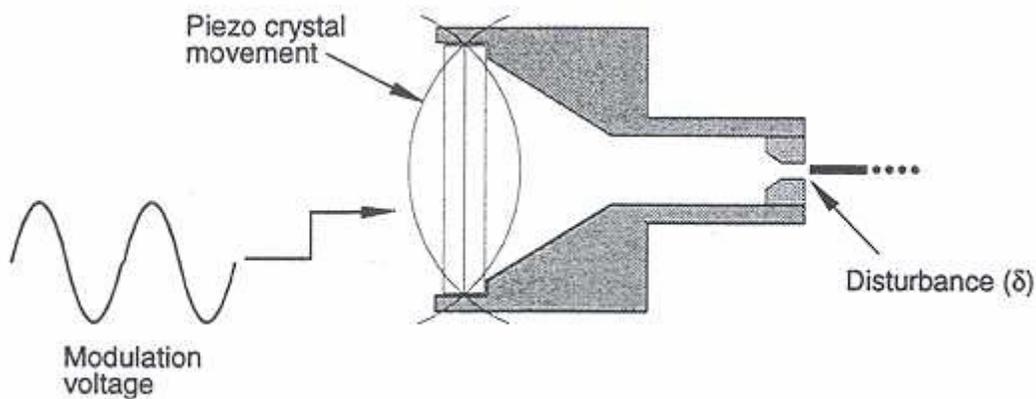
Figure 9: Piezoelectric crystal perturbation on the ink

If a voltage is applied to a Piezo crystal it will flex and the degree of flex will depend upon the voltage applied. The actual voltage applied is known as the modulation voltage. By applying a continuous sign wave (which swings from between positive and negative alternately) at the optimum frequency, the result is a stimulated jet, and drops are produced. The actual

movement is very small, i.e. the drops are formed by growth of the disturbance and not the actual volume displaced. Around a century ago, Rayleigh [39] analyzed the breakup of a cylinder of fluid into drops when a disturbance is introduced. His analysis indicated that a cylinder of fluid forms into a uniform sequence of droplets if the disturbance frequency is such that

$\lambda/d > \pi$ and $\lambda = v/f$

where,

d is the diameter of the orifice;

λ is the spacing of the droplets;

v is the velocity of the stream;

f is the disturbing frequency;

Rayleigh also determined that the time constant t, that is the time for a disturbance's amplitude to grow by a factor of e, is given in Equation 3.1 [32].

$$t = \left[\left(\frac{\rho d^3}{8T} \right) \times \left(\frac{1}{I} \right) \right]$$ (3.1)

where,

ρ is the fluid density;

T is the surface tension;

I is the Rayleigh instability factor

The Rayleigh instability factor is zero at $\lambda/d = \pi$ and becomes a maximum for λ/d of 4.5. The greatest instability therefore, occurs when this ratio lies near 4.5. As an indication of the instability, or the ease of forming droplets, disturbances are introduced at constant amplitude,

and the time required for the stream to breakup into droplets is measured. The level of modulation is an important factor on the actual formation of drops. The modulation required can vary depending upon the characteristics of the ink. For example, different modulations will be required for different viscosities of inks. The modulation level can also affect the position at which the drop breakup occurs, and the actual characteristics of the drops in terms of size and shape. Incorrect modulation can create satellite drops as shown in Figure 10 [46].
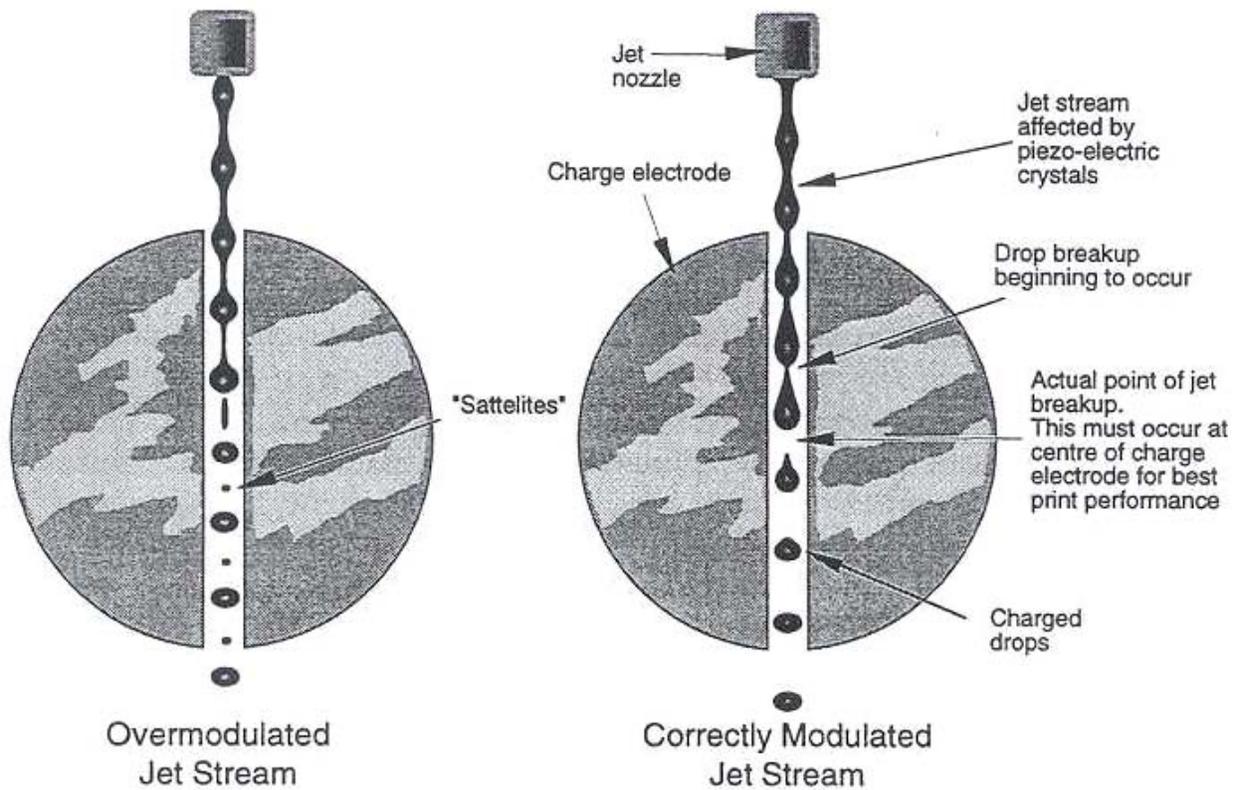
Figure 10: Modulation modes and satellite formations

3.4   MODELING AND VALIDATION APPROACH

The Continuous Inkjet (CIJ) system involves the complex interaction of three domains namely electrostatic, structural and fluid for the formation of drops. The PZT disc is excited by an input voltage to undergo high frequency oscillations that are applied to the fluid medium at its interface. The perturbations applied to the fluid grow exponentially with time and are propagated to the jet surface through the nozzle orifice. A combination of forced acoustic waves and Rayleigh instabilities leads to a controlled drop breakup. The above phenomenon is divided into three analyses based on input energies, physical domains and interfacial interactions as shown in Figure11.
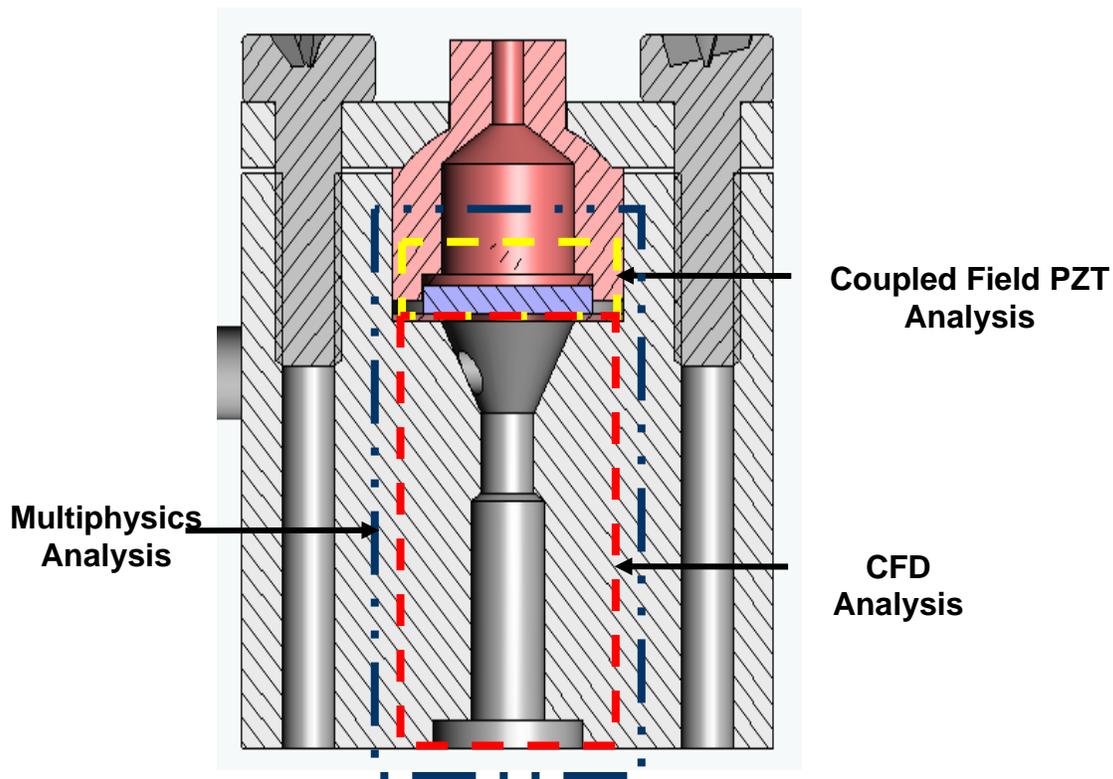
Figure 11: CIJ components and respective analysis types
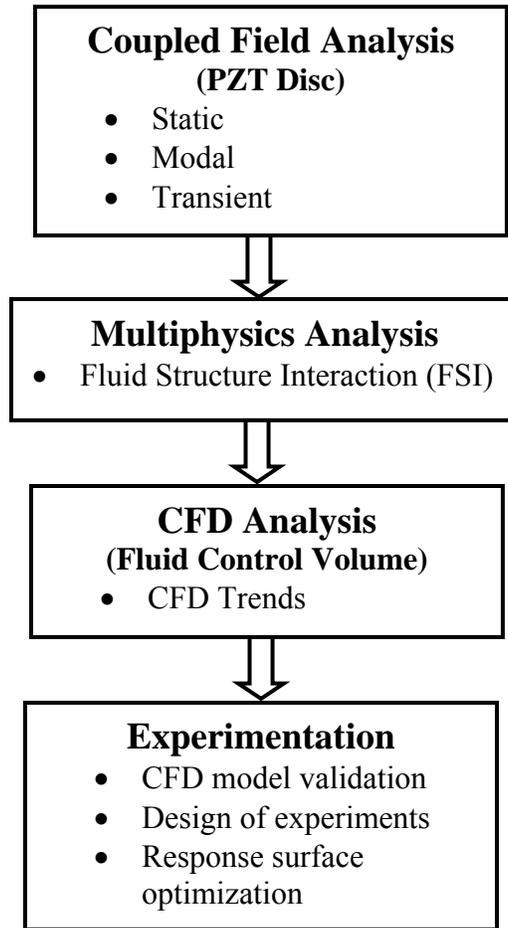
Figure 12: Research Methodology

Figure 12 shows the research methodology adopted in this dissertation. The first stage is the modeling of the piezoelectric disc, which generates the perturbation displacements. A coupled-field analysis is employed that simulates the PZT disc behavior in free air (low density fluid). The second stage is the modeling of the fluid-structural interaction (FSI) at the PZT disc-fluid interface using a Multiphysics analysis. This analysis will determine the behavior of the PZT disc when in contact with a denser fluid such as water, MEK or nano particulate suspension. The PZT displacement from this analysis is superimposed as Simple Harmonic displacement

(SHM) boundary condition in a Computational Fluid Dynamic (CFD) analysis. The SHM boundary condition mimics the PZT displacement behavior.

The CFD model developed in here is validated with real-time experimental results. Ultra high-speed photographic images are used to compare the droplet characteristics with the simulation results. Further, an experimental design approach is used to identify significant factors affecting the droplet volume and velocity. A Response Surface design is employed to optimize the droplet volume based on significant input parameters.

4.0   COUPLED-FIELD ANALYSIS OF CIJ PIEZOELECTRIC DISC

Piezoelectricity is the property exhibited by a special class of materials in which the electric and mechanical fields are directly coupled. Devices built from piezoelectric materials deform when an electric field is applied to their surfaces and generate voltage when they are deformed by the application of an external force. The smart structure characteristic of PZT makes it an ideal candidate for applications requiring restricted component dimensions, agile response and high multidisciplinary functionality. Typical applications include high frequency resonators, sensors in automotive safety systems (airbag deployment), actuators in micro pumps and other Micro Electro Mechanical (MEMS) devices.

The use of piezoelectric (PZT) bimorph structures for fluidic dispersion has widespread applications. Of particular interest to the present investigation is the utilization of a piezoelectric disc for the development of a three-dimensional printing technology that incorporates conductive nano particulate suspensions.

4.1   CIJ PRINT HEAD PZT MODULATION

A Continuous Inkjet (CIJ) print head contains a PZT modulator assembly, which is subject to a fluid under high pressures (5 to 50 psi). An exploded view of the components of a PZT modulator assembly within a typical CIJ print head is depicted in Figure 13. It consists of a

piezoelectric disc with electric leads on one side and pressurized fluid on the other side. Fluid is supplied through inlet tubes provided on the sides of the modulator assembly. The piezo carrier accommodates the terminal connector, piezoelectric disc and Teflon seal.

The PZT disc is vibrated at high frequency (20 to 100 kHz) with an alternating electric voltage to ultimately generate droplets that are discharged from the print head. The PZT disc deforms in conjunction with the sinusoidal waveform input signal, thereby creating pressure fluctuations within the chamber. These pressure fluctuations are complemented by Rayleigh Taylor instabilities resulting in a consistent drop breakup. An orifice with aperture opening (30 to 60 micrometers in diameter) is provided in the nozzle to eject micro droplets (60 to 120 micrometers in diameter).
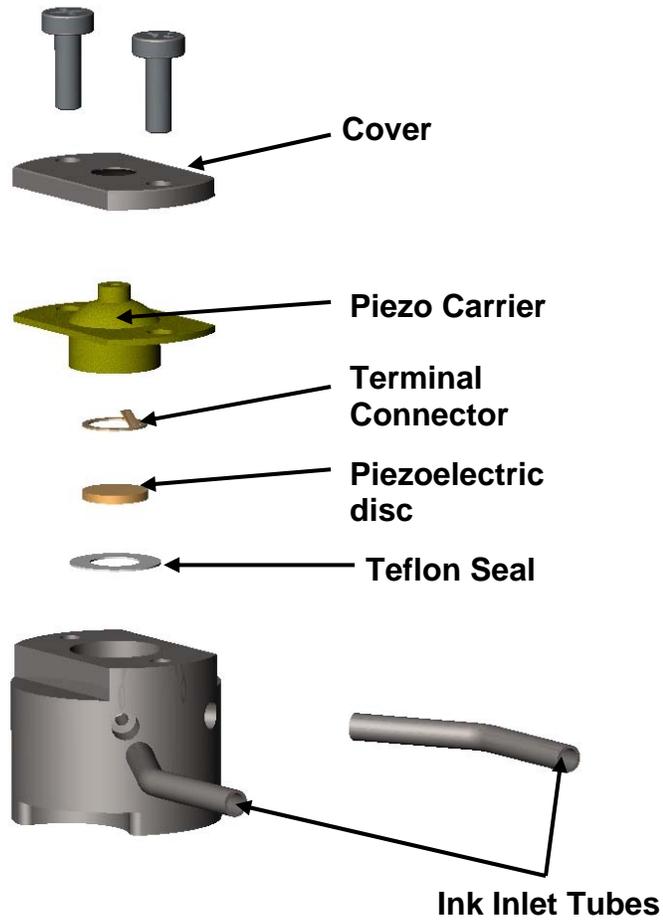
Figure 13: Exploded view of piezoelectric modulation assembly

4.2 CIJ PIEZOELETRIC DISC

The piezoelectric disc within the PZT modulator assembly is a critical component for controlling the droplets generated by the CIJ print head. In principle, a fluid stream is perturbed by acoustic or capillary waves generated by the vibrating PZT disc. The vibration characteristic of the PZT disc is a vital component for determining the droplet generation behavior. It is therefore essential to investigate the piezoelectric disc deformation during both static and transient loading. One of the problems encountered during transient CIJ operation is the generation of satellite droplets. Satellite drops are micro scale sized unwanted droplets that are

generated between regular sized CIJ drops. These satellite drops are responsible for an inferior quality print and in many cases, they hinder the generation of regular sized droplets. Figure 14 shows the cross-sectional view of a piezoelectric disc within the PZT modulator assembly.
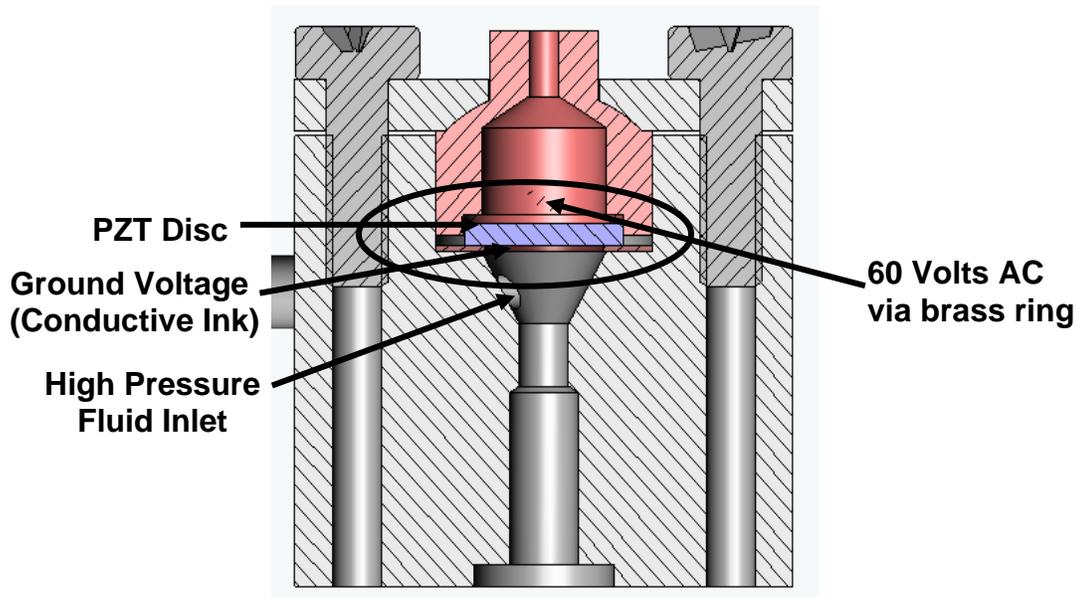
Figure 14: Cross-sectional view of piezoelectric disc within PZT

The investigation of the transient behavior of the PZT disc can provide important insight into the conditions that lead to the formation of satellite drops. In theory, by optimizing the design of PZT disc and its vibration characteristics, satellite droplets can be eliminated. The PZT disc is supplied with 60V AC input via a brass ring on the top and is grounded at the bottom by virtue of the conductive fluid. In this chapter we will analyze the PZT behavior using commercial FEA software ANSYS®.

4.3 VALIDATION OF NUMERICAL RESULTS WITH THEORETICAL SOLUTION

Before attempting to optimize the performance of a PZT disc within a CIJ printing system using a coupled-field element (PLANE223) of the commercial software ANSYS® 8.0 [47], it is essential to first validate the numerical technique using a theoretical formulation. The coupled-field element PLANE 223 as shown in Figure 15 is a quadratic eight node planar element with up to three degrees of freedom per node.
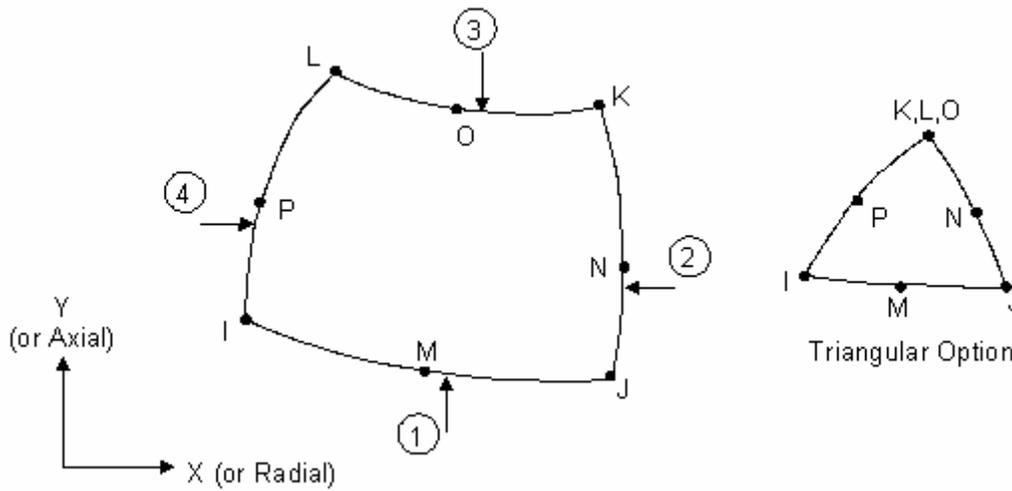
Figure 15: Geometry of PLANE 223 element

It has structural, electrical, piezoresistive, and piezoelectric capabilities. The electromechanical constitutive equations for linear material behavior are [48]:

$$\{T\} = [c^E]\{S\} - [e]\{E\} \tag{4.1}$$

$$\{D\} = [e]^t\{S\} + [\varepsilon^S]\{E\} \tag{4.2}$$

where,

{T} is the mechanical stress vector,

{S} is the mechanical strain vector,

{D} is the electric flux density vector,

{E} is the electric field vector,

$[c^E]$ is the stiffness matrix evaluated at constant electric field,

[e] is the piezoelectric matrix relating stress/electric field,

$[e]^t$ is the piezoelectric matrix relating stress/electric field (transposed),

$[\varepsilon^S]$ is the dielectric matrix evaluated at constant strain.

The bimorph layers within PLANE223 elements are bonded together with opposing polarities in the vertical direction. Thus, when electric field is applied to the bottom layer it expands along the length. The top layer has opposite polarity to the applied voltage and contracts along its length. The combined effect of these deformations results in the upward bending of the cantilever beam under a series voltage loading conditions. The mechanical and piezoelectric properties of the material are given in Table 1.

Table 1: Mechanical and piezoelectric properties for a bimorph cantilever beam

Property	Notation	Values
Young's modulus (Pa)	E_X	2.0e9
Shear modulus (Pa)	G_{XY}	0.775e9
Poisson's ratio	PU_{XY}	0.29
Piezoelectric strain coefficient (m/V)	d_{31}	2.2e-11
Permittivity at constant stress (F/m)	ε_{33}	1.062e-10

To ensure that the material and element parameters are being input correctly a simple PLANE223 model will be compared to a known theoretical solution. More specifically, the displacement value at the tip of a piezoelectric bimorph cantilever beam will be compared to a theoretical value given by the constituent equations of piezoelectric bimorphs. In this regard, the bimorph cantilever beam shown in Figure 16 was modeled and analyzed. In the model; the beam had a length L of 10e-3 m and a layer thickness h of 0.5e-3m. In the model one end of the beam

was fixed and the other end had a pressure load applied with a magnitude of 34475Pa (5psi), which is represented by upward arrows on its bottom layer. The bimorph cantilever beam was also subjected to a voltage of 60V DC on its bottom layer and grounded on the top layer. Elements with an aspect ratio of unity were used to obtain consistent results. It is important to note that the loading and boundary conditions in the model are similar to the boundary conditions experienced by the PZT disc within the PZT modulator.
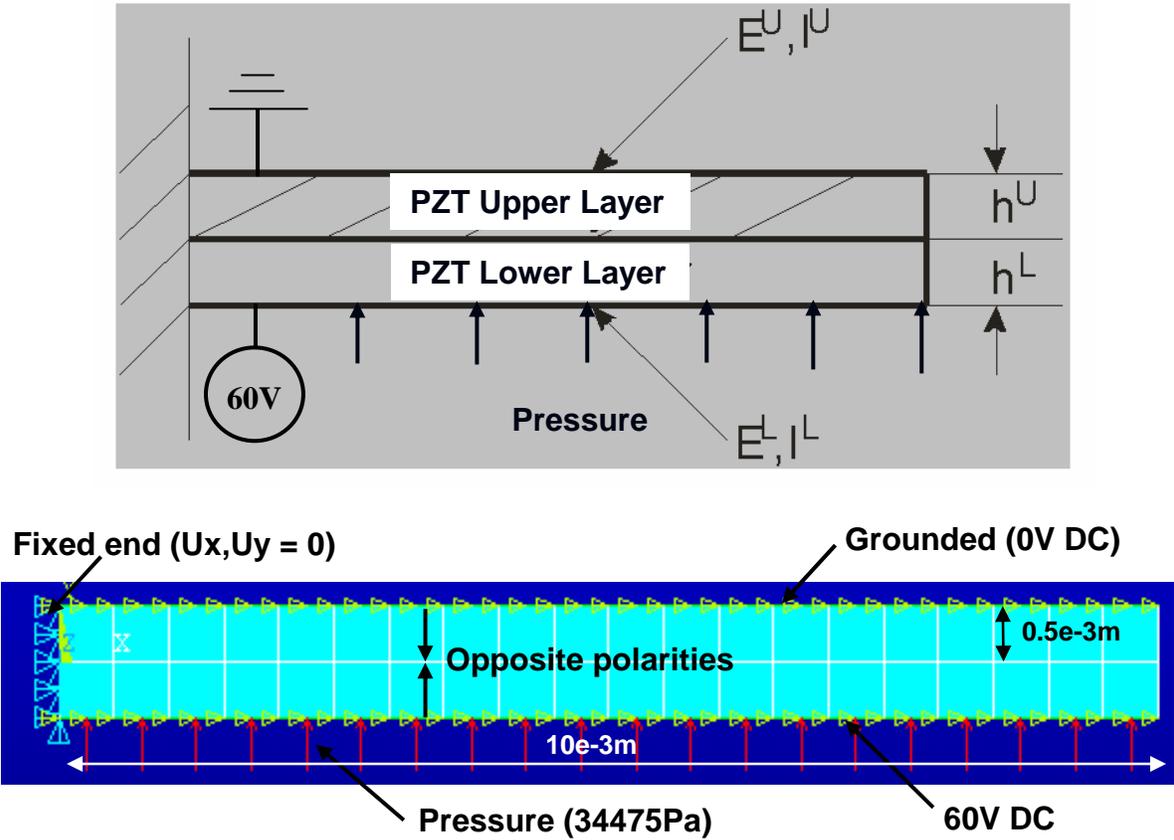
Figure 16: Schematics and boundary conditions of PZT bimorph cantilever beam

For the problem posed, a theoretical solution [49] is available, which provides the tip deflection of the cantilever beam as a function of the applied voltage, geometry and material properties. In the finite element model, the tip deflection of the bimorph cantilever beam for a

static coupled field analysis is δ = 2.6035e-4 m. The theoretical value computed by the equation 4.3 is δ = 2.5889e-4 m. Both values show a close conformance to each other with an error of 0.56%.

$$[\delta] = \left[\left(\frac{3s_{11}^E L^4}{16h^3} \right) \times p + \left(\frac{3d_{31}L^2}{8h^2} \right) \times V \right] \tag{4.3}$$

where,

$\{\delta\}$ is the tip deflection of the bimorph cantilever beam in m,

$\{s_{11}^E\}$ is the compliance coefficient = $\{1/E_x\}$ in m^2/N,

$\{d_{31}\}$ is the piezoelectric strain coefficient in m/V,

$\{L\}$ is the length of the cantilever beam in m,

$\{h\}$ is the thickness of individual bimorph section in m,

$\{p\}$ is the pressure applied on the bottom of the cantilever beam in Pa,

$\{V\}$ is the voltage applied to the top layer of the beam in V,

4.4   PIEZOLECTRIC DISC FINITE ELEMENT MODEL (STATIC ANALYSIS)

Once the feasibility study was completed, a PZT disc was modeled using PLANE 223 coupled field elements. In the model, axisymmetry was utilized to aid in the computational efficiency without compromising on the accuracy of the solution. The dielectric constants (ε^s), piezoelectric strain coefficients (d) and compliance matrix (s^e) for the bimorph material Lead Zirconate Titanate (PZT-5A) [50] are given in Figure 17. The bimorph disc used in the present investigation was custom ordered to be fitted inside the PZT modulator assembly [51]. In the literature [26], analytical approaches are presented for PZT discs with simply supported

boundary conditions for static analysis. However the modal and transient behavior of an arbitrarily constrained PZT bimorph disc is complicated and therefore lends itself to the finite element method.

$$[s^E] = \begin{bmatrix} 16.4 & -5.74 & -7.22 & 0 & 0 & 0 \\ -5.74 & 16.4 & -7.22 & 0 & 0 & 0 \\ -7.22 & -7.22 & 18.8 & 0 & 0 & 0 \\ 0 & 0 & 0 & 47.5 & 0 & 0 \\ 0 & 0 & 0 & 0 & 47.5 & 0 \\ 0 & 0 & 0 & 0 & 0 & 44.3 \end{bmatrix} \times 10^{-12} m^2/N \qquad [\varepsilon^S] = \begin{bmatrix} 1.53 & 0 & 0 \\ 0 & 1.53 & 0 \\ 0 & 0 & 1.505 \end{bmatrix} \times 10^{-8} F/m$$

$$[d] = \begin{bmatrix} 0 & 0 & -171 \\ 0 & 0 & -171 \\ 0 & 0 & 374 \\ 0 & 0 & 0 \\ 0 & 584 & 0 \\ 584 & 0 & 0 \end{bmatrix} \times 10^{-12} C/N$$

Figure 17: Mechanical and piezoelectric properties for bimorph PZT disc

The piezoelectric disc modeled in the present analysis is shown in Figure 18. As illustrated, the PZT has a radius r of 2.55e-3m and bimorph layer thickness h of 0.32e-3m. In the model, the piezoelectric bimorph disc is clamped on its top and bottom periphery surfaces, thereby constraining the displacement in the Ux and Uy directions. The left edge is constrained in the Ux direction to impose the axisymmetric boundary conditions. A 60V DC voltage is applied on the top surface where the annular electric leads rest on the disc. The bottom surface is grounded by virtue of contact with conductive fluid.

**Constrained top
and bottom (Ux,Uy = 0)**

60 V DC

Ground Voltage (Conductive Ink)
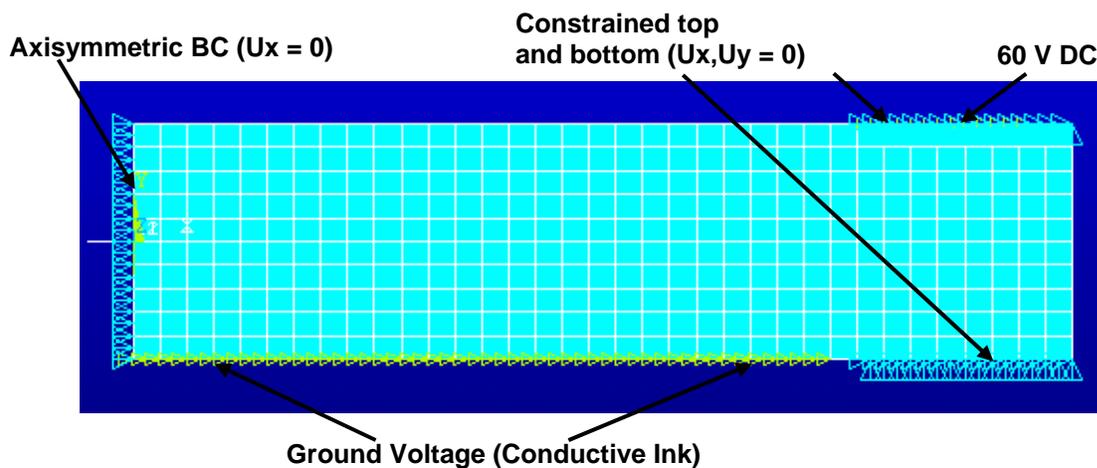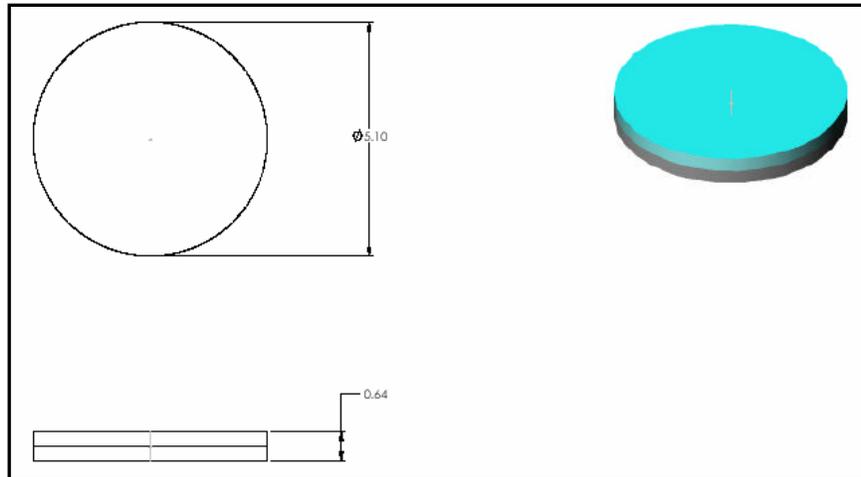
Figure 18: PZT bimorph disc and finite element boundary conditions

In the numerical simulation, an aspect ratio of one was used for the elements in the finite element mesh to determine the number of elements required to attain accurate results. A grid independence study was conducted to obtain the optimal number of elements along the PZT disc radius. Figure 19 depicts a graph of the maximum displacement of the PZT disc at the center versus the number of elements along the PZT disc radius. It was observed that for less number of elements such as 10 the displacement value was inflated to 8.5e-9m. Also increasing the number

of elements beyond 40 added no significant benefits to the accuracy of the solution. Thus, the minimal number of elements to obtain accurate results was found to be 40.
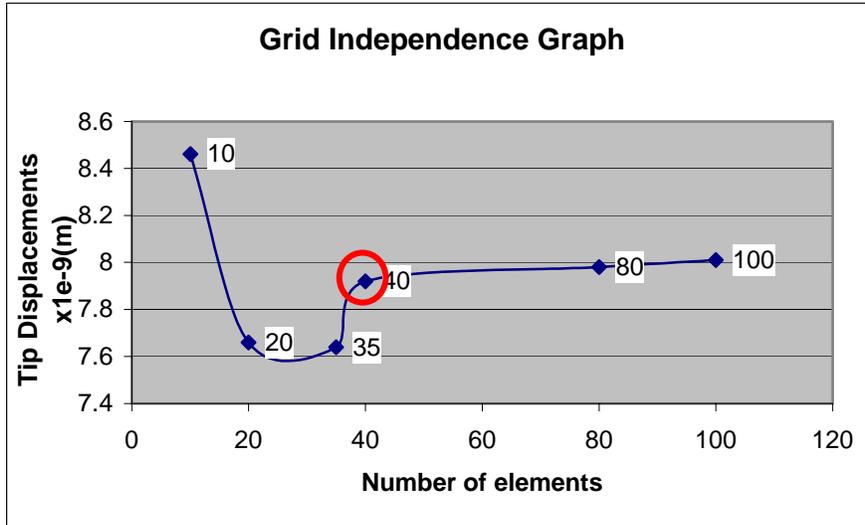
Figure 19: Displacement at disc center v/s number of elements along the PZT disc radius
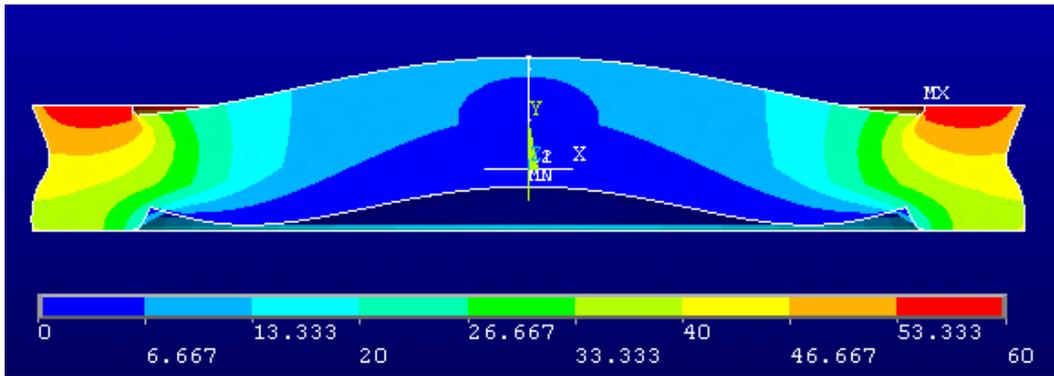
Figure 20: Voltage drop across the PZT disc in volts (cross sectional view)

Figures 20 show the distribution of voltage across the cross-sectional area of the PZT disc. The figure shows a voltage of 60V on the top annular region, which represents the electric leads, while the bottom layer is grounded as it is in contact with conductive fluid.
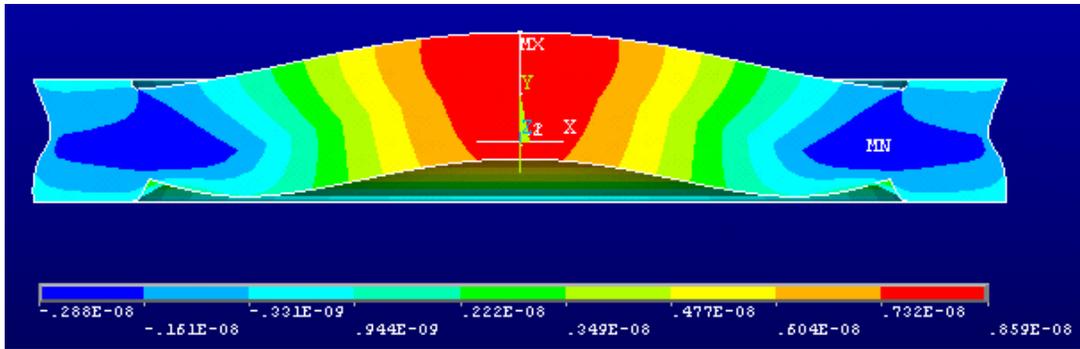
Figure 21: Displacement values of the PZT disc in meters (cross sectional view)

Figures 21 show the distribution of displacement across the cross-sectional area of the PZT disc. For the boundary and loading conditions applied to the model, the PZT disc deformation has been exaggerated to illustrate the deformation behavior of the disc. As expected from the applied boundary conditions, the maximum deflection of the PZT disc occurs at the center and has a magnitude of 7.925e-9 m. It is important to note, however, that the deformed shape shown in Figure 21 cannot be used to predict the behavior of the actual PZT disc because it does not take into account the dynamic effects during sinusoidal excitation.

4.5   MODAL ANALYSIS OF PZT DISC

Before attempting to model the transient behavior of the PZT disc it is essential to first determine its natural frequencies. This is due to the fact that the generation of uniform sized drops in a CIJ printing system is based on perturbing the fluid at appropriate frequencies. Exciting the fluid beyond a threshold frequency value will lead to the phenomenon of satellite droplet formations. To establish the threshold frequency values for the finite element model a modal analysis was performed on the PZT disc. In the modal analysis, the Block Lanczos

eigenvalue solver was utilized to extract the eigenfrequencies for the PZT disc [52]. The first five

natural frequencies for the PZT disc under the above-mentioned boundary conditions are listed in

Table 2. Since the first natural frequency of the disc was found to be 186246 Hz, the disc should

not be excited above 93kHz (half of its first frequency), to limit secondary harmonics and

eliminate satellite droplets.

Table 2: Natural frequencies for PZT disc

Set	Frequency
1	186246
2	539790
3	916491
4	956071
5	1391430

4.6   TRANSIENT COUPLED FIELD ANALYSIS OF PZT DISC

The dynamic deformation behavior of the PZT disc was captured with a transient

coupled-field finite analysis. Similar to the static case the bimorph PZT disc was modeled

axisymmetrically and was given identical boundary conditions and material properties to that

described previously. The disc cross-section in the X-Y plane can be rotated 360° about its

central axis to obtain a 3D view. It must be noted that the transient analysis performed in this

section captures the PZT disc behavior in free air. The disc is excited by a 60V AC input signal

at 80kHz, which is less than one-half its natural frequency (186246 Hz). A time step of 0.625μs

was used to precisely capture the sinusoidal displacement waveform. Figure 22 shows the

displacement shape of the PZT disc at a time *(t)* of = 18.75μs. The periphery of the PZT disc has

negligible displacement in Uy direction (as shown in red), while the disc center (shown in blue) has maximum displacement.
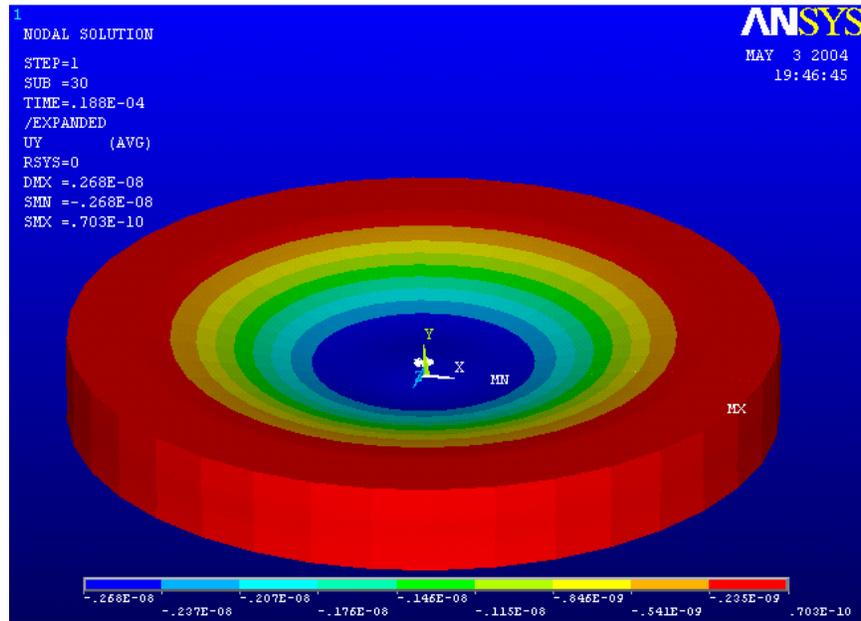
Figure 22: Displacement values of the 3D PZT disc at 18.75 μs in (m)

In order to analyze the transient behavior of the disc, Figure 23 was generated to superimpose the input voltage (red) and output displacement (yellow) at the center of the disc. As demonstrated in the figure, the input voltage has a sinusoidal waveform with a time period of 12.5μs. The output displacement waveform at the PZT disc center, however, deviates from a predominant sinusoidal shape. Such a finding can be attributed to differences in the time lag between the two waveforms, which results in opposing voltage and displacement cycles of the PZT. For the present configuration (60V AC, 80kHz) the time lag between the electrical excitation and the physical displacement are on the order of 1μs. The voltage cycle reverses ahead of the displacement cycle in time, thereby forcing the disc to momentarily change its

direction. The PZT disc will continue to displace in its original direction due to residual strain energy after the momentary pause or change in direction. The abrupt change direction leads to an increase in the time lag between electrical excitation and PZT displacement. In the subsequent cycles when the electrical voltage reverses its direction, the PZT displacement has a greater time lag than earlier cycles. These momentary reversals in displacement directions accumulate over time, thereby causing future displacement reversals to occur non-uniformly over time.
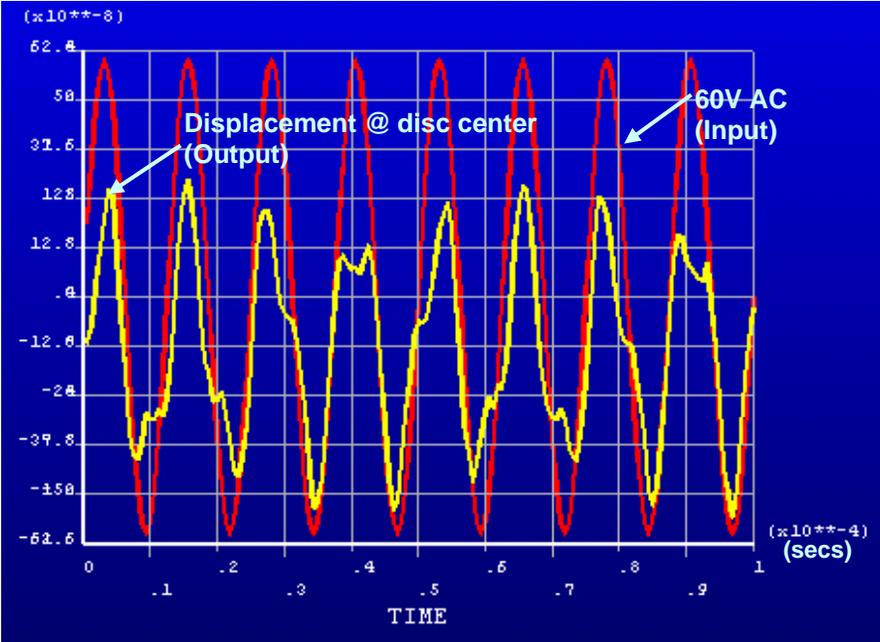
Figure 23: Superposition of input voltage and output displacement waveforms for 100μs

The average amplitude value of the PZT disc for transient analysis is δ = 2.6-8m, which is substantially higher than that found in the static analysis δ = 7.925e-9m. This increase in amplitude can be attributed to the kinetic energy imparted to disc by the input signal. As highlighted in Figure 23, the dynamic effect of the PZT disc substantially alters the deformation behavior. It is noteworthy to mention that the disruptions in the displacement waveform are observed when the PZT disc is in contact with a lower density fluid (air). For this reason it is

important to simulate the transient behavior of PZT disc in the presence of a higher density fluid such as water to understand its true dynamic characteristics.

4.7   TRANSIENT ANALYSIS OF PZT DISC WITH FSI

The primary aim of simulating the PZT disc is to replicate its transient behavior within an actual CIJ print head. Predicting the disc displacement pattern in free air gives an overview of the transient behavior but does not include the dampening effects introduced by a higher density fluid. In addition, displacement in free air does not provide information on the interplay of the physical properties of the fluid such as viscosity and surface tension with the deformation of the PZT disc. For this reason, a transient analysis of the PZT disc was conducted to account for fluid-structural interaction (FSI). In the present analysis the bottom layer of the PZT disc was placed in contact with an organic solvent Methyl Ethyl Ketone (MEK). The physical properties of the fluid are given in Table 3.

Table 3: Physical properties of MEK

Property	Notation	Value
Density (kg/m^3)	ρ	0.85e3
Dynamic Viscosity [kg/(m.s)]	μ	3.5e-3
Surface Tension (kg/m^2)	σ	2.5e-3

In the analysis fluid was supplied at 40 psi (275800 Pa) within the PZT modulator assembly. The effect of gravity was taken into consideration while modeling the FSI. The structural and fluidic domains were both modeled axisymmetrically. The mechanical and piezoelectric properties of the PZT disc were similar to those used in the static analysis and the

45

boundary conditions were identical with the exception of input voltage. In the FSI model, an input voltage of 60V AC was applied at 80kHz. A time step of 0.625μs is used to capture the fluid structural interaction and each input voltage waveform had a time period of 12.5μs.

In the finite element model, the transient behavior of the PZT disc was captured for the initial 120μs, which was equivalent to approximately 10 displacement cycles. Figure 24 shows the superposition of the input voltage waveform (red) and the output displacement waveform (yellow). The input voltage fluctuates between +60V to –60V and the PZT disc displacement varies sinusoidal.
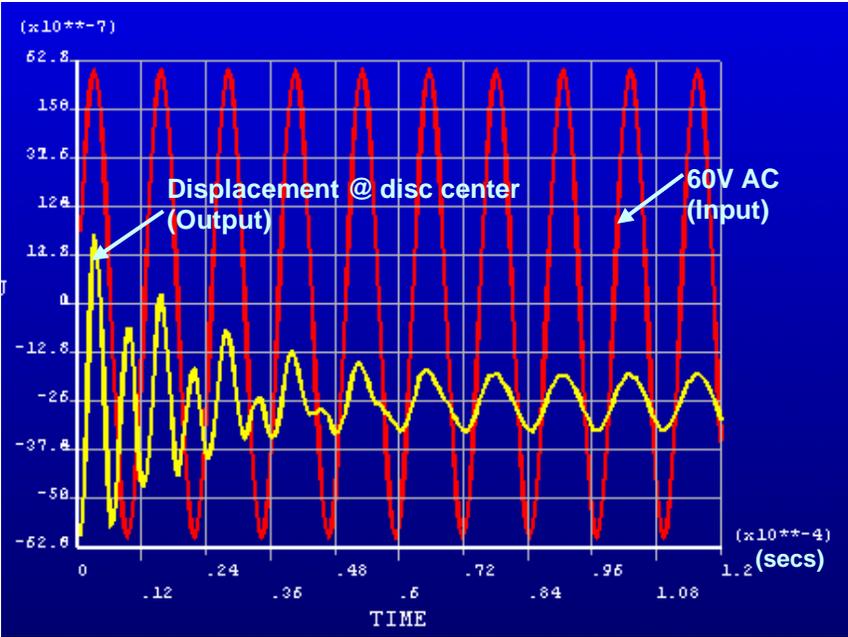
Figure 24: Superposition of input voltage and output displacement waveforms for 120μs (FSI)

During the initial displacement cycles, the PZT displacement shows increased amplitudes of fluctuations. This can be explained by the fact that the initial pressure surge inside the PZT

modulator assembly. After the initial 50μs, the displacement waveform stabilizes to a steady amplitude. Unlike the transient analysis in free air, the FSI analysis does not produce abrupt reversals of directions in the displacement waveform because of the dampening provided by the MEK fluid. This forces the displacement waveform to be in harmony with the input voltage waveform.
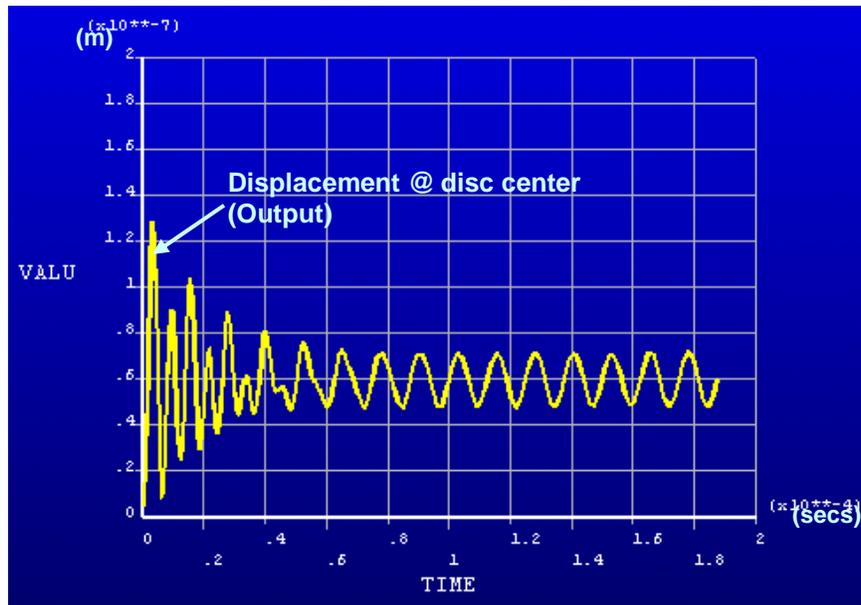
Figure 25: Displacement waveform of PZT disc for 187.5μs (FSI)

Figure 25 shows an extended view of the PZT disc displacement for 187.5μs in the transient FSI analysis. In the analysis, the displacement waveform attains a steady amplitude of δ = 1.15-e8m, which is less than the amplitude obtained in free air. This again is due to the increased dampening of the PZT disc in the higher density fluid (MEK). When the PZT disc vibrates in free air, its amplitude varies in both the positive and negative direction. However in the case of FSI transient analysis, the PZT disc is pre-stressed in the positive direction from the higher fluid pressure, which pushes the disc in the positive direction. As a result the disc vibrates sinosoidally in the positive direction.

5.0   MULTIPHYSICS ANALYSIS OF CIJ SYSTEM

Continuous inkjet printing is inherently more complex system than other inkjet techniques. This is because CIJ systems include precision coupling between the electrostatic, structural and fluid regimes to generate a synchronous droplet stream. Furthermore, the CIJ process operates at the extremes of both the temporal and spatial domains. The CIJ print head generates droplets in the MHz range (in microseconds) in drop diameters range between 10 to 150μm thus, making it an ultra-high speed microscopic process.

Traditionally, experimental procedures have been used to characterize the CIJ process [53]. These experiments have been used to obtain spatial information on droplet formation such as the drop volume and velocity. Despite their important value, CIJ experiments are not capable of unfolding the details of droplet transport mechanisms such as pressure fluctuations, which is a significant aspect in drop breakup. For this reason a novel way Multiphysics analysis will be employed in the present investigation to capture the interaction of the above-mentioned domains.

5.1   CIJ SCHEMATICS PERTINENT TO FSI

The Multiphysics analysis conducted in this dissertation focuses on the drop generation mechanisms in the CIJ process. Analysis of the charging and deflecting of droplets will be addressed in subsequent research. Figure 26 shows a cross-sectional view of the PZT modulator

assembly. In Figure 26, the region of interest has been highlighted and includes the piezoelectric bimorph disc and the fluid chamber. In the modulator assembly, fluid is supplied at high pressure (5 to 50 psi) through the inlet tube. The piezoelectric bimorph disc is vibrated at high frequencies to perturb fluid within the fluid chamber. These perturbations generate acoustic waves, which result in consistent drop breakup at frequencies equal to the excitation frequency.
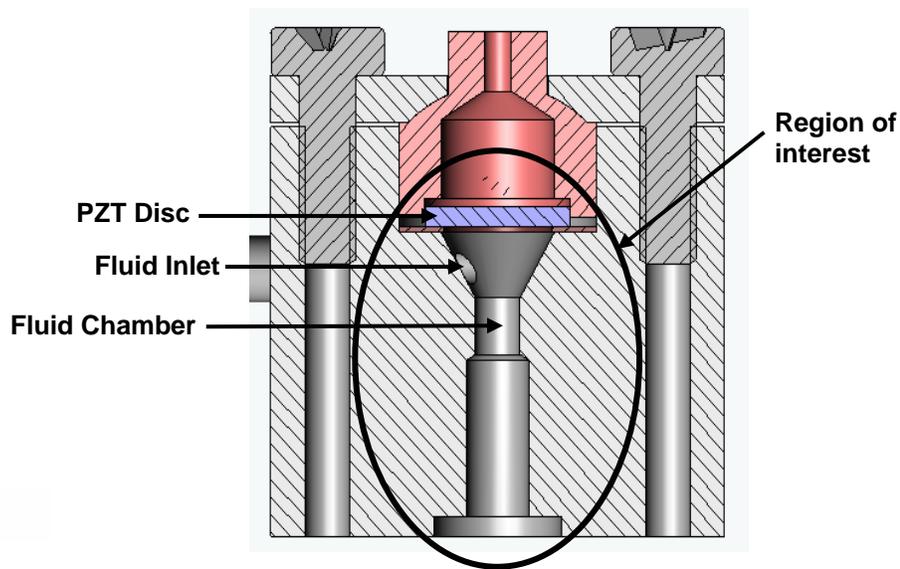
Figure 26: Cross-sectional view of PZT modulator assemble components

Figure 27 shows the cross sectional view of the components of interest modeled in the Multiphysics analysis. The PZT disc interfaces with the fluid medium such that the fluid domain is modeled from the PZT disc interface to the nozzle orifice. The high-pressure inlet tube is modeled as a boundary condition in the model. The droplet is allowed to exit from the control volume after a limited path of flight, which is represented with an open wall boundary condition. The width of the control volume during droplet path of flight is larger than the average droplet radius. Based on the input excitation characteristics, the droplet radius varies from 2 to 3 times

the orifice radius. This consideration is important because it impacts the total number of fluid elements within the CV.
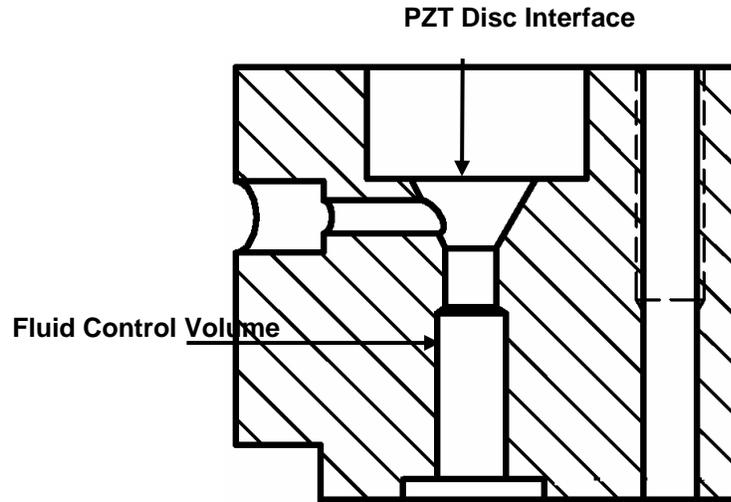
Figure 27: Cross-sectional view modeled of PZT modulator assembly components

5.2   FLUID-STRUCTURAL INTERACTION (FSI) ALGORITHM

The transfer of PZT disc displacements to fluid is handled with a fluid-structural interaction (FSI) algorithm. The FSI algorithm uses a sequential coupling technique, which solves the equations for the fluid and solid domains independently. The algorithm transfers structural displacements and fluid forces across the fluid-solid interface and continues to loop through the solid and fluid analyses until convergence is reached for a particular time step (or until the maximum number of stagger iterations is reached) [54]. Convergence in the stagger loop is based on the quantities being transferred at the fluid-solid interface. Figure 28 (adapted from reference [54]) shows the algorithm for the time and stagger loops of a fluid-solid interaction analysis. The fluid-solid interface must have two sets of solid model entities and

nodes; one set for the fluid region and one set for the solid region. It is customary to have a dissimilar mesh along the fluid-solid interface due to different mesh resolution requirements within the fluid and solid analysis.

Begin Time Loop

    Begin Stagger Loop

ANSYS – SOLID Analysis
Interpolation and Load Transfer

FLUID Mesh Update

ANSYS – FLUID Analysis
Interpolation and Load Transfer

Convergence Check

End Stagger Loop

End Time Loop
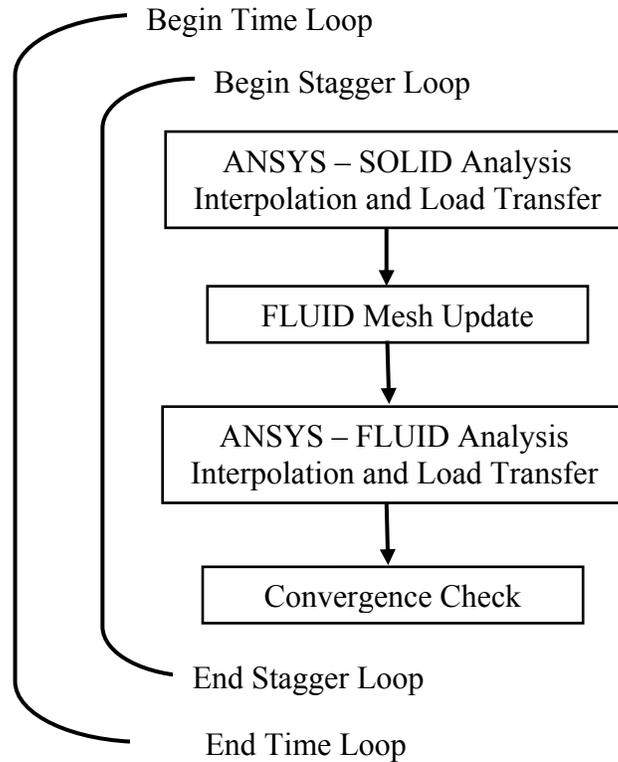
Figure 28: Fluid-Solid Interaction Solution Algorithm

The FSI solver supports load transfer across a dissimilar mesh by using a linear search algorithm for the global search to locate the nodes belonging to the finite element mesh. It also uses a point to segment search algorithm for the local search to locate the nodal locations on an element face. Two interpolation methods the Conservative and the Non-Conservative are available for load transfer. The details of each interpolation technique are given in Table 4.

Table 4: Interpolation schemes for element types

Scheme	Element Types	Nodes
Conservative	Low order elements on the fluid and solid sides	Number of nodes on the fluid side is greater than the number of nodes on the solid side
Non-Conservative	High order elements on the solid side	Number of nodes on the solid side is greater than the number of nodes on the fluid side

5.3   MULTIPHYSICS ANALYSIS

The Multiphysics model used to simulate the drop generation mechanism was developed in three stages. The first stage included the development of a Computational fluid dynamic (CFD) analysis of the fluid domain from the PZT disc to the nozzle orifice. The second stage included the development of a coupled-field analysis for the PZT disc. Finally, when both of the individual domains are modeled, the third and final stage combines the interacting domains into an integrated Multiphysics analysis. The Multiphysics analysis not only performs superposition of the individual domains, but also implements interfacial parameters, redundant boundary conditions, and time step increments for all three stages of the analyses. This type of Multiphysics analysis captures the electrostatic-structural coupling using a direct-coupled field analysis and structural-fluid coupling using a sequential-coupled FSI technique. The typical procedure in a Multiphysics analysis with direct and sequential coupling methods is delineated below.

5.3.1   Fluid and Solid Analyses

To perform a fluid-solid interaction analysis, the first step is to create the fluid model and the finite element mesh for the fluid region [55]. The appropriate boundary conditions for the fluid region are then applied, and the material properties and solution control options are defined.

The solid model and the finite element mesh for the solid region [56] are then created and appropriate boundary conditions, material properties, and solution control options are applied.

5.3.2 Identification of Fluid-Solid Interfaces

The next step is to identify fluid-solid interfaces where load transfer takes place with a fluid-solid interface number. The field-surface interface is flagged twice: once for the fluid side of the interface and once for the solid side of the interface. Load transfer occurs between fluid and solid interfaces with the same interface number.

5.3.3 Specification of the Fluid-Solid Interaction Solution Options

Before performing an analysis, the fluid-solid interaction scheme is turned on and the solution order for the fluid and solid analyses must be set. The analysis that is driving the solution should be first since the physics of the problem determines the order of the analysis type. The solution end time and time step increment for the fluid-solid interaction analysis has to be specified. The end time should be a multiple of the time step increment. The fluid-solid interaction solver only supports constant time stepping. The time step increment for the solid and fluid analyses should be less than or equal to the time step increment for the FSI analysis. A fluid-solid interaction analysis sub-cycles over the fluid and solid analyses so that load transfers across the fluid-solid interface. The maximum number of stagger iterations between the fluid and solid analysis has to be specified. It applies to each time step in the fluid-solid interaction analysis. At the end of each stagger loop, the fluid-solid interaction solver checks the convergence of the quantities transferred across the interface. The analysis proceeds to the next time step if the interface quantities have converged or the maximum number of stagger iterations has been reached.

5.4   MODEL DEVELOPMENT

The Multiphysics model for the CIJ print head combines the fluid chamber CFD analysis and the coupled field PZT disc analysis. A brief description of the CFD and PZT analyses are provided followed by a detailed fluid-structural coupling model development.

5.4.1   CFD model of fluid chamber

The control volume (CV) of the fluid chamber is modeled using a Fluid141 planar element in the ANSYS® FLOTRAN software [57]. A Volume of Fluid – Continuum Surface force (VOF-CSF) algorithm [58] is used to track the evolution of free surface of the droplet in air. The control volume extends from the PZT disc interface through the nozzle orifice to the drop flight of path. Depending on the inlet pressure the control volume may be extended in length as the drop breakup occurs further ahead from the nozzle. The control volume is modeled axisymmetrically around the Y-plane to aid in the computational efficiency without compromising the accuracy of the solution. Similar to the PZT disc analysis the geometry of the CV permits the use of an axisymmetric model. Figure 29 shows the boundary conditions and applied loads on the CFD model. The high-pressure inlet tube carrying fluid to the chamber is the only geometry without symmetry. This is taken into account with an inlet boundary condition. The length of the inlet is equivalent to the fluid discharge rate of the high-pressure tubing. A pressure loading is applied on the equivalent length. The arrows in yellow denote the axisymmetric BC. The model can be rotated for 360° about its vertical central axis to obtain a 3D view. The velocities in the X and Y directions are set to zero for the side boundaries enclosing the control volume. (i.e. V_x and $V_y = 0$ as shown in the figure with red arrows). The total number of elements for the CFD model is 1685. The aspect ratio of elements is close to one with an

adequate mesh density to effectively capture the pressure wave propagations inside the fluid chamber.
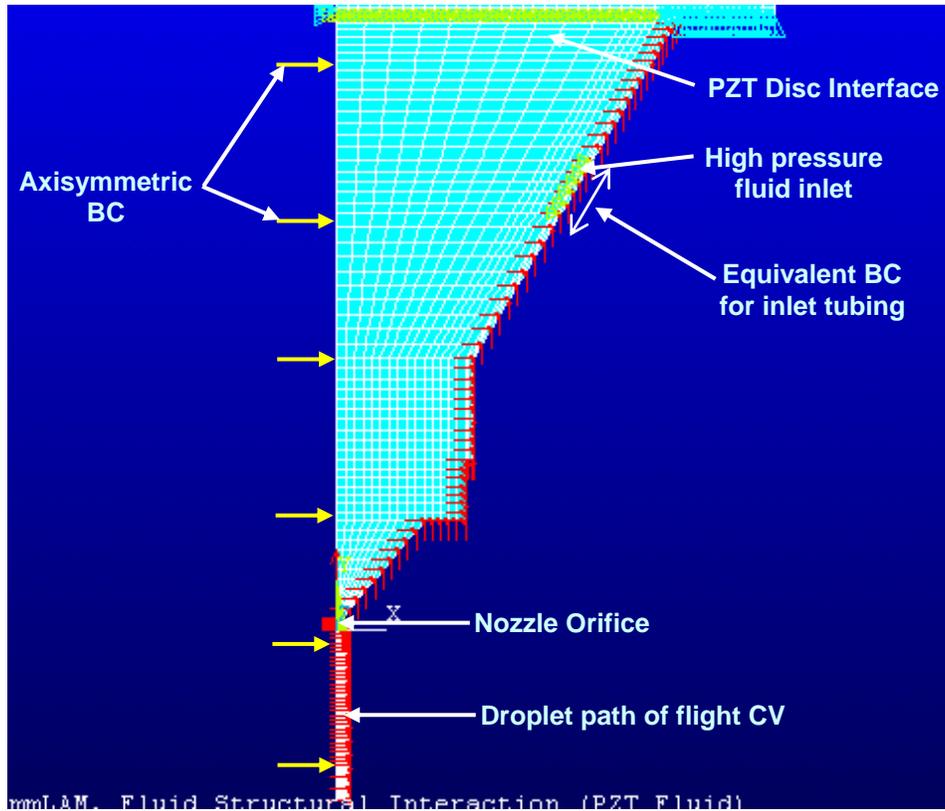
Figure 29: Boundary conditions and loading of CFD model

The effect of gravity is taken into account and the fluid pressure is applied at 40psi (275800 Pa) inside the fluid chamber. The fluid used in the analysis is an organic solvent Methyl Ethyl Ketone (MEK). The physical properties of the fluid are given in Table 5.

Table 5: Physical properties of MEK

Property	Notation	Value
Density (kg/m^3)	ρ	0.85e3
Dynamic Viscosity [kg/(m.s)]	μ	3.5e-3
Surface Tension (kg/m^2)	σ	2.5e-3

5.4.2 Coupled field analysis of PZT disc

The PZT disc section of the FSI analysis is modeled with a transient coupled field technique. The PZT disc is modeled using a PLANE223 coupled field element in the commercial ANSYS 8.0 software [59]. It is modeled axisymmetrically to aid compatibility with the CFD model. The dielectric constants (ε^s), piezoelectric strain coefficients (d) and compliance matrix (s^e) for the bimorph material Lead Zirconate Titanate (PZT-5A) are given in Figure 30 [60].

$$[s^E] = \begin{bmatrix} 16.4 & -5.74 & -7.22 & 0 & 0 & 0 \\ -5.74 & 16.4 & -7.22 & 0 & 0 & 0 \\ -7.22 & -7.22 & 18.8 & 0 & 0 & 0 \\ 0 & 0 & 0 & 47.5 & 0 & 0 \\ 0 & 0 & 0 & 0 & 47.5 & 0 \\ 0 & 0 & 0 & 0 & 0 & 44.3 \end{bmatrix} \times 10^{-12} m^2 / N \qquad [\varepsilon^s] = \begin{bmatrix} 1.53 & 0 & 0 \\ 0 & 1.53 & 0 \\ 0 & 0 & 1.505 \end{bmatrix} \times 10^{-8} F / m$$

$$[d] = \begin{bmatrix} 0 & 0 & -171 \\ 0 & 0 & -171 \\ 0 & 0 & 374 \\ 0 & 0 & 0 \\ 0 & 584 & 0 \\ 584 & 0 & 0 \end{bmatrix} \times 10^{-12} C / N$$

Figure 30: Mechanical and piezoelectric properties for PZT bimorph disc

The boundary conditions and voltage loading are shown in Figure 31. The PZT has a radius of $r = 2.55e\text{-}3m$ and the thickness of the individual bimorph layer $h = 0.32e\text{-}3m$. The piezoelectric bimorph disc is clamped on its top and bottom periphery thereby constraining its displacement in the Ux and Uy directions. The left edge is constrained in the Ux direction to reflect the axisymmetric boundary conditions. The disc is excited by a 60V AC input signal at 80kHz applied on the top surface where the annular electric leads rest on the disc. The bottom surface is grounded by virtue of contact with conductive fluid (MEK).
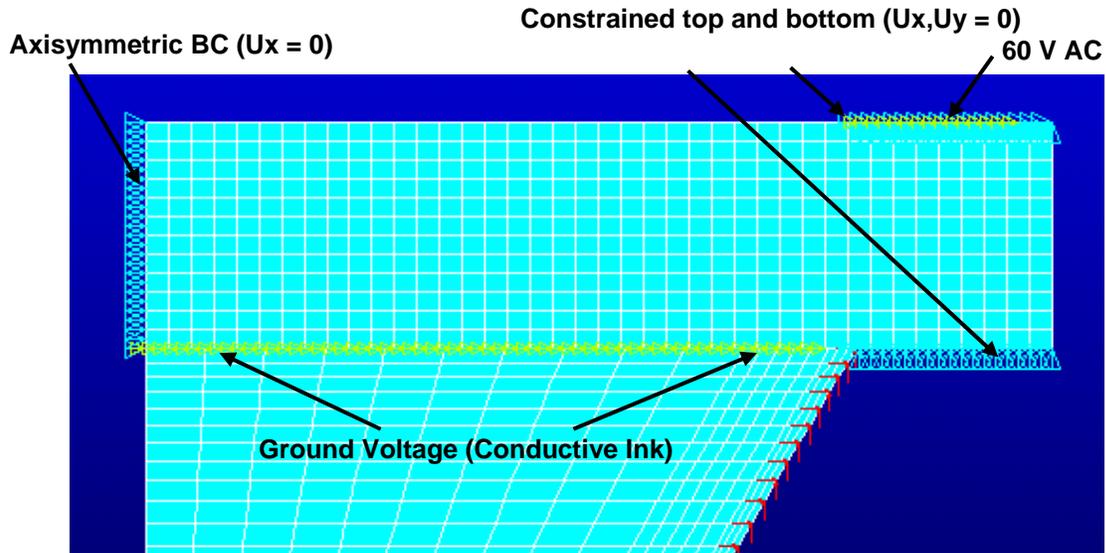
Figure 31: Boundary conditions and voltage loading on axisymmetric PZT disc

5.4.3 FSI model development

The final stage of the analysis involves combining the CFD and PZT disc model into a single Multiphysics model. The CFD model developed above is built and the top wall is flagged as a fluid interface. Similarly the PZT disc model developed above is built after the fluid model and is identified at its bottom layer as a solid interface. As shown in Figure 32 both these flags have a common flag number (FSIN = 1) that corresponds to a fluid-solid interface. The interaction of the fluid and the structure at a mesh interface causes the acoustic pressure to exert a force applied to the structure and the structural motions produce an effective "fluid load." The length of the fluid control volume from the nozzle orifice to the substrate is 1mm. This length is intentionally shortened to limit the number of elements for the FSI model. Shortening this length does not affect the PZT displacement characteristics. The PZT displacement characteristics is influenced by the fluid behavior within the CV, which extends from the PZT disc to the nozzle. The dynamics of the fluid after breakup does not influence the upstream fluid behavior within

the fluid chamber. The width of the fluid control volume is minimal enough to accommodate the maximum drop radius. Depending on the input excitation parameters the drop radius varies from 2 to 3 times the orifice radius. In this case the orifice radius is 30microns, thus the control volume width during droplet path of flight is limited to 80microns. The length and width of the CV in the droplet path of flight region were restricted since this region plays a minimal role in determining the PZT disc displacement behavior. However the rest of the fluid chamber CV was modeled with an adequate mesh density to simulate the fluid behavior in the vicinity of the fluid-solid interface. The total number of elements for the Multiphysics analysis was [solid (480) + fluid (1685)] = 2165 elements.

As the solid analysis is the driving physical phenomenon in the case of the CIJ simulation, its solution order is set first followed by the fluid analysis. The maximum number of stagger iterations between the fluid and solid analysis per time step is set to 10. A non-conservative interpolation method is employed for the FSI solver, as there are higher order elements on the solid side. The time increment for solid, fluid and FSI analysis is set to $t_{inc} =$ 6.25e-7 seconds. The time increment is based on the time period for the input voltage cycle. For an 80kHz PZT frequency the time period is 12.5 microseconds. This cycle is divided into 20 sub steps to obtain the $t_{inc} =$ 6.25e-7 seconds which can effectively capture the sinusoidal waveform of the input excitation. The end time is a multiple of the time step increment that tracks the first 15 cycles of the excitation. Thus $t_{end} =$ 15*20*6.25e-7 = 1.875e-4 seconds. The solid and fluid output results are saved separately for each time step.
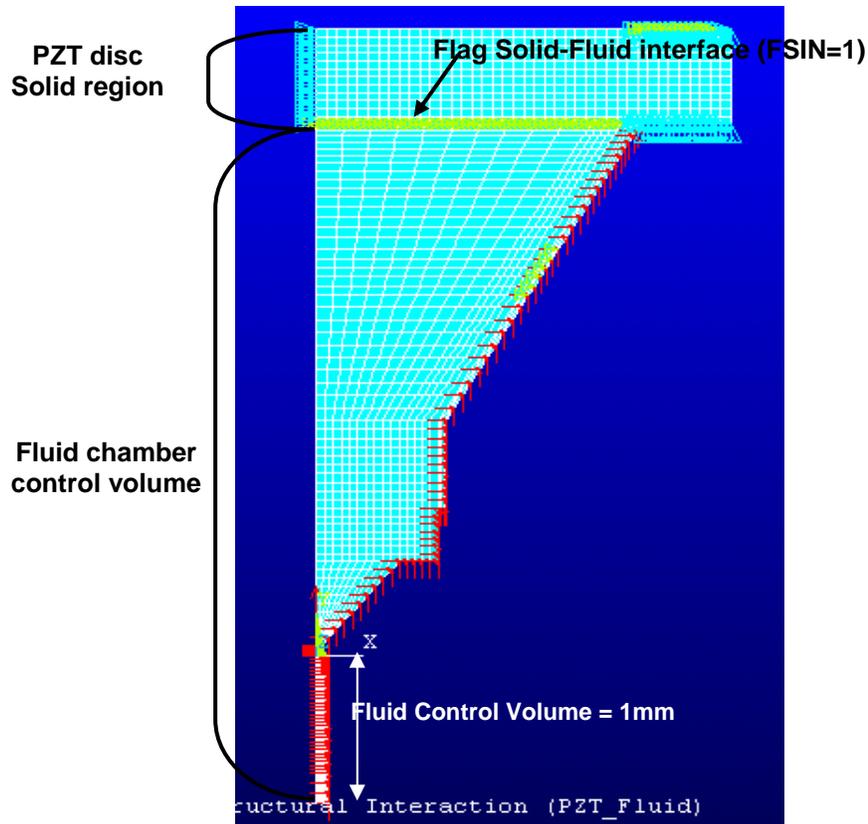
Figure 32: Boundary conditions on axisymmetric Multiphysics model

The Multiphysics analysis requires substantial computing resources to obtain a steady state solution for the droplet formation. To give an estimate, it takes around 250 hours (approx 10 days) to reach a steady state solution level. The Multiphysics model used for these computations is identical to the one discussed above with the exception of an additional fluid control volume length from nozzle orifice to substrate. It has been observed from experimental results that the drop breakup occurs at 5 to 6 mm from the orifice and stable spherical drops are observed beyond 9mm in length from the nozzle orifice. This is particularly true for a fluid chamber with a pressure of 40psi. In order to observe the droplet formation behavior this length was extended from 1mm to 12mm. The model was run using an Intel Pentium4 machine with

1Gb of RAM. The FSI analysis saves the solid and fluid results files separately, which totaled to 5 GB of hard disk space for the initial 5 milliseconds of inkjet simulation.

Given the exhaustive computing resource requirements for the FSI analysis, an alternate method is devised to obtain steady state droplet formation. In a Multiphysics analysis, the transfer of the PZT disc displacement to the fluid domain via the interface simulates the drop formation behavior. As shown in Chapter 4 (PZT) the interaction of solid-fluid domains captures the dampening effect on the PZT disc. This gives an accurate estimate of the PZT displacement, that would not be captured with a PZT disc vibrating in free air. Now that we have the true PZT displacements in contact with fluid we can superimpose these values as boundary conditions on a purely fluid model (CFD analysis). We are therefore running only a single analysis type that reduces both the computation time and the complexity of the algorithm to obtain equivalent results as the FSI algorithm. However we still need the FSI analysis to obtain the true PZT disc displacements when in contact with fluid media. The Multiphysics analysis is an intermediate stage that feeds into the final CFD analysis.

5.5   MULTIPHYSICS MODEL RESULTS

The Multiphysics model developed in this chapter was extended to simulate the fluid-structural interactions and to obtain the PZT displacements for different input conditions. These PZT displacements were superimposed as boundary conditions on the CFD model presented in Chapter 6. In order to ascertain the effect of input pressure on the PZT disc displacement, four models were built with inlet pressures of 5, 10, 20 and 40 psi respectively. The models resemble the above-developed FSI model with excitation frequency of 80kHz at 60V AC. Figures 33, 34,

35, and 36 show the PZT displacement characteristics over the first 15 excitation cycles for 5, 10, 20 and 40 psi respectively.
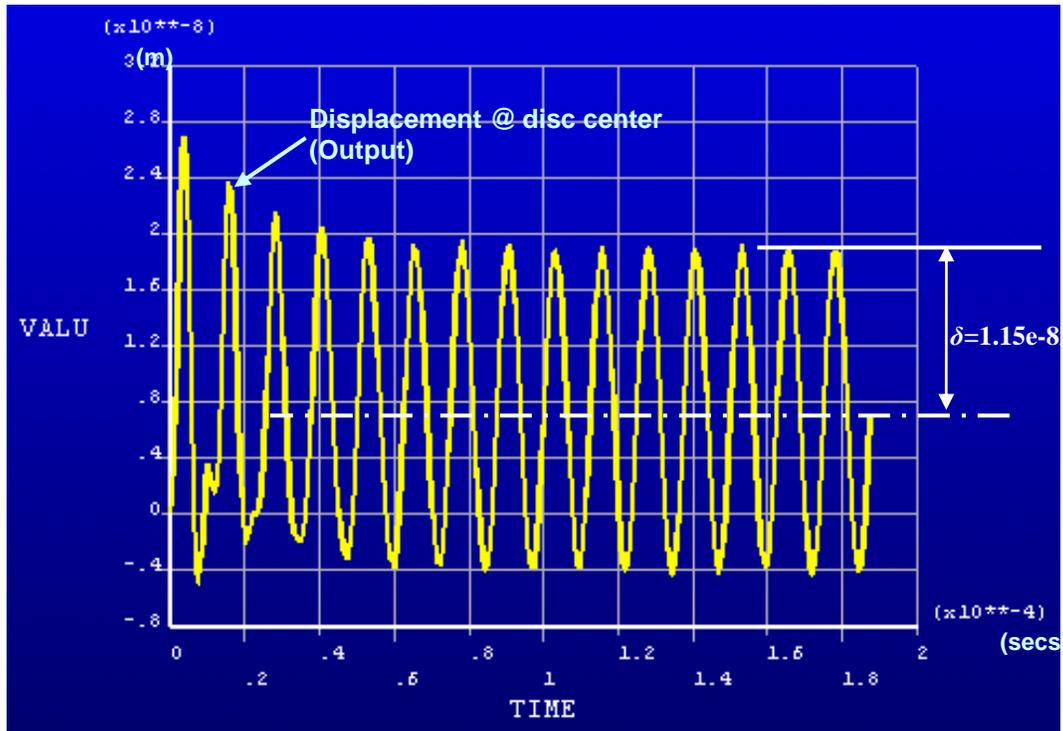
Figure 33: PZT disc displacement at 5psi, 80kHz, 60V, with DISP = 0.0115μm

It is important to note that the PZT disc displacement occurs on the positive side of the mean value, which is zero. This can be attributed to a positive head on the lower layer of the PZT disc due to high incoming fluid pressure. Though the fluid chamber has an aperture in the nozzle, it is small enough to permit a pressure head balance with ambient pressure, thereby causing the PZT disc to deflect and prestress in the upward direction for the above configuration. After an initial transient period (initial 2 cycles), the displacement waveform stabilizes in amplitude with the mean position around 7.5e-9m. The steady state displacement amplitude of the PZT disc is δ = 1.15e-8m.
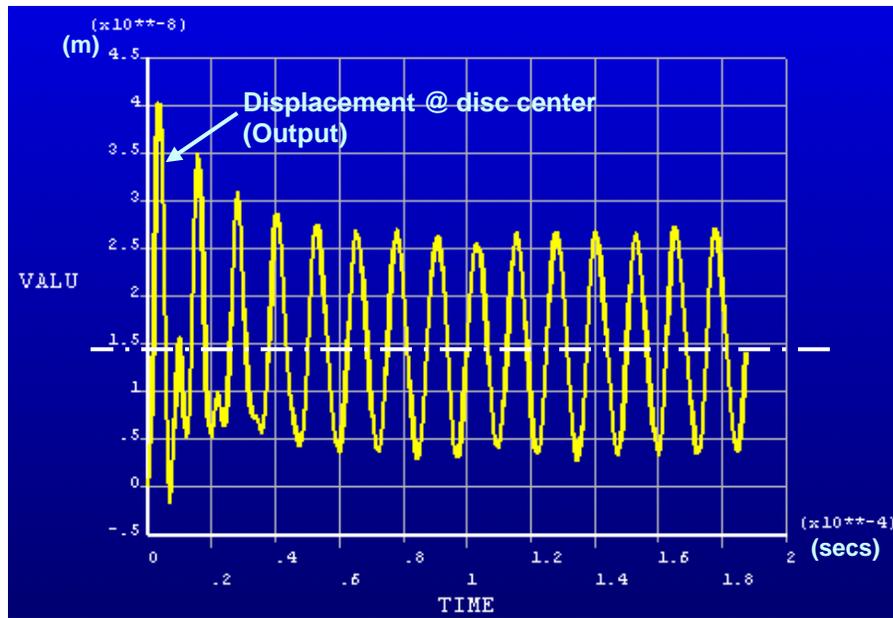
Figure 34: PZT disc displacement at 10psi, 80 kHz, 60V, with DISP = 0.012μm

The PZT displacement for cases with 10 and 20 psi inlet pressures is δ = 1.2e-8m. As shown in Figures 34 and 35, the PZT disc displacements show a transient pattern during the early cycles. The offset of mean position from zero increases with an increase in inlet pressure. The mean position for 10 and 20psi inlet pressures is around 1.5e-8m and 3.0e-8m respectively.
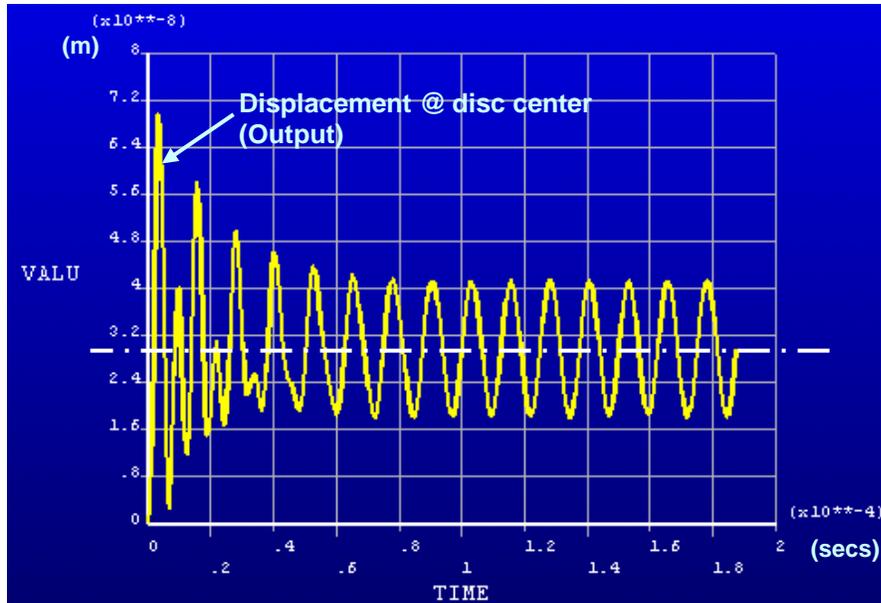
Figure 35: PZT disc displacement at 20psi, 80 kHz, 60V, with DISP = 0.012μm
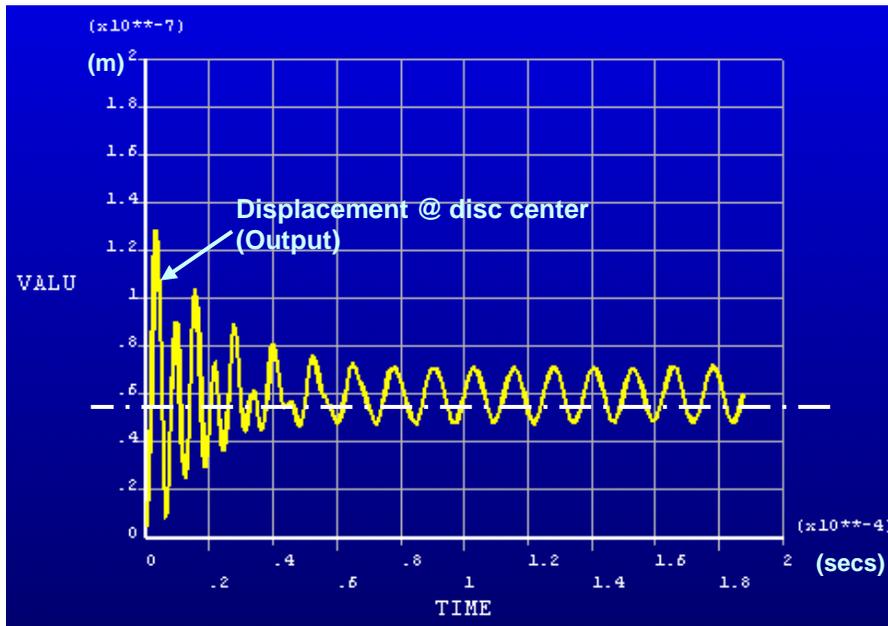
Figure 36: PZT disc displacement at 40psi, 80kHz, 60V, with DISP = 0.0115μm

In the case of an inlet pressure of 40psi, the transient behavior of the PZT displacement waveform lasts for approximately 50μs. The mean position for PZT displacement amplitude in the 40psi case is near 6.0e-8m, which is the highest among all the four cases considered. It is important to note, however, that the average PZT displacement amplitude under steady state conditions is δ = 1.2e-8m. We can therefore conclude that although the higher inlet pressures deflect and prestress the PZT disc in one direction, the average displacement amplitudes remain the same. Thereby we can utilize the average displacement amplitude from a single Multiphysics model and superimpose it as a valid boundary condition on the CFD model. This is true for simulating other models with varying pressures given that rest of the excitation inputs remain identical.
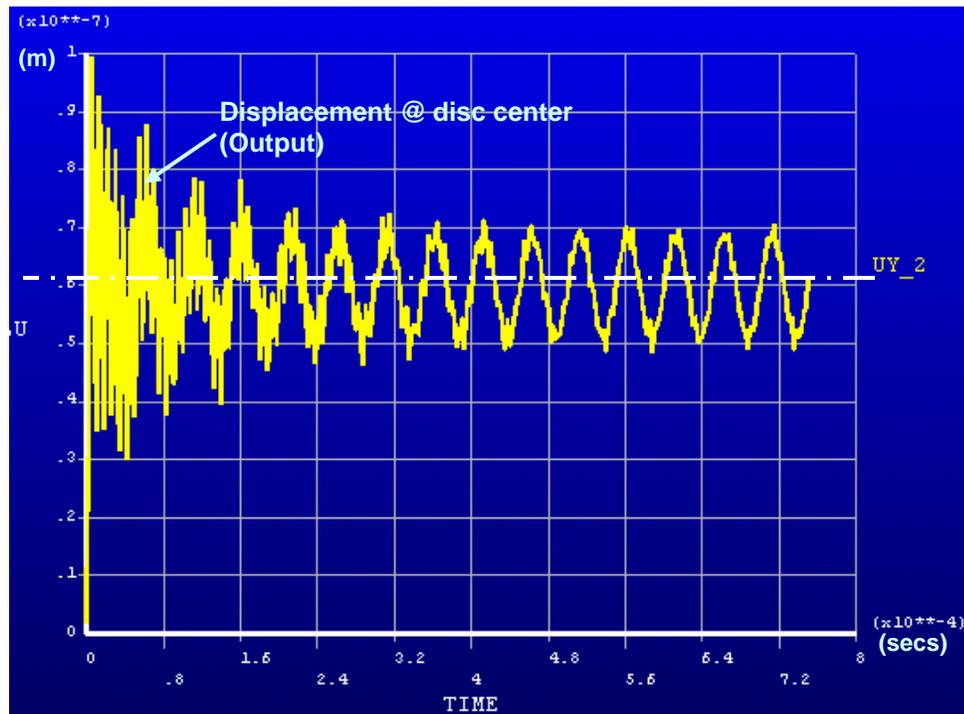
Figure 37: PZT disc displacement at 40psi, 20 kHz, 60V, with DISP = 0.0105μm

As shown in Figure 37 the PZT displacement decreases from δ = 1.2e-8m in the case of 80 kHz excitation to δ = 1.05e-8m in the case of 20 kHz modulation frequency. A 12.5% decrease in PZT displacement is observed between the two frequencies. At a higher frequency the time required to reverse a displacement cycle is reduced, allowing the PZT disc to attain higher velocities to traverse from peak to peak of the waveform. As a result, the PZT disc attains higher kinetic energy and forces itself to higher amplitudes as compared with a lower frequency input signal. Another observation made in Figure 37 is that the displacement waveform for 20 kHz frequency is slightly jagged as compared to a similar waveform for 80 kHz excitation signal shown in Figure 34. The mean position of waveform oscillation, however, stays steady at 5.95e-8m in both cases due to a 40psi inlet pressure. The above difference indicates that a higher excitation frequency increases the PZT displacement, maintaining the same mean position of oscillation.
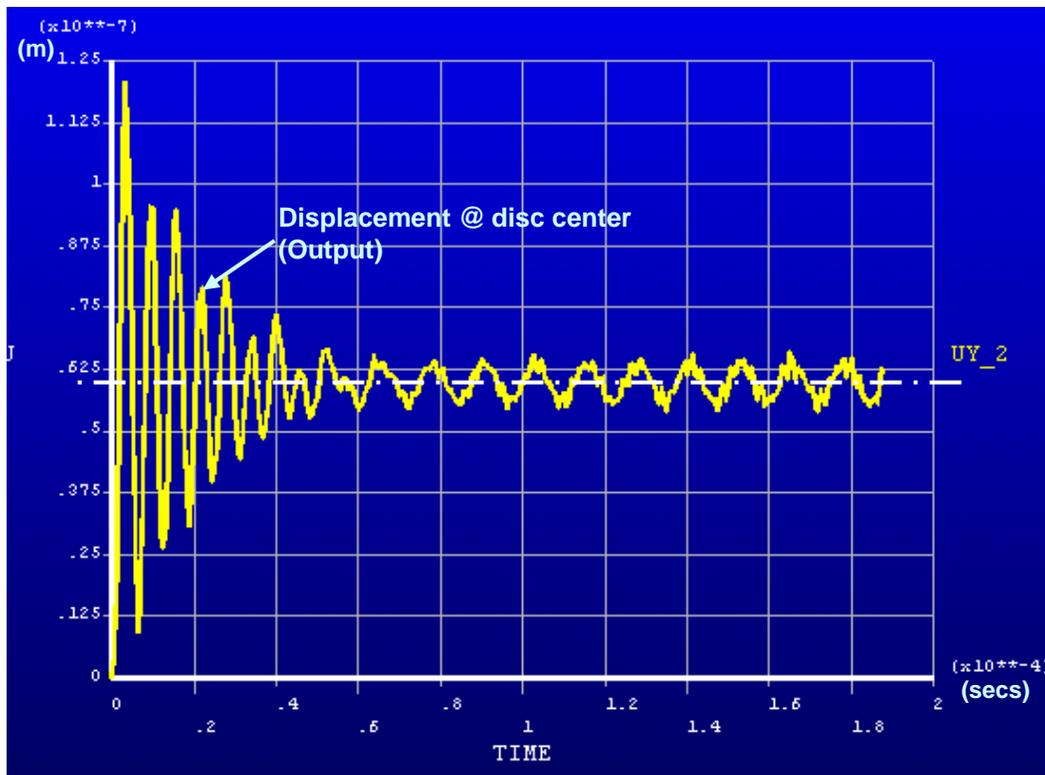
Figure 38: PZT disc displacement at 40psi, 80 kHz, 20V, with DISP = 0.0045μm

Figure 38 shows the PZT disc displacement at lower amplitude of excitation voltage, which is 20V AC. This is lower than the earlier applied voltage of 60V, which results in lower PZT disc displacements. The steady state amplitude of PZT displacement with 20V input signal is δ = 4.5e-9m. This value is correspondingly lower than the 1.15e-8m displacement for the 60V input signal. However the mean position for oscillations remains steady at 5.95e-8m in both the 20V and 60V cases due to identical inlet pressure of 40psi.

6.0   COMPUTATIONAL FLUID DYNAMIC ANALYSIS OF CIJ SYSTEM

6.1   INVESTIGATION OF DROP FORMATION MECHANISM

In the CIJ printing method a fluid jet is perturbed with a source of acoustic energy to form standing wave nodes along the jet length. The standing wave maxima along the fluid stream condense into discrete microdrops [61]. The piezoelectric disc stimulation produces velocity disturbances that grow through the physico-chemical [62] properties of the fluid (i.e. surface tension) until the jet breaks into uniform drops [63]. In the past researchers have modeled the liquid jet break-up and drop formation using approximate analytical techniques such as the stream-tube method [64]. For the flow of an incompressible fluid, the Navier-Stokes equations of motion and continuity equation can be solved simultaneously under specific boundary conditions to obtain an exact solution. Since the Navier-Stokes equations are non-linear, however, it is difficult to obtain an analytical solution [65] for nontrivial problems. By omitting the inertia terms for a flow whose Re is small (slow flow around a sphere), or by neglecting the viscosity term for a flow whose Re is large (fast free-stream flow around a wing), approximate solutions have been documented. For intermediate Re, the equations cannot be simplified because the inertia term is roughly as large as the viscosity term and there is consequently no method for obtaining the approximate solution numerically. For this reason, the complexity of the CIJ process demands the use of numerical and experimental solution techniques.

Experimental studies have been carried out to study the stability of drops during droplet path of flight [66]. These experimental techniques have not been able to capture the spatio-temporal phenomena within the drop formation mechanism. Earlier attempts to capture ink-jet evolution, drop formation, and impingement on a substrate have been limited to microscopic high speed photography where a LED strobe is synchronized with the rate of drop formations. Such calibration techniques do not provide an understanding of the transport phenomena such as pressure and turbulence, which are critical in achieving optimal jet flow.

6.2   ALTERNATE MODELING STRATEGY

With limitations in theoretical and experimental analysis techniques, it is essential to develop a comprehensive methodology to model the complex CIJ system. A prudent way to achieve this objective is by conducting a parametric Computational Fluid Dynamic (CFD) Analysis of CIJ. Alternative Multiphysics techniques may also be utilized to solve the droplet formation problem. Although the Multiphysics analysis simulates interacting domains, it is computationally expensive on two fronts. As mentioned in Chapter 5, the Multiphysics analysis iterates betweens domains, which generates higher volumes of data and requires longer convergence times. These issues can be avoided with the use of a CFD analysis which is restricted to a single domain and is far more efficient on system memory and convergence times. The CFD analysis is ideal when the original problem is represented by relevant boundary conditions.

In this Chapter a CFD analysis will be performed to assist in identifying critical input parameters for optimizing drop generation. The Multiphysics analysis conducted in Chapter 4

provides the input boundary conditions for the CFD model. The first step is to record the PZT disc displacement amplitude in Multiphysics analysis under steady state conditions. This displacement is then superimposed as a Simple Harmonic Motion (SHM) boundary condition on the top wall of the CFD model.

6.3   FREE SURFACE ANALYSIS OF CIJ SYSTEM

In the CIJ system the evolving fluid jet is in contact with the surrounding air and breaks into droplets. A free surface analysis is used to solve this type of problem involving a unconstrained gas-liquid surface. A two dimensional axisymmetric analysis was conducted in the commercial software ANSYS FLOTRAN$^{®}$. The software employs a Continuum Surface Force - Volume of Fluid (CSF-VOF) [37] algorithm to track the free surface evolution during the droplet path of flight.

In a Volume of Fluid (VOF) analysis, FLOTRAN uses an advection algorithm for the volume fraction (VFRC) to track the evolution of the free surface. The VFRC value for each element varies from zero to one, where zero denotes an empty or void element and one denotes a full or fluid element. The values between zero and one indicate that the corresponding elements are the partially full or surface elements (henceforth called partial elements), and the free surface can thus be determined by the distribution of the VFRC field.

For the dynamic behavior at the interface between a gas and liquid, FLOTRAN uses a continuum surface force (CSF) method to model the surface tension. Surface tension is an inherent characteristic of material interfaces. It is a localized surface force acting on the interface. FLOTRAN reformulates this surface force into an equivalent volumetric force in the

momentum equation. This force consists of two components: a normal component to the interface due to local curvature and a tangential component to the interface due to local variations of the surface tension coefficient.

In the current version of FLOTRAN, VOF capability is only available for quadrilateral elements for two dimensional planar or axisymmetric analyses. For a VOF analysis, boundary conditions are required for boundary nodes that belong to at least one non-empty (partial or full) element. This is because the VFRC boundary conditions determine if there exists a fluid inlet or outlet at the boundary nodes.

6.4   VOLUME OF FLUID (VOF) ALGORITHM

A free surface refers to an interface between a gas and a liquid where the difference in the densities between the two is quite large. Due to a low density, the inertia of the gas is usually negligible, so the only influence of the gas is the pressure acting on the interface. Hence, the region of gas need not be modeled, and the free surface is simply modeled as a boundary with constant pressure. The volume of fluid (VOF) method determines the shape and location of the free surface based on the concept of a fractional volume of fluid. A unity value of the volume fraction (VFRC) corresponds to a full element occupied by the fluid (or liquid in the CIJ simulation), and a zero value indicates an empty element containing no fluid (or gas in the CIJ simulation). A VFRC value between zero and one indicates that the corresponding element is the partial (or surface) element. In general, the evolution of the free surface is computed either through a VOF advection algorithm or through the equation 6.1 [67]:

$$\frac{\partial F}{\partial t} + \vec{u} \bullet \nabla F = 0 \tag{6.1}$$

where,

F = volume fraction (or VFRC)

In order to study complex flow problems, an original VOF algorithm has been developed that is applicable to the unstructured mesh.

6.4.1   CLEAR-VOF Advection

CLEAR stands for Computational Lagrangian-Eulerian Advection Remap. This algorithm takes a new approach to compute the fluxes of fluid originating from a home element towards each of its immediate neighboring elements. Here, these fluxes are referred to as the VFRC fluxes. The idea behind the computation of the VFRC fluxes is to move the fluid portion of an element in a Lagrangian sense, and compute how much of the fluid remains in the home element, and how much of it passes into each of its neighboring elements. This process is illustrated in Figure 39 [68]

(a) Original polygon (P_1,P_2,P_3,P_4) of fluid in the home element with VFRC = 0.5

(b) Advected polygon (P_1',P_2',P_3',P_4') of fluid in the next time step

(c) Intersection of the advected polygon with the neighboring elements.

(d) Update the new area and the VFRC value for the home element.
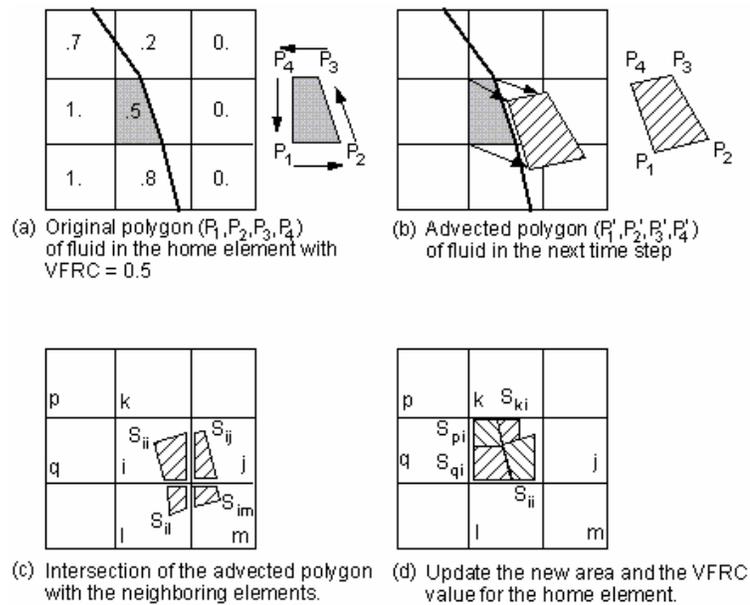
Figure 39: Typical Advection Step in CLEAR-VOF Algorithm

6.4.2   Treatment of Surface Tension Field

In a VOF analysis, the surface tension is modeled through a continuum-surface force (CSF) method. As described earlier, there are two components in this surface force. The first one is normal to the interface due to the local curvature, and the second one is tangential to the interface due to local variations of the surface tension coefficient. In this approach, the surface force localized at the fluid interface is replaced by a continuous volume force to fluid elements everywhere within a thin transition region near the interface. The CSF method removes the topological restrictions without losing accuracy [69], and it has thus been used widely and successfully in a variety of studies [70,71,72,73].

The surface tension is a force per unit area given by equation 6.2:

$$\vec{f}_s = \sigma \kappa \, \hat{n} + \nabla_{\hat{t}} \sigma \tag{6.2}$$

where,

$\vec{f}_s$ = surface force

σ = surface tension coefficient

κ = surface curvature

$\hat{n}$ = unit normal vector

$\nabla_{\hat{t}}$ = surface gradient

6.5   ARBITRARY LAGRANGIAN-EULERIAN (ALE) FORMULATION

A free surface evolution by itself offers a challenge, which can be dealt with numerically using either an Eulerian or Lagrangian approach. The Eulerian approach involves the use of discretization mesh that remains fixed in space with the flow moving through it, while in the Lagrangian approach the mesh in convected with the flow. The major drawback of the Lagrangian approach is that only simple nonintersecting interfaces can be represented due to a limitation on the amount of mesh distortion allowed. The disadvantage of Eulerian approach is that a fine mesh is required to capture the fluid response, making the method very computationally expensive. An alternate approach called as the Arbitrary Lagrangian Eulerian (ALE) is used to model free surface development.

The general concept of the ALE formulation is that an arbitrary referential domain is defined for the description of motion that is different from the material (Lagrangian) and spatial (Eulerian) domains [74].

6.6   FLUID FLOW MATRICES AND SEGREGATED SOLUTION ALGORITHM

A segregated, sequential solution algorithm is used [75]. The element matrices are formed, assembled and the resulting system solved for each degree of freedom separately. Development of the matrices proceeds in two parts. In the first, the form of the equations is achieved and an approach is taken towards evaluating all of the terms. Next, the segregated solution algorithm is outlined and the element matrices are developed from the equations.

Each degree of freedom is solved in sequential fashion. The equations are coupled, so that each equation is solved with intermediate values of the other degrees of freedom. The

process of solving all the equations in turn and then updating the properties is called a global iteration.

6.7   CONTROL VOLUME (CV) FOR CFD ANALYSIS
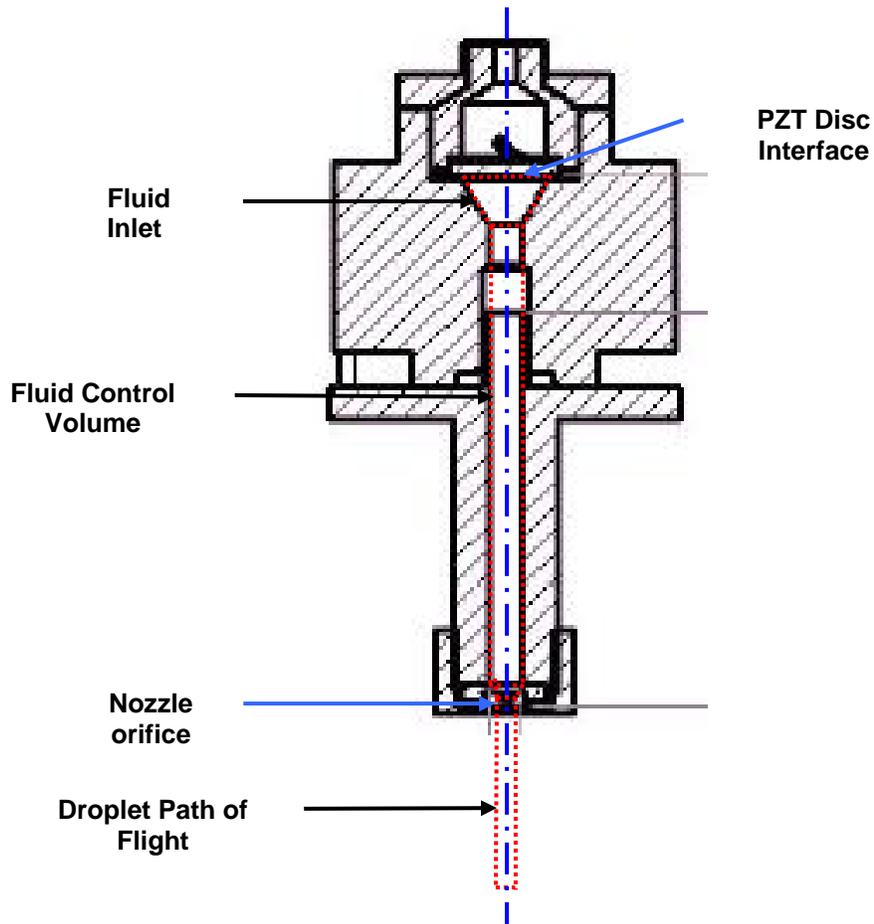
Figure 40: Control Volume for CFD Analysis

Figure 40 shows the cross sectional view of the fluid chamber within the PZT modulator assembly. The region demarcated by red dotted lines is the control volume for the CFD analysis. The fluid domain is modeled from the PZT disc interface to the nozzle orifice. The high-pressure

inlet tube is modeled as a boundary condition with equivalent discharge at high pressure. The lower end of the control chamber extends through the nozzle orifice to the droplet path of flight. The length of the droplet path of flight is modeled depending on the inlet fluid pressure. A higher inlet pressure corresponds to a higher orifice exit velocity, and thereby a longer CV length in the droplet path of flight region.

The droplet is allowed to exit from the control volume after a limited path of flight, which is represented with an open wall boundary condition. The width of the control volume during the droplet path of flight is marginally higher than the average droplet radius. Based on the input excitation characteristics the final droplet radius varies from 2 to 3 times the orifice radius. It is important to restrict the total number of elements within the CV to obtain results within a reasonable time frame without compromising on the accuracy of the solution.

6.8   CFD MODEL DEVELOPMENT

The control volume (CV) (as shown in Figure 38) is modeled using a Fluid141 [76] planar element. The FLUID141 element is used to model transient or steady state fluid/thermal systems that involve fluid and/or non-fluid regions. The conservation equations for viscous fluid flow and energy are solved in the fluid region, while only the energy equation is solved in the non-fluid region. For the FLUID141 element, the velocities are obtained from the conservation of momentum principle, and the pressure is obtained from the conservation of mass principle. The temperature, if required, is obtained from the law of conservation of energy. A segregated sequential solver algorithm is used; that is, the matrix system derived from the finite element discretization of the governing equation for each degree of freedom is solved separately. The

flow problem is nonlinear and the governing equations are coupled together. The sequential solution of all the governing equations, combined with the update of any temperature or pressure-dependent properties, constitutes a global iteration. The number of global iterations required to achieve a converged solution may vary considerably, depending on the size and stability of the problem. Transport equations are solved for the mass fractions of up to six species.

The degrees of freedom are velocities, pressure, and temperature. Two turbulence quantities, the turbulent kinetic energy and the turbulent kinetic energy dissipation rate, are calculated if the optional turbulence model is invoked.
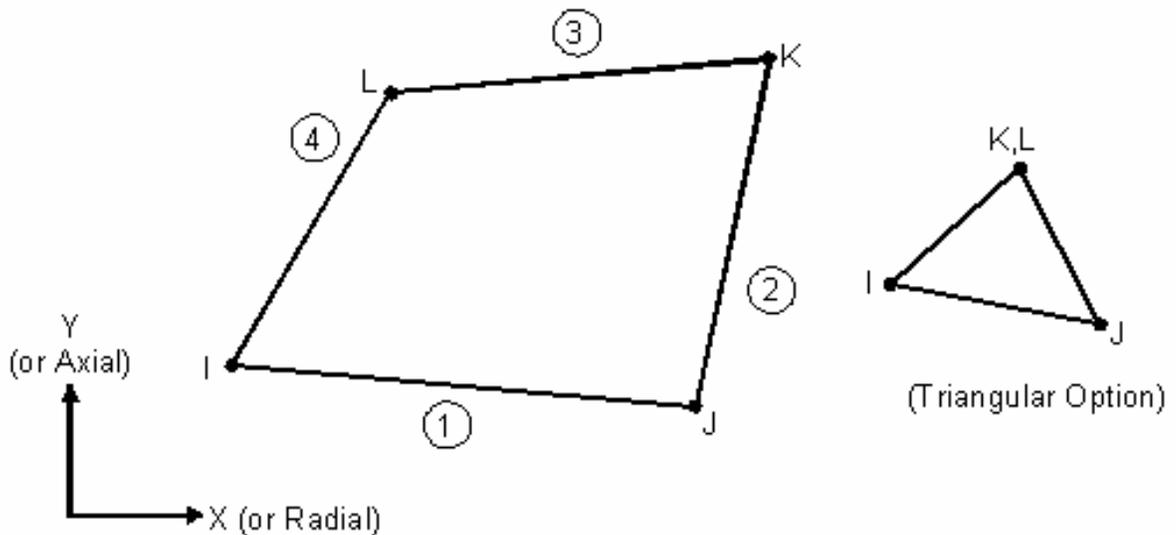
Figure 41: FLUID141 element geometry

Figure 41 shows the geometry, node locations, and the coordinate system for element FLUID141. The element is defined by three nodes (triangle) or four nodes (quadrilateral) and by

isotropic material properties. The coordinate system may be selected as Cartesian, axisymmetric, or polar.
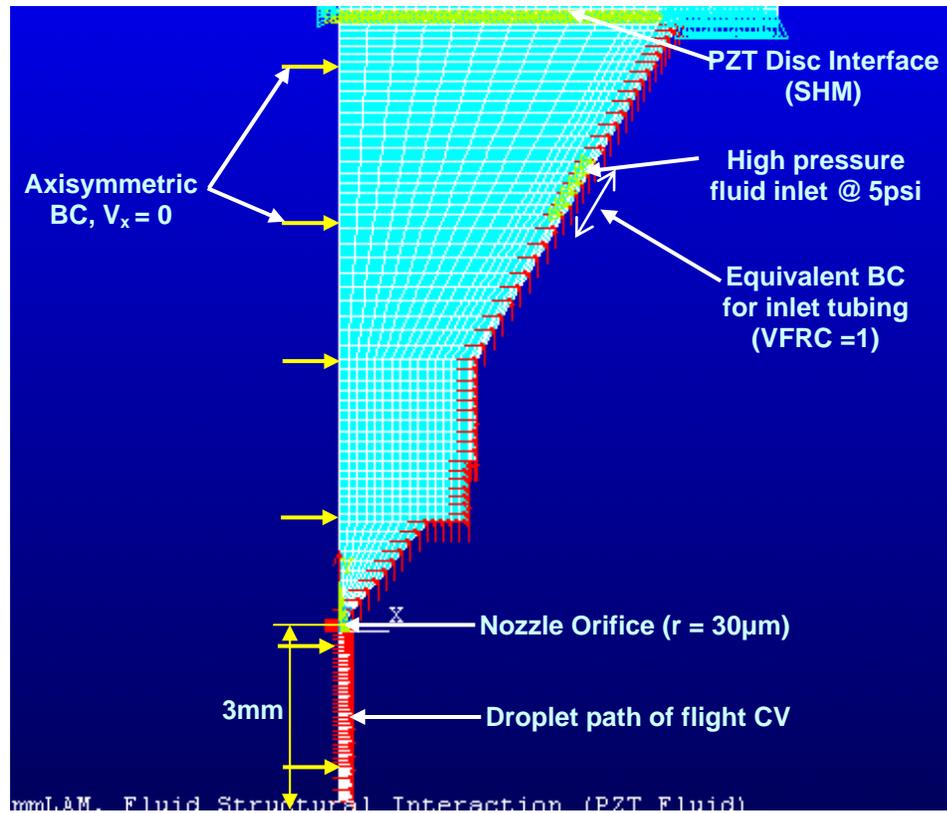
Figure 42: Boundary conditions applied to the CFD model

The control volume was modeled axisymmetrically around the Y-plane to aid in computational efficiency without compromising the accuracy of the solution. Figure 42 shows the boundary conditions and the loads applied to the CFD model. The high-pressure inlet tube carrying the fluid to the chamber is the only geometry without symmetry. This was taken into account using an inlet boundary condition. The length of this inlet is equivalent to the fluid discharge rate of the high-pressure tubing. A pressure loading was applied on this equivalent length. Figure 43 shows the equivalent areas for both a pipe and an axisymmetric boundary condition inlet. The pipe inlet area is given by,

$A_1 = \pi r^2$

Where, r is the radius of the pipe = 1000 μm
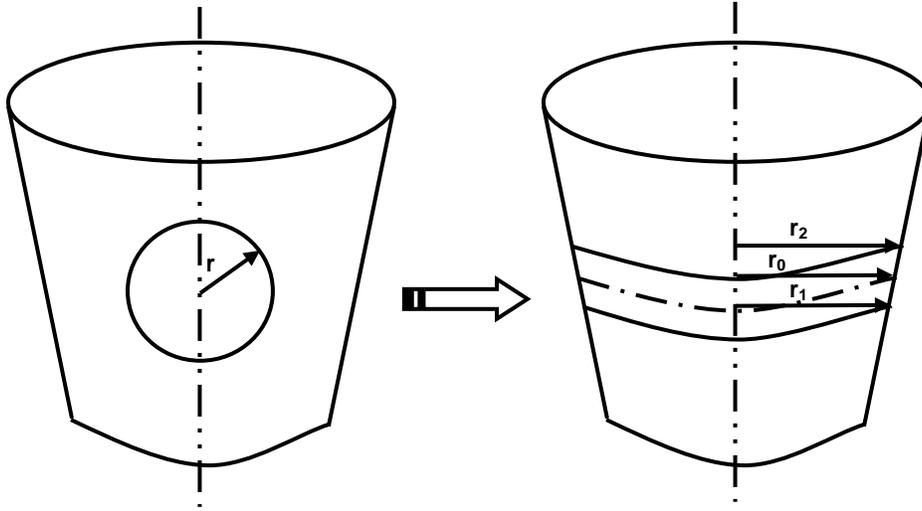
Figure 43: Equivalent inlet area for axisymmetric CFD model

The equivalent boundary condition is the pressure applied to the surface of the frustum of a cone, whose area is given by,

$A_2 = \pi (r_1 + r_2)/2 \times 2 \times s$ or $A_2 = \pi r_0 \times 2 \times s$

Where, r_1, r_0 and r_2 are radii of the frustum of cone at the bottom, middle and top layers along the axis. The value of $r_0 = 1400$ μm was chosen at the identical location of the center of the pipe inlet. To obtain the values of r_1 and r_2 the areas A_1 and A_2 were equated by substituting for r and r_0.

$\pi r^2 = \pi r_0 \times 2 \times s$

Thus, s = 357.142 μm, which is the slant height of the frustum of cone. Using trigonometric relations, the radii r_1 = 1491.874 and r_2 = 1308.126 were calculated for the axisymmetric CFD model. A VFRC = 1 (i.e. fluid inlet condition) and pressure loading of 5psi was applied to this area, which is represented by the slant height (s) shown in Figure 42.

The top wall of the CFD model was given a simple harmonic motion (SHM) displacement to mimic the vibration of the piezoelectric crystal. The displacement values for the amplitude of the SHM were obtained from the Multiphysics analysis. The axisymmetric BC was denoted with $V_x = 0$ and the model could be rotated for 360° around its vertical central axis to obtain a 3D view. The total number of elements for the axisymmetric CFD model was 26655. The aspect ratio of elements was close to one with an adequate mesh density to effectively capture the pressure wave propagations inside the fluid chamber. The effect of gravity was taken into account.

6.8.1 Fluids

There were two fluids used for the CFD analysis, namely water and 5nm Hexanethiol Nano gold in Toluene. Water was used for the initial model to describe the breakup phenomena and for comparison to the experimental results (see Chapter 7). The CFD results described in section 6.10 were obtained using 5nm Hexanethiol Nano gold in Toluene. The physical properties and composition of individual fluids are tabulated in the relevant sections.

6.8.2 Boundary Conditions

- Initial Conditions: Velocities for the entire model (Control Volume) were set to zero. Vx and Vy = 0.

- Substrate end: The substrate was modeled as an open wall with $V_x = V_y = 0$,

     where, V_x and V_y are velocities in the x and y directions respectively.

- Side boundary wall: The velocities in the x and y directions were set to zero for the side boundaries enclosing the control volume. i.e. V_x and $V_y = 0$.

6.8.3 Loading

A fluid pressure of 5psi (34475 Pa) was applied at the tube inlet along with a wetting boundary condition (VFRC = 1). The combination of wetting boundary status and pressure represents mass flow rate.

6.8.4 Solution Parameters

- Algorithm: The Arbitrary Lagrangian Eulerian (ALE) formulation described earlier in this chapter was used to track the free surface evolution and flow. This method is more accurate than the conventional Eulerian approach.

- Flow regime: The distinction between laminar and turbulent flow lies in the ratio of the inertial transport to the viscous transport. As this ratio increases, instabilities develop and velocity fluctuations begin to occur. A turbulent model accounts for the effect of these fluctuations on the mean flow by using an increased viscosity, the effective viscosity, in the governing equations. The effective viscosity given in equation (6.3) is the sum of the laminar viscosity (which is a property of the fluid) and turbulent viscosity (which is calculated from a turbulence model).

$$\mu_e = \mu + \mu_t \tag{6.3}$$

where,

μ_e: effective viscosity

μ: laminar viscosity

μ_t: turbulent viscosity

Generally, the more turbulent the flow field, the higher the effective viscosity. For the geometry of the CIJ print head a number of initial simulations were run using the turbulent

model. The values of effective viscosity were calculated at regions of maximum gradients within the control volume. The average behavior of effective viscosity was tracked as the solution proceeded. It was observed that the turbulence model predicted low values of effective viscosity. The final average effective viscosity was less than five times the laminar value thus a laminar flow was selected. The choice of laminar flow was further justified as the analysis executed without diverging. Alternately a standard k-Є turbulent model was used to study the droplet formation. Using the turbulent model it was observed that the droplet breakup was inconsistent and fluid jet intermittently generated lumps of fluid. This was due to the fact that the additional effective viscosity term dampened out the pressure oscillations within the CV. This artificial dampening was contrary to the drop generation mechanism, which is through acoustic pressure fluctuations.

The control volume chosen for the CFD analysis spans from the PZT disc interface to the nozzle and from the nozzle to the droplet path of flight. The choice of laminar flow is justified for first section (i.e. from the PZT disc to the nozzle) based on the effective viscosity calculations. However the flow of drops through air poses a challenge to the choice of flow regime for the later section of the control volume (i.e. during droplet path of flight). A microdrop is small enough that the force associated with its viscous flow resistance to motion is defined by Stokes Law[84]. The Stokes drag force is different from the more familiar dynamic force associated with macroscopic objects, such as aircraft, in that it is first order independent of air density and is proportional to the first power (not the square) of the speed of the object. Thus the Reynolds number for microdrops can be given in Equation (6.4) [84],

$$Re = vd/\nu \qquad\qquad\qquad (6.4)$$

where,

v is the drop velocity relative to air

d is the drop diameter

ν is the Kinematic viscosity of air (0.151 cm^2/sec at standard temperature and pressure)

For a microdrop with a diameter of 100 μm, the Re is 1.8, which is far below than the turbulent flow regime Re of 10^5[84]. Thus the flow of droplets during path of flight can be modeled with a laminar flow regime. Finally with sufficient contemplation, a laminar flow regime was selected for the entire CFD control volume.

- Time Increments: Automatic time stepping based on the advection limit was used in the analyses. The average time step is on the order of 1/200th of the excitation signal time period.

6.9   CFD MODEL RESULTS

A CFD analysis was performed to determine the drop formation phenomena in a CIJ print head. Before proceeding to a nano particulate solution, analyses were first performed with water for comparison to available experimental results. The input parameter values used for this analysis are tabulated in Table 6 and the fluid properties are listed in Table 7.

Table 6: Input parameter values for CFD analysis

Input Parameter	Value
Fluid Pressure	5psi
Frequency	20kHz
Voltage amplitude	20V

Table 7: Physical properties of water

Property	Notation	Value
Density (kg/m^3)	ρ	1e3
Dynamic Viscosity [kg/(m.s)]	μ	1.14e-3
Surface Tension (kg/m^2)	σ	7.28e-3
Contact angle with walls	θ	90°

A PZT displacement of 0.012μm was obtained from the Multiphysics analysis of the excitation conditions listed in Table 6. This value was impressed as a SHM displacement boundary condition on the top wall of the control volume. The path of flight region of the control volume was restricted to 3mm in length. This length was determined based on the breakup length of the fluid jet at 5psi. Prior experimentation has shown that for a fluid pressure of 5 psi the fluid jet breaks up in the vicinity of 1.5 mm from the orifice. The additional 1.5 mm length was used to capture the drop formation mechanism. The simulation was run for 5 milliseconds and results were appended every time period (0.05 milliseconds) of the excitation cycle.

Figure 44 shows the pressure fluctuations at the breakup length (1.5mm) from the orifice. Zero pressure indicates absence of droplets. The results shown are taken every time period of the frequency cycle. In the CIJ system drops are generated at the excitation frequency, thus in this case every drop is being formed at 0.05 milliseconds. The fluid jet develops for the initial 0.5 milliseconds and hence there is no drop formed at the breakup length. A zero pressure level on the graph indicates this. After the initial 0.5 milliseconds consistent drops are formed at a 20kHz frequency. The droplet generation mechanism occurs with the formation of standing nodes in the fluid jet, which condense into discrete droplets. During breakup the droplet tail snaps off from the fluid jet and merges into the descending drop. This phenomenon involves very high levels of pressure variations and thereby velocity fluctuations in a short period of time (on the order of

micro seconds). The graph shows variations of pressure (peaks) at few cycles. This is because the results are captured at a constant time increment and fluctuations of pressure at that instant may be different for different drops. By selecting a fixed point within the CV (Eulerian approach) the pressure fluctuations of the drop are recorded as it passes through this point.
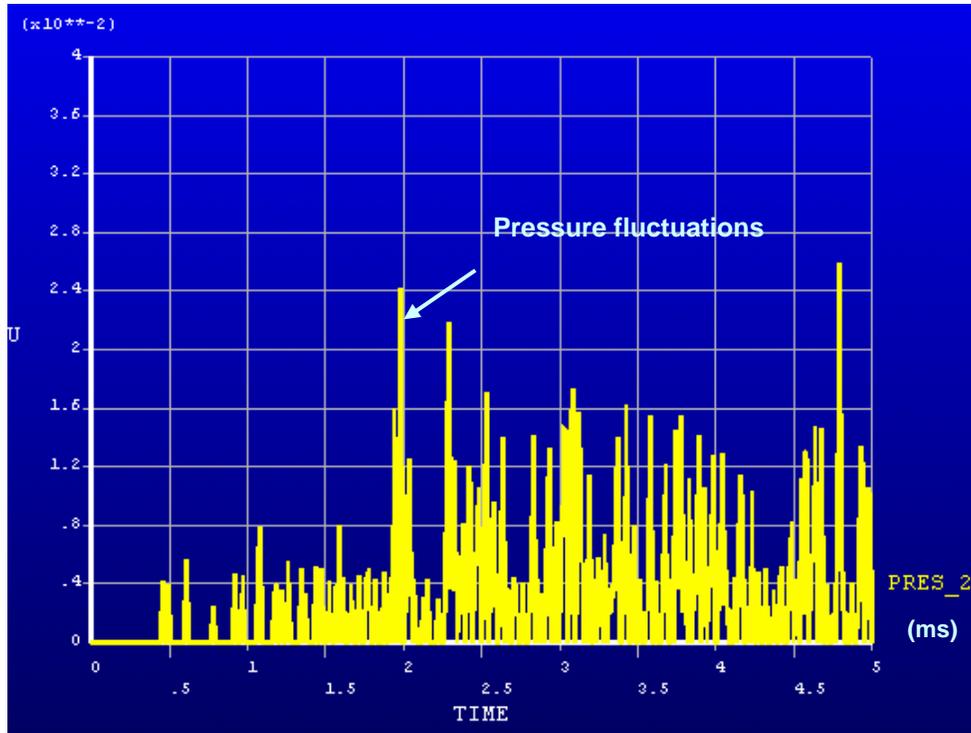
Figure 44: Pressure fluctuations at breakup length (1.5mm) over 5 milliseconds

A detailed view of the pressure fluctuations for the time period between 4 to 5 milliseconds is shown in Figure 45. The spikes of pressure indicate the presence of a drop and the time periods with zero pressure indicates the absence of a drop. From the figure it is evident that the total number of drops formed over a 1 millisecond range is 20. This is equal to the excitation frequency of 20kHz and is a preliminary validation of the CFD model. It is observed that at lower fluid pressures and excitation frequencies there are tendencies to form satellite

droplets, which have varying drop volumes. This is evident from the inconsistent time periods for drop formations.
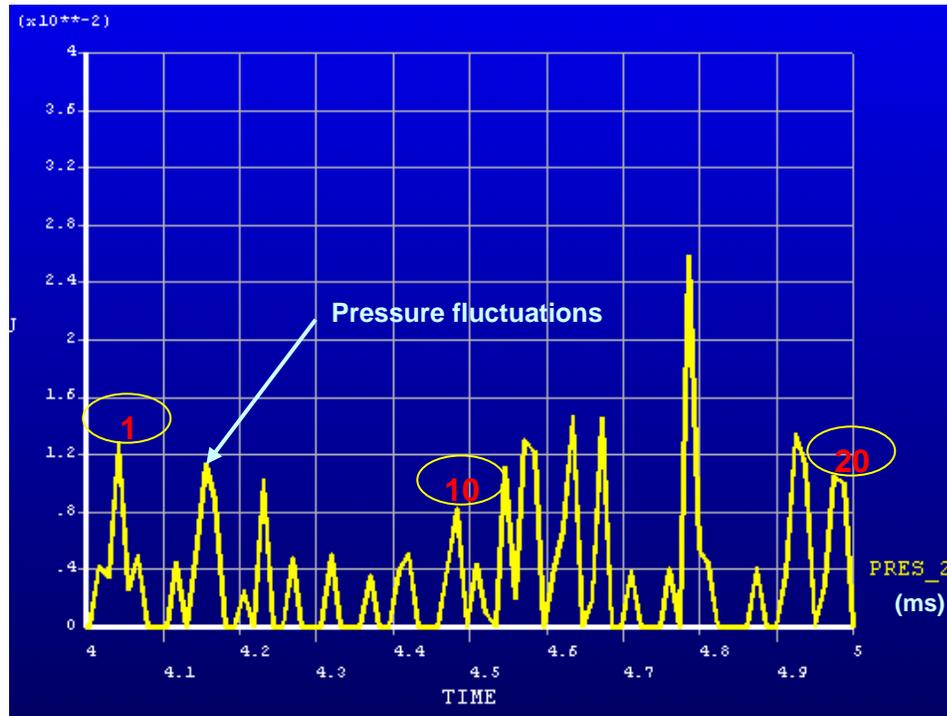
Figure 45: Pressure fluctuations at breakup length from 4 to 5 milliseconds

Figure 46 shows the fluctuations of velocity at the orifice exit over time. The velocity at orifice exit fluctuates around 7.5m/s. These fluctuations in velocity would be absent if fluid was supplied at 5psi without being perturbed by the PZT disc. However these fluctuations indicate the presence of acoustic waves and thereby pressure fluctuations, which lead to drop breakup. The velocity fluctuations shown in Figure 46 appear fairly consistent.
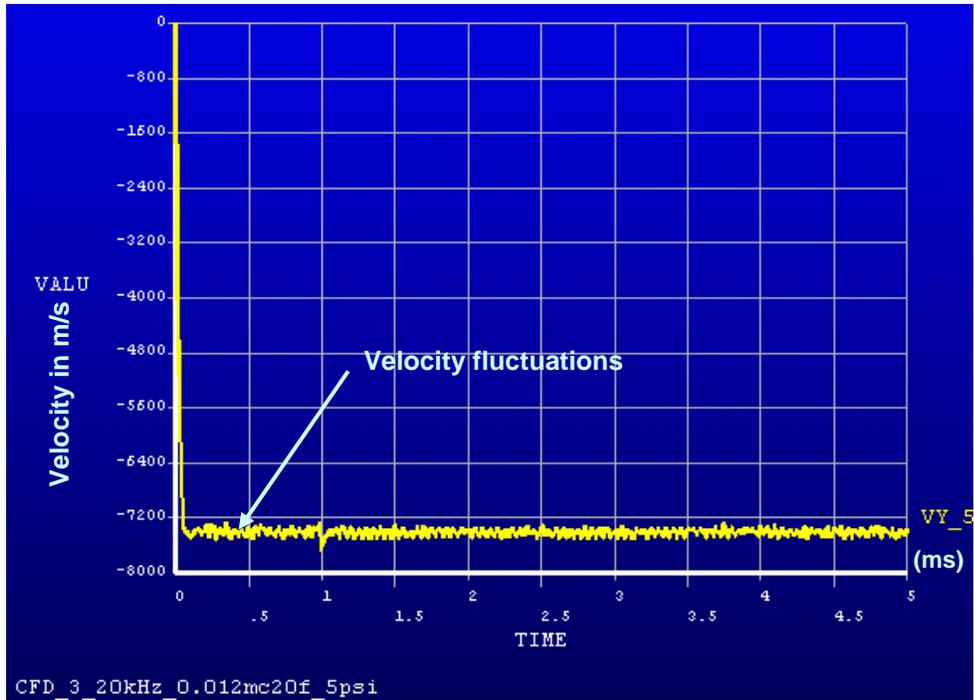
Figure 46: Fluctuations of velocity at the orifice exit over time

Figure 47 shows the fluid jet breakup, satellite formations and droplets at 4 ms. This figure shows the formation of standing nodes within the fluid jet. A tiny satellite drop is formed along with a regular sized drop. The inter-drop distances and drop diameters are fairly consistent. Due to intermittent satellite formations, the droplet volumes are altered causing some drops to appear larger than others.
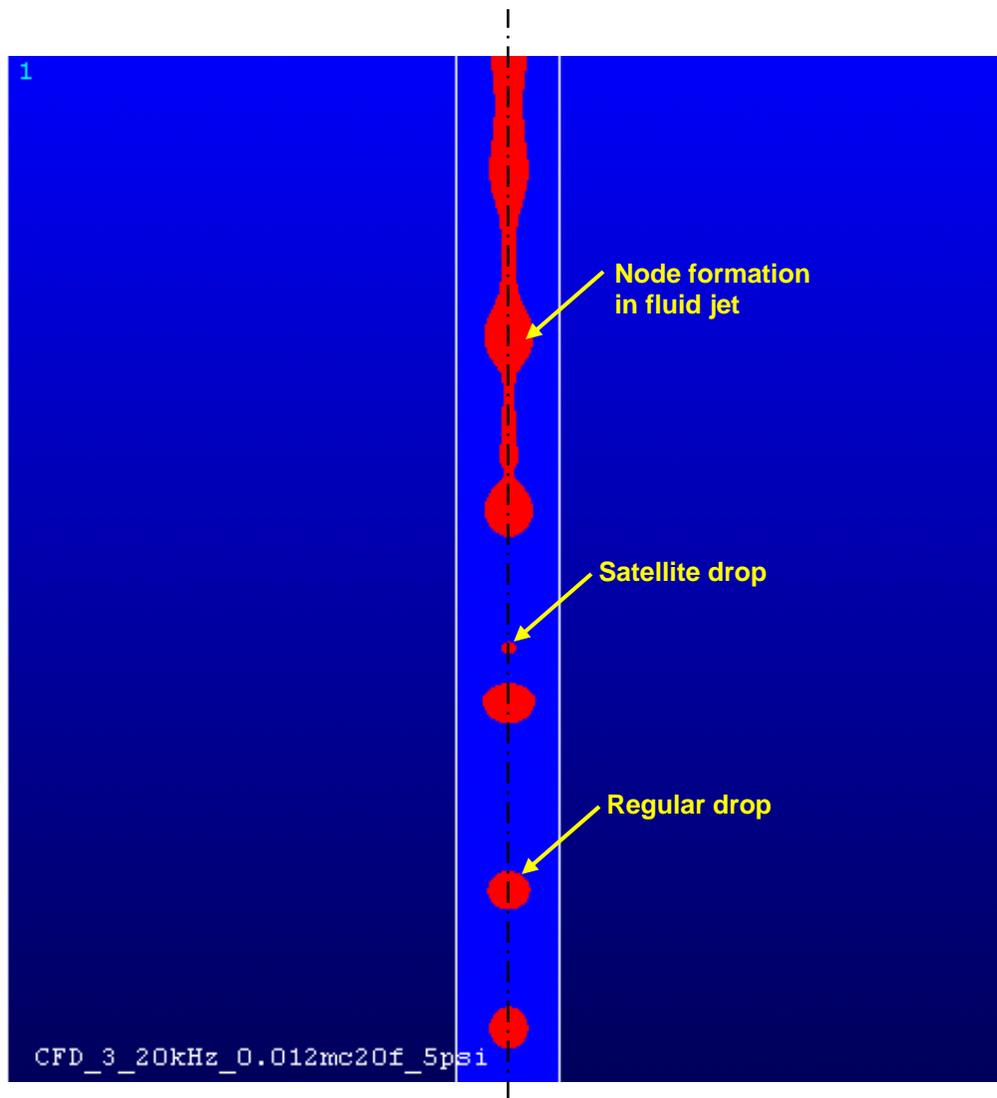
Figure 47: Droplet generation at 4ms

Figure 48 shows the droplet formations at 2.5, 3, 4 and 5 ms respectively. At 2.5ms a fluid ligament is seen merging with the main drop. The fluid jet necking prior to drop snap off is seen at 5ms. These results when combined in a video file give an elegant view of the drop formation mechanism. Similar drop breakup pictures are compared with experimental results from ultra-high speed photography to validate the drop profile, volume and velocity. A close conformance is obtained in each case.
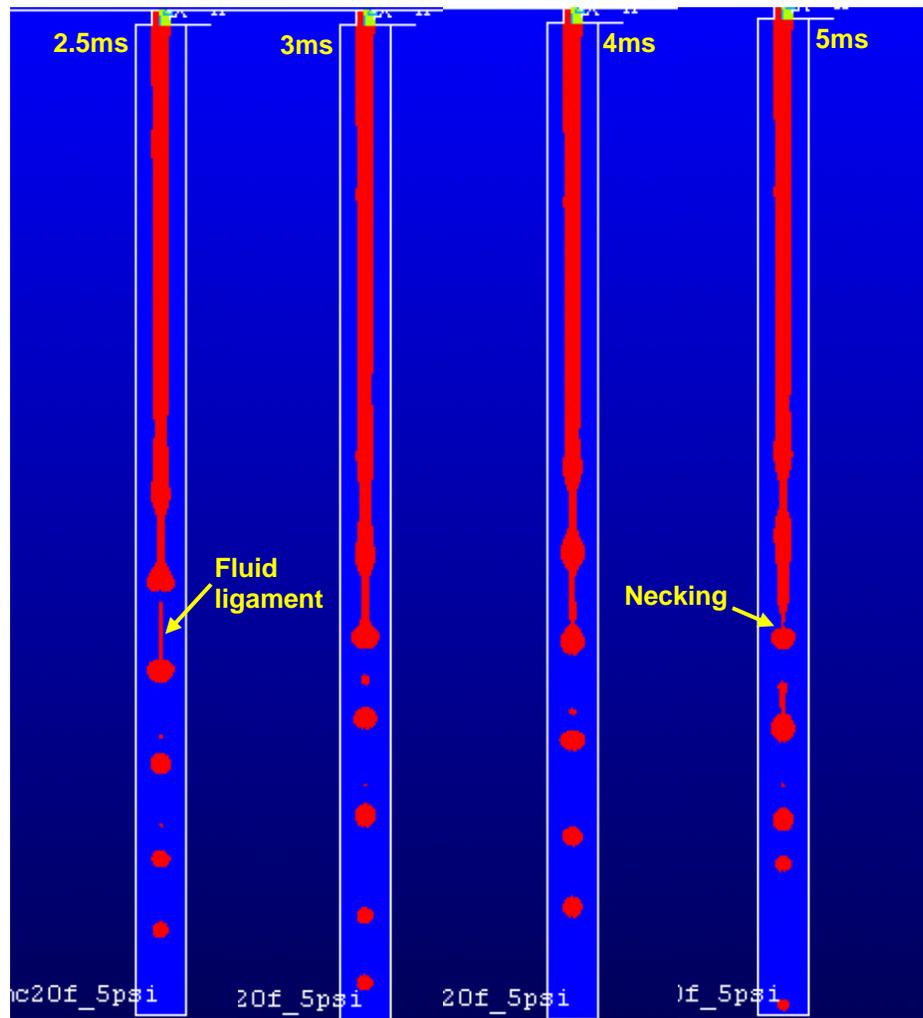
Figure 48: Drop formations at 2.5, 3, 4 and 5 ms

6.10 CFD TRENDS

In a CIJ system, the output response (drop characteristics) is dependent on the supply pressure, PZT excitation, fluid properties & nozzle geometry. One approach for optimizing the drop characteristics is to vary the fluid pressure and PZT excitation parameters. For a given fluid and wall geometry, the input parameters that are practical to vary are:

- Fluid pressure

- Frequency of input signal to the PZT disc

- Amplitude of voltage applied to the PZT disc

  The significant output responses that determine the quality of print are drop:

- Drop Volume

- Drop Velocity

Given the parametric nature of the CFD model outlined in Section 6.9, the model could be directly used to establish the role of pressure and PZT excitation on droplet quality. Each input parameter was varied for 4 levels holding the other parameters constant. Thus the total number of simulations to be executed were 3 input parameters x 4 levels each = 12 runs. However, the use of a different fluid and excitation parameters required double the number of runs for obtaining appropriate droplets. The baseline case (shown in bold in Table 9) was a pressure of 5psi with an excitation frequency and voltage of 20kHz and 90V respectively.

The fluid used for conducting all the CFD trends was a 5nm Hexanethiol Nano gold colloid in Toluene. The fluid had a composition of (0.33gm of nano gold particulate in 2ml toluene) [77]. This nano particulate fluid suspension, when printed, demonstrated low electrical resistance values comparable with ones used for building electronic traces [77]. The physical properties of the fluid are given in Table 8.

Table 8: Physical properties of 5nm gold colloid

Property	Notation	Value
Density (kg/m^3)	ρ	1.05e3
Dynamic Viscosity [kg/(m.s)]	μ	0.79e-3
Surface Tension (kg/m^2)	σ	3.2e-3
Contact angle with walls	θ	90°

6.10.1 Input Parameter: Pressure

Pressure was varied as an input parameter to observe its influence on both the drop volume and velocities. The other input parameters, frequency and voltage were held constant. The values of the input parameters and their corresponding responses (drop volume & drop velocity) are tabulated in Table 9. Pressures were chosen in the range 3-6 psi so as to enable the capturing of drop breakup within the 3mm length of the control volume.

Table 9: Input parameters values and Drop Volume (Pressure varying)

No.	Pressure (psi)	Frequency (Khz)	Amplitude (V)	Drop Volume (picolitres)	Drop Velocity (m/s)
1	3	20	90	124.79	4.56
2	4	20	90	150.53	5.78
3	**5**	**20**	**90**	**195.43**	**6.65**
4	6	20	90	268.08	7.25

Figure 49 shows the plot of Pressure v/s Drop volume. As illustrated in the Figure, the droplet volume increases with fluid pressure in a nonlinear nature. In fact, the drop volume at 6psi is nearly twice that of 3psi. This sharp increase in drop volume can be attributed to the fact that as pressure increases there is an increase in the mass flow rate, which contributes to a higher

drop volume. The variation in droplet volume with increase in pressure can be expressed by the second order equation 6.5.

$$\text{Drop volume (P)} = 193.9 - 58.06*\text{Pressure} + 11.73*\text{Pressure}^2 \qquad (6.5)$$
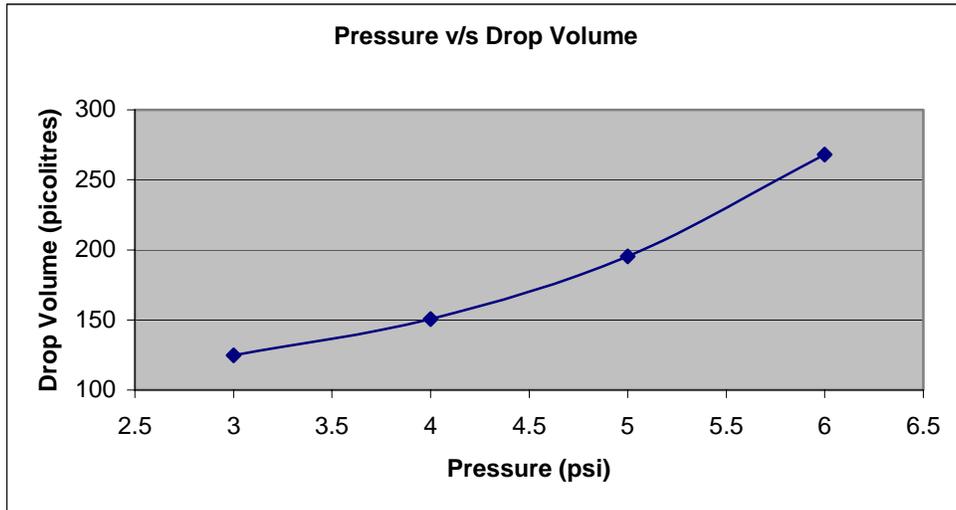
Figure 49: Pressure v/s Drop Volume
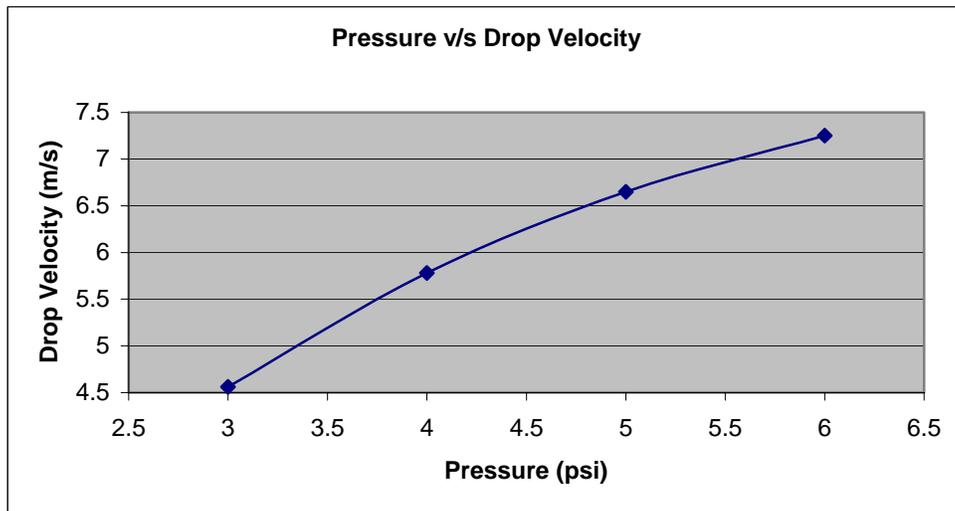
Figure 50: Pressure v/s Drop Velocity

Figure 50 shows the plot of Pressure v/s Drop Velocity. In the figure it is observed that the drop velocity increases as a nonlinear function of the inlet pressure. This can be explained by examining Bernoulli's equation which states that the total pressure at a point within the system remains constant [65].

$$H = p + \frac{\rho v^2}{2} + \rho g z \qquad (6.6)$$

where,

H = Total pressure

p = static pressure

ρ = density of the fluid

v = velocity of the fluid

g = gravitational acceleration

z = potential head

The total pressure is the summation of the static pressure, the dynamic pressure and the potential energy. As the elevation difference between the nozzle droplet breakup height is extremely small, the last term of potential energy is neglected. For a point inside the fluid chamber the static pressure is the dominant part of the total pressure (as velocities are low). However the dynamic pressure, which is proportional to the square of velocity, is the dominant part of the total pressure during droplet path of flight (static pressure is negligible). The balance of the static pressure within the fluid chamber with the dynamic pressure during droplet path of flight therefore results in a nonlinear relationship between inlet pressure and output response (drop velocity). This is expressed by the second order equation 6.7.

$$\text{Drop Velocity (P)} = -0.9080 + 2.289 * \text{Pressure} - 0.1550 * \text{Pressure}^2 \qquad (6.7)$$

6.10.2 Input Parameter: Frequency

In this case, Frequency was varied as an input parameter to observe its influence on both the drop volume and velocities. The other input parameters, pressure and voltage were held constant. The values of the input parameters are their corresponding responses (drop volume & drop velocity) are tabulated in Table 10. The frequency range was chosen within the 20-30 kHz range because frequencies lower than 20kHz did not breakup the fluid stream into droplets.

Table 10: Input parameter values and Drop Volume (Frequency varying)

No.	Pressure (psi)	Frequency (Khz)	Amplitude (V)	Drop Volume (picolitres)	Drop Velocity (m/s)
1	5	20	90	*195.43*	*6.65*
2	5	22.5	90	*150.53*	*6.65*
3	5	25	90	*113.1*	*6.65*
4	5	27.5	90	*96.967*	*6.66*

Figure 51 shows the plot of Frequency v/s Drop volume. In the figure it is found that an increase in frequency from 20kHz exhibits a sharp nonlinear decrease in the drop volume. This is because as input frequency increases the number of drops that are formed from the same quantity of fluid, resulting in lower volume per drop. The relationship between drop volume and frequency of excitation can be expressed by a second order curve given in equation 6.8.

$$\text{Drop Volume (F)} = 1095 - 67.97 * \text{Frequency} + 1.151 * \text{Frequency}^2 \qquad (6.8)$$
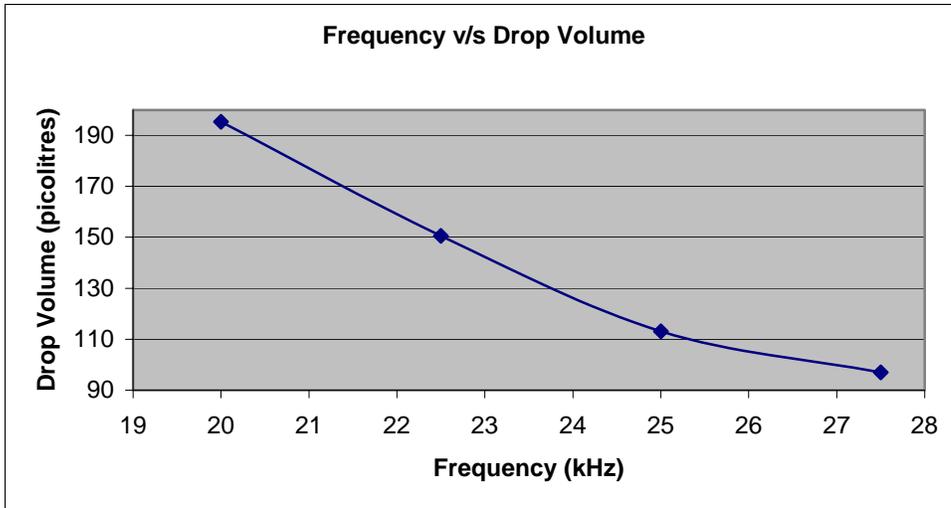
Figure 51: Frequency v/s Drop Volume
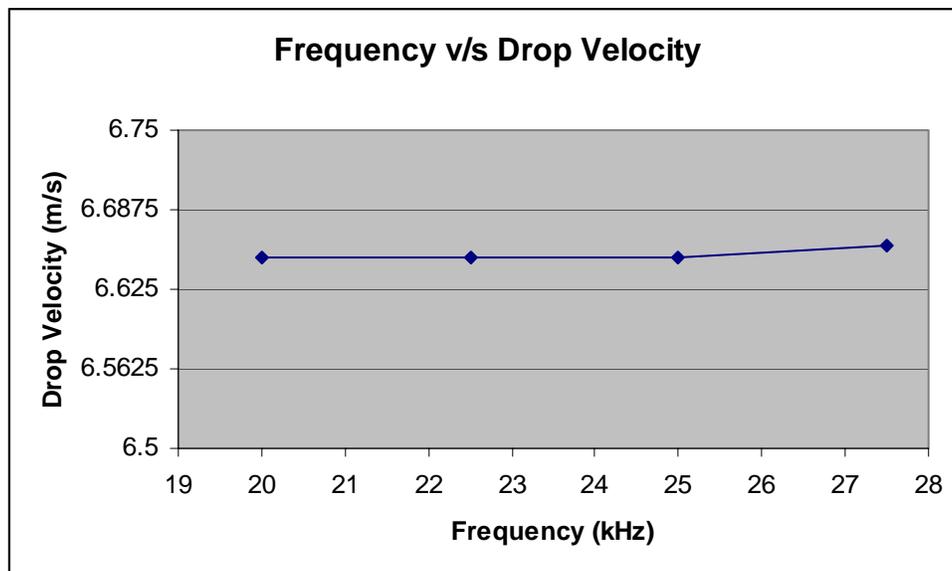
Figure 52: Frequency v/s Drop Velocity

Figure 52 shows the plot of Frequency v/s Drop Velocity. For an increase of frequency from 20kHz to 27.5 kHz the drop velocity does not show any marked changes (remains close to 6.66m/s). This indicates that the frequency of excitation does not alter the drop velocity.

6.10.3 Input Parameter: Voltage

As a final parameter, the Voltage was varied as an input parameter to observe its influence on both the drop volume and velocity. The other input parameters, pressure and frequency were held constant. The values of the input parameters and their corresponding responses (drop volume & drop velocity) are tabulated in Table 11. Voltages were chosen in the 85-100V ranges. This voltage range was chosen because voltages lower than 85V did not result in drop breakup, while voltages higher than 100V caused fluid to breakup intermittently with excessive satellites.

Table 11: Input parameter values and Drop Volume (Voltage varying)

No.	Pressure (psi)	Frequency (Khz)	Amplitude (V)	Drop Volume (picolitres)	Drop Velocity (m/s)
1	5	20	85	*188.99*	*6.66*
2	**5**	**20**	**90**	***195.43***	***6.65***
3	5	20	95	*202.02*	*6.64*
4	5	20	100	*210.46*	*6.64*

Figure 53 shows the plot of Voltage v/s Drop Volume. It can be observed that the drop volume increases with voltage in nearly a linear fashion. This is due to the fact that an increase in input voltage linearly increases the maximum PZT disc displacement and the drop volume is proportional to the PZT displacement. The linear relationship between input voltage and drop volume is expressed by the equation 6.9.

$$\text{Drop Volume (V)} = 67.88 + 1.42 * \text{Voltage} \tag{6.9}$$
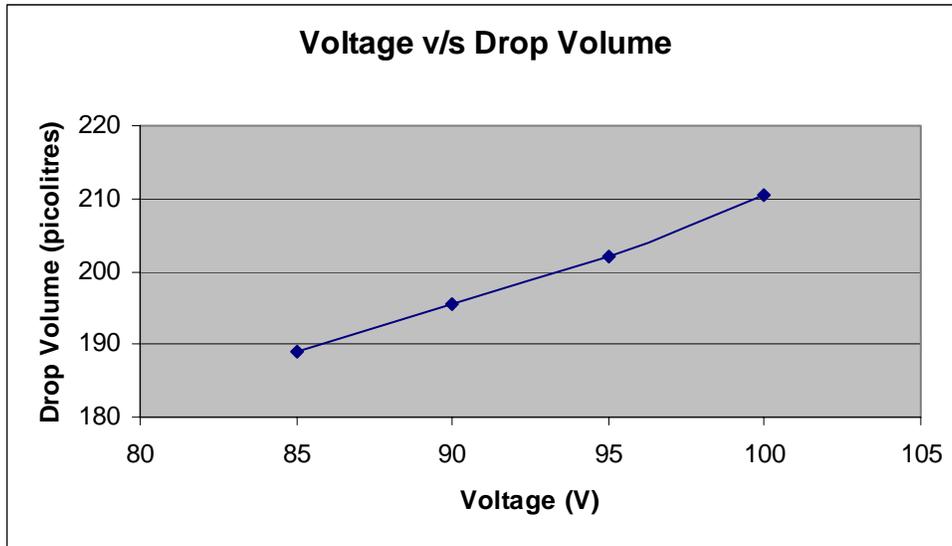
Figure 53: Voltage v/s Drop Volume
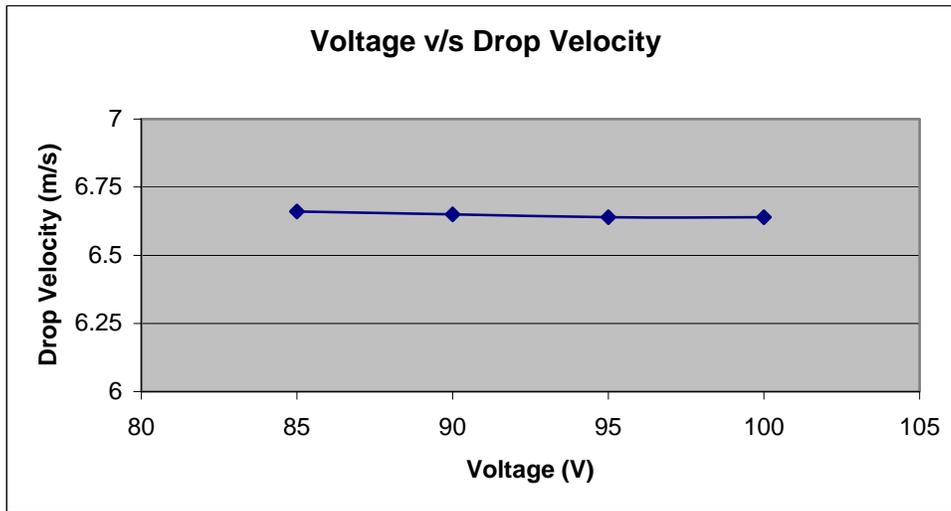
Figure 54: Voltage v/s Drop Velocity

Figure 54 shows the plot of Voltage v/s Drop Velocity. As seen from the figure voltage does not affect the drop velocity. For an increase in voltage from 85 to 100V, the drop velocity stays close to 6.65m/s.

6.11 ILLUSTRATIVE EXAMPLE

The CFD trends developed in this research give insight on the effect of the three input parameters; pressure, frequency, and voltage on the output responses; drop volume and velocity. These trends are valid for the fluids and CIJ printhead parameters studied. Based on the numerical model it has been found that frequencies lower than 17.5kHz do not produce enough excitation to yield drops. Similarly, excitation voltages lower than 85V do not form standing nodes within the fluid stream, which is the mechanism to form droplets. At voltages higher than 100V irregular drops are formed. This is because fluid drops lump together due to excessive amplitude of the standing nodes. Consistent drops with minimal satellites were obtained at a fluid pressure of 5psi with an excitation frequency and voltage of 20kHz and 90V respectively. This research has set a basis so that similar trends can be run for different fluids and excitation conditions without expending valuable resources.

7.0 EXPERIMENTAL DESIGN AND RESPONSE SURFACE OPTIMIZATION

The early chapters of this dissertation focus on the numerical simulation for droplet formation mechanism. It is paramount that the CFD simulations be validated by real-time experimental data. A Design of Experiment approach was used to obtain the significant factors affecting the response of interest. Further, based on the significant factors a Response Surface Optimization was conducted to establish trend patterns for the output response.

Traditionally, researchers have captured droplet results using a CCD camera and synchronizing an LED light source with the drop generation frequency. This method works well to obtain spatial data such as drop volume when drops were formed consistently without satellites around them. However spatio-temporal data such as velocity, drop progression, and satellite formations cannot be captured using stroboscopic methods. It has been observed that satellites were formed at threshold frequencies, which hamper the measurement of drop volume using synchronous photography. A unique method to address these issues is to capture non-superimposing images at ultra-high speeds with extremely short exposure values.

7.1 EXPERIMENTAL SETUP

In order to validate the numerical simulations a custom built CIJ head was fabricated at the Swanson Center [78]. Similarly customized hydraulics [79] and electronic circuitry [80] were

built to control input parameters such as fluid pressure, PZT excitation frequency and voltage to the CIJ print head. The commercially available CIJ print head was incapable of generating input parameters at variable ranges, thus there was a need for a custom built head. The experimental droplet generation rate varied from 10 to 80kHz. In order to capture useful data concerning the flow characteristics of droplet formation, an ultra-high speed camera system was used. For obtaining crisper pictures, the frame capture rates must be at least twice the drop generation frequency. Also, it is necessary that the photographic system provide high-resolution images in the size range of the droplets. To this end, one of the initial stipulations of the system was that it be capable of capturing discernable features as small as 1 micron. In addition, the setup and mounting of the system was flexible enough to allow for the use of interchangeable light sources, print heads and modified configurations of such. Figure 55 shows the experimental setup.

7.1.1 Camera and mounting system

A SENSICAM [81] High-Speed digital camera, capable of capturing high quality images (1280x1024 pixel resolution) at a rate of 10 million frames per second was used for the ultra-high speed photography. The camera has a charged coupled device (CCD), which registers the light on the individual photocells. This data is locally buffered and transmitted to a computer for digital image processing via a coaxial cable.

A configuration of Infinity KC [82] lenses was selected to allow for the appropriate depth of field (DOF) and field of view (FOV) of the droplets. The camera was mounted on a linear slide to adjust the focal length. Figure 55 shows the camera, light source and mounting system.
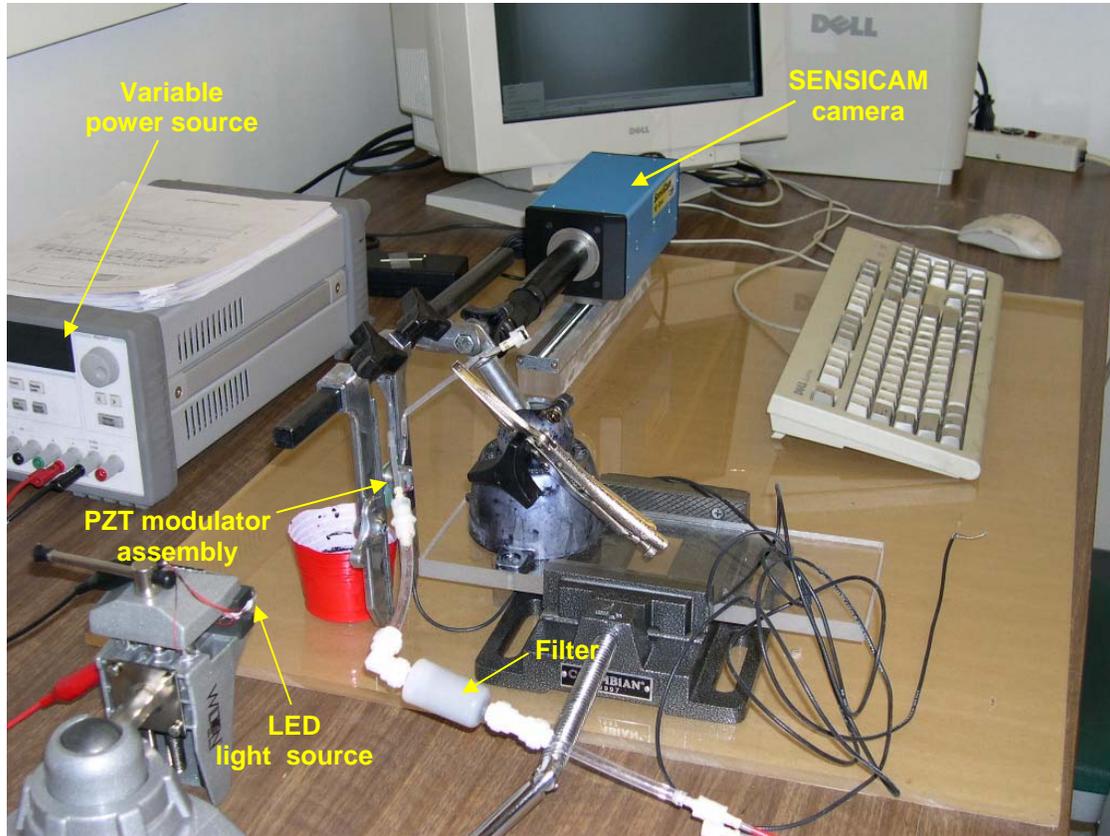
Figure 55: Experimental Setup

7.1.2 Hydraulics

A positive displacement pump was used to supply fluid at pressures up to 100psi. The pump exit line was connected to a high quality filter as contamination of fluids can lead to clogging of the nozzle orifice. A pressure stabilizer was installed in the fluid line to dampen any oscillations from the pump. It was observed that even minimal pressure fluctuations from the pump caused irregular drop breakup.

7.1.3 Illumination setup

The image capture resolution at high speeds was dependent on the quality and intensity of the light source. A backlighting technique was used to capture the droplet formation phenomena.

In this method the light source was placed behind the object of interest to capture its shadow profile. Literature sources [83] have suggested backlighting as one of the best methods to capture microdrops during path of flight. A number of light sources, including high intensity halogen bulbs and diffused fluorescent tubes to LED bulbs were tested experimentation. It was observed that the CCD of the camera was receptive to a well-collimated light source. In many cases the seemingly bright halogen light source could barely be registered on the photocells of the CCD. Thus white LED's were selected to illuminate the background of the drops. The lighting intensity was varied by controlling the input voltage to the LED's. Figure 56 shows the LED's used for the experiments.

Figure 56: LED light source used for the experiments

7.1.4   Piezoelectric Modulator Assembly

Figure 57 shows the PZT modulator assembly, which was custom built at the Swanson Center. It consists of a PZT can, which seats the PZT disc. High-pressure fluid is supplied

through the tubes. Electric leads are connected to the PZT disc for modulation. The nozzle end of the assembly accommodates a 60μm orifice.
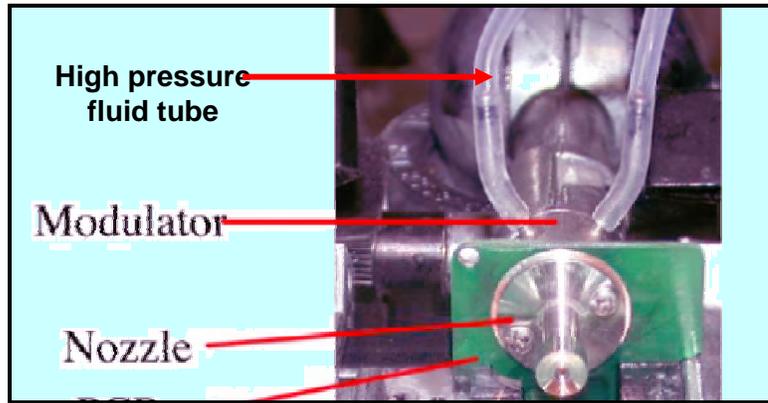
Figure 57: PZT Modulator Assembly

7.2 EXPERIMENTAL RESULTS

The fluid used for experimentation was water. Its physical properties are tabulated in Table 12. A primary reason for choosing water was due to the limited availability and high cost of using nano gold colloid. The droplet volume generated by the CIJ print head is in picoliters. However, due to its continuous drop generation nature the discharge rates become significant, prohibiting the use of an expensive nano gold colloid for experimentation. The CFD simulations in this chapter were also modeled using water so as to compare against the experimental results.

Table 12: Physical properties of water

Property	Notation	Value
Density (kg/m^3)	ρ	1e3
Dynamic Viscosity [kg/(m.s)]	μ	1.14e-3
Surface Tension (kg/m^2)	σ	7.28e-3
Contact angle with walls	θ	90°

7.2.1 Variations in Breakup length

The breakup length of the fluid jet was primarily based on the fluid pressure. A high-pressure fluid jet will be ejected at higher velocities from the nozzle orifice thus breaking up at larger lengths from the orifice exit. It was essential to investigate the breakup length of the fluid jet as it determines the location of the charge tunnel within the print head. The charge tunnel (discussed in section 3.2) should be ideally located such that it impresses a charge on the fluid stream at the breakup point. Thus the breaking droplets carry a charge with them during flight. Improper placement of the charge tunnel can lead to intermittent drop charging or a failure to impress any charge on the droplets. The breakup lengths at pressures 5, 10, 20 and 40 psi were recorded at a frequency of 20kHz and voltage amplitudes of 20V AC. Figure 58 shows the variations in breakup lengths for different excitation parameters.
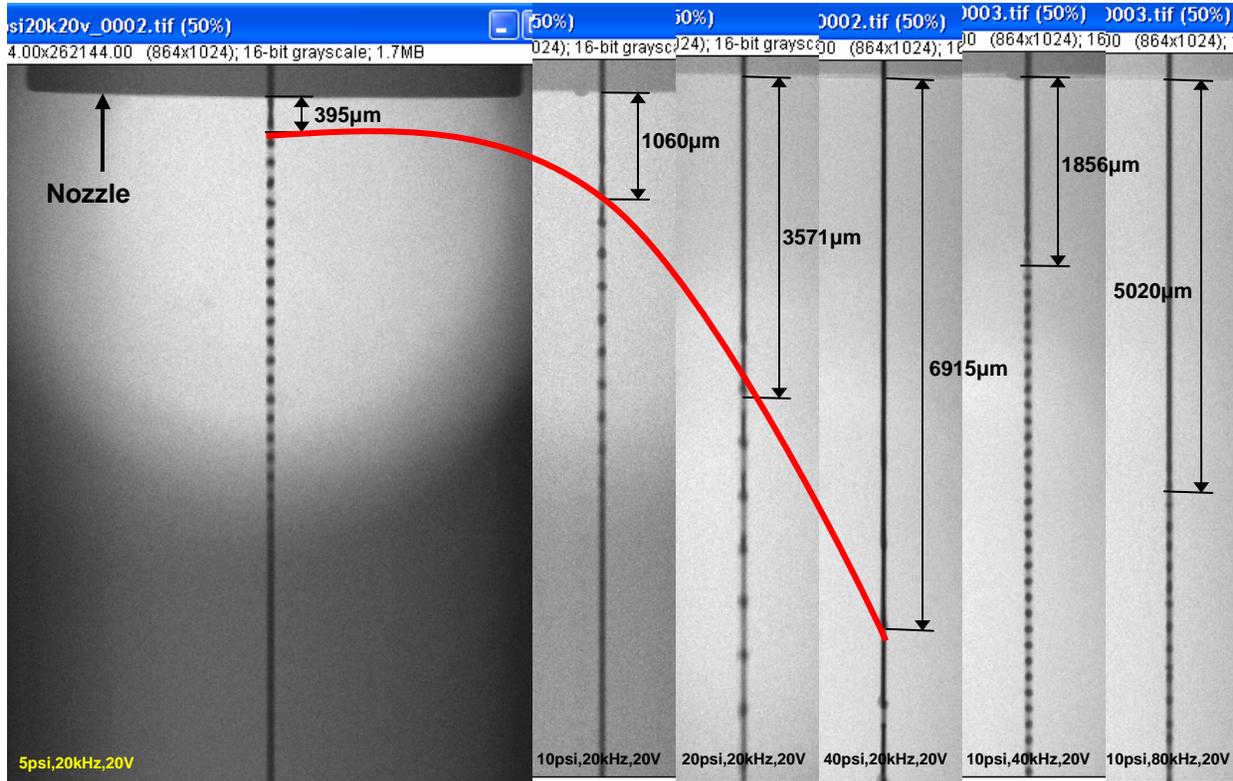
Figure 58: Variations in droplet breakup lengths

As seen from Figure 58 the drop breakup length is a function of the pressure. The breakup length increases at higher pressures and can be defined as a non-linear function of pressure. The nozzle diameter shown in the Figure 58 gives an estimate of the dimension scale for measurements. The fluid jet diameter can also be used as a reference for the length scale. In the CIJ system the fluid jet exits the nozzle at a diameter equal to the orifice diameter. In this case the orifice diameter is 60μm, thus the fluid jet diameter is identical for all cases. The measurements for the breakup lengths were done using an Image Processing and Analysis software in Java called (ImageJ) [84] provided by the National Institute of Health (NIH). The image analysis software allows the establishing of a reference scale at the outlet. Once the scale is calibrated, point-to-point linear dimensions can be measured accurately based on the density of

pixels in the picture file. The photos captured by the SENSICAM camera are high-resolution pictures (1280X1024) per frame. The image contrast is adjusted to obtain crisper images.

Table 13 shows the relation of droplet breakup length with excitation parameters. Given that frequency and voltage remain constant, the breakup length is dependent on the fluid pressure. However at constant pressure and amplitude, breakup length is a function of the frequency of PZT signal. The breakup length increases as a nonlinear function of the excitation frequency. Thus pressure and frequency are important parameters that determine the breakup length of the fluid jet.

Table 13: Relation of droplet breakup length with excitation parameters

No.	Pressure (psi)	Frequency (Khz)	Amplitude (V)	Break up Length (μm)
1	5	20	20	*395*
2	10	20	20	*1060*
3	20	20	20	*3571*
4	40	20	20	*6915*
5	10	40	20	*1856*
6	10	80	20	*5020*

7.3   CFD MODEL VALIDATION

7.3.1   Droplet Profile and Volume Comparison

The CIJ printer generates drops at rates equal to the excitation frequency of input signal. It is desired that the droplets are consistent in the volume over time. There can, however, be satellite drop formations depending on the fluid properties and excitation parameters. Droplet volumes are calculated and compared for experimental and CFD results. Figure 59 shows the comparison of droplet profiles and volumes. Both of the images were evaluated with ImageJ software. The length scale is calibrated as explained in the breakup length procedure. A copper wire of diameter 241.3μm is inserted into the frame view during experimentation to establish a reference length scale. The control volume diameter of 160μm was selected as reference length for the CFD model. The input excitation parameters in the experimental and CFD cases were Pressure = 5psi, Frequency = 10kHz and Voltage = 60V. It was observed that at lower frequency and pressure there was a tendency towards satellite formations. This is captured both in real-time photographic images and CFD simulations.

The following assumptions were made to calculate the volume of the droplets:

The ink droplet was assumed to be an ellipsoid [85], which can be defined in Cartesian coordinates as given in equation (7.1).

$$\frac{x^2}{a^2} + \frac{y^2}{b^2} + \frac{z^2}{c^2} = 1 \qquad (7.1)$$

The volume of ellipsoid is given in equation (7.2).

$$\text{Ellipsoid Volume} = \frac{4}{3} \times \pi \times a \times b \times c \qquad (7.2)$$

where, a, b, and c, are the radii in the x, y, and z axes, respectively.

The only force on the drop was due to the breakup phenomena wherein the perturbation force exceeds the surface tension of the fluid. The drop continues to oscillate in the mutually perpendicular X & Y direction (in the plane of the photograph) to stabilize into a sphere. There exists no force or disturbance due to air currents in the third dimension Z (out of plane direction). Thus ideally the drop varies its radii (a & b) in the X & Y dimension. The Z dimension radius (c) varies equal to the Y dimension radius (b).
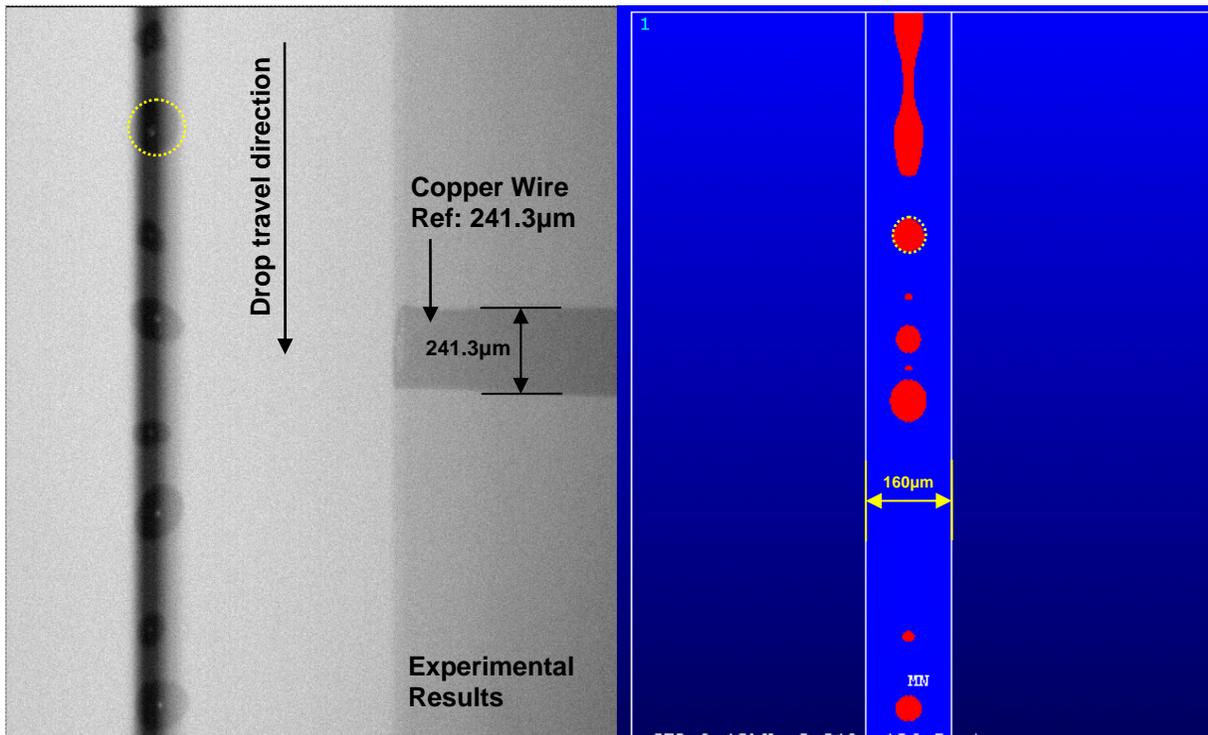
Figure 59: Droplet Profile and Volume Comparison

The drop volumes were calculated using equation (7.2) and a hypothesis testing based on two-sample T test [86] was conducted to compare the droplet volumes. Data from both experimental and CFD results were assumed to have a normal distribution. A T-test was chosen as population means and variances were unknown and sample size was 10. The null hypothesis for a two-tailed two-sample T test was,

H_0: $\mu_1 - \mu_2 = \delta_o$ versus the alternate hypothesis,

H_1: $\mu_1 - \mu_2 \neq \delta_o$

Where, μ_1 and μ_2 are the population means of the experimental and CFD drop volumes respectively and δ_o is the hypothesized difference between the two population means. In other words, the alternate hypothesis determines if the population means differ significantly. The mean and standard deviation of the two samples are tabulated in Table 14.

Table 14: Mean and Standard deviation of Droplet Volume

Result Type	Number of runs	Mean (picoliters)	StDev.
EXP	10	1004.2	65.3
CFD	10	966.3	66.5

Difference = $\mu_1 - \mu_2$

Estimate for difference: 37.8659

95% CI for difference: (-24.3285, 100.0603)

T-Value = 1.28, P-Value = 0.216, Degree of Freedom = 17

The 95% confidence interval for difference in population means is (-24.3285, 100.0603) which includes zero, thus suggesting that there is no difference between the means. The test statistic is 1.28, with a p-value of 0.219. Since the T value is less than the $T_{critical} = 2.11$ and the p-value is greater than 0.05, there is no statistical evidence for a difference in drop volumes obtained from experimental and CFD results. Thus the null hypothesis H_0 is accepted in favor of the alternate hypothesis H_1 to conclude that the droplet volumes in the experimental and CFD results show close conformance with each other.

7.3.2 Droplet Velocity comparison

It has been shown that the droplet volume and profile from CFD simulations match closely with the real-time experimental results. However this conformance relates only to the spatial aspect of validation. A rigorous treatment is applied to the CFD model by comparing the droplet velocity during droplet path of flight. Figure 60 shows the calculation and comparison of the droplet velocities during the early stages of the path of flight.
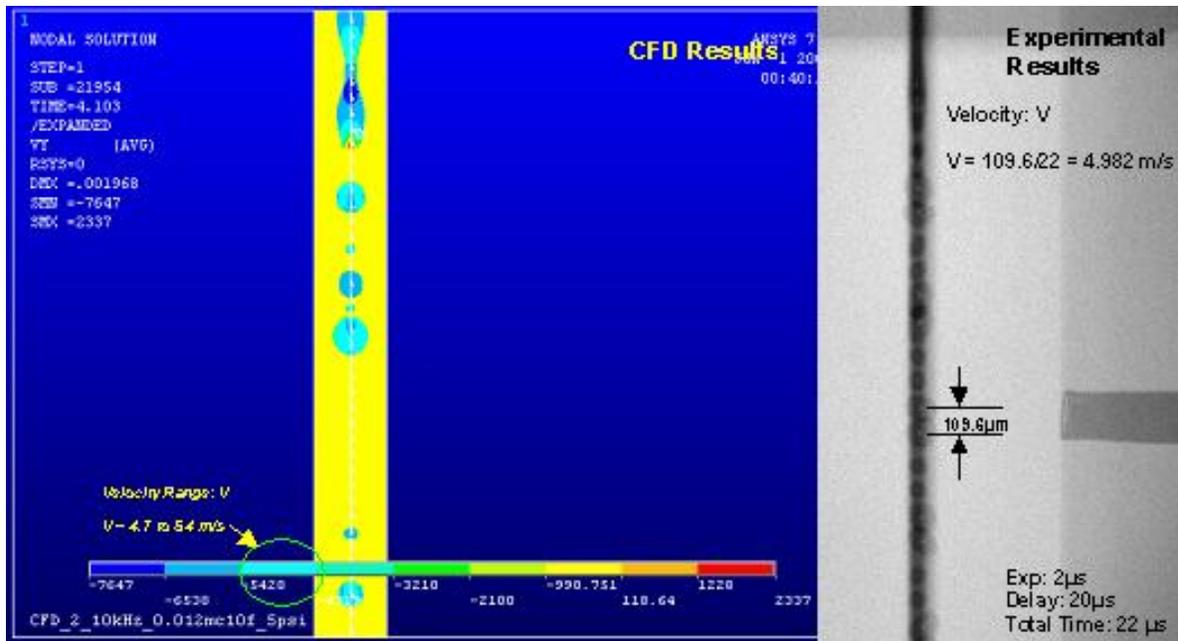
Figure 60: Droplet Velocity Comparison

For the experimental results a double exposure is captured per frame. The total time the drop travels is equal to the (exposure + delay) times. In this case the exposure time is 2μs and the delay time is 20μs. The delay is intentionally prolonged to capture the same drop after 109.6μm travel and prevent superimposition of the droplets on each other. The velocity was calculated

from basic principles of physics. The droplet velocity in the experimental case is 4.982m/s. The droplet velocity in the CFD results varies on the location of the nodes within the drop. On an average the number of nodes per drop is around 250. A significant number of these nodes have droplet velocities in the range 4.7 – 5.4 m/s. The droplet velocity at the center of the drop is 5.04m/s. There exists a deviation of velocities for individual nodes because the droplet oscillates to attain a spherical shape and thereby the individual nodes have velocities changing both in direction and magnitude.

The drop velocities were calculated using the above procedure and a hypothesis test based on two-sample T test [87] was conducted to compare the droplet velocities. Data from both experimental and CFD results were assumed to have a normal distribution. A T-test was chosen as population means and variances were unknown and sample size was 10. The null hypothesis for a two-tailed two-sample T test was,

$H_0: \mu_1 - \mu_2 = \delta_o$ versus the alternate hypothesis,

$H_1: \mu_1 - \mu_2 \neq \delta_o$

Where, μ_1 and μ_2 are the population means of the experimental and CFD drop velocities respectively and δ_o is the hypothesized difference between the two population means. In other words, the alternate hypothesis determines if the population means differ significantly. The mean and standard deviation of the two samples are tabulated in Table 15.

Table 15: Mean and standard deviation of Droplet Velocity

Result Type	Number of runs	Mean (picoliters)	StDev.
EXP	10	5.0859	0.0955
CFD	10	5.112	0.109

Difference $= \mu_1 - \mu_2$

Estimate for difference: -0.026177

95% CI for difference: (-0.122967,0.0706)

T-Value = -0.57, P-Value = 0.576, Degree of Freedom = 17

The 95% confidence interval for difference in population means is (-0.122967,0.0706) which includes zero, thus suggesting that there is no difference between the means. The test statistic is T = –0.57, with a p-value of 0.576. Since the T value does not lie beyond the $T_{critical}$ regions of the distribution curve (i.e.-2.11< -0.57 < 2.11) and the p-value is greater than 0.05, there is no statistical evidence for a difference in drop velocities obtained from experimental and CFD results. Thus the null hypothesis H_0 is accepted in favor of the alternate hypothesis H_1 to conclude that the droplet velocities in the experimental and CFD results show close conformance with each other.

From the droplet volume and velocity comparisons it can be concluded that the CFD results are reliable predictors of droplet characteristics. Thus the parametric CFD model can be judiciously utilized to predict the behavior of fluid jets and resultant droplets.

7.4   FACTORIAL DESIGN FOR DROPLET VOLUME

One of the critical aspects of optimal print quality for CIJ printing technology is the droplet volume. Thus it is important to determine which input parameters affect the droplet volume. Based on the results of CFD models and preliminary experimental data it was observed that 3 factors namely; Pressure, Frequency and Voltage affect the droplet volume. However a superficial observance of such trends does not constitute a scientific understanding of the droplet

volume. A valid approach to this problem is to run a designed experiment whereby we can statistically conclude our hypothesis. In the current research a 2^3 full factorial design is utilized to study the joint effect of the three factors namely; Pressure, Frequency, and Voltage amplitude on the droplet volume. This is a typical factor screening experiment to determine which of the factors have an influence on the droplet volume. The details of the 2^k (where k=3) [88] design is shown in Table 16. As the design is a full factorial design, all the terms are free from aliasing effects and thus we can check for three way interaction effects.

Table 16: Full Factorial Design

Designation	Value
Factors	3
Base Design	3,8
Replicates	2
Runs	16
Blocks	1

The design with eight treatment combinations is displayed as a cube as shown in Figure 61. The low and high levels of each factor are given in parenthesis i.e.; Pressure in psi (10, 20), Frequency in kHz (15, 30) and Voltage amplitude in volts (10, 35). The response (Droplet Volume) is measured in picolitres.
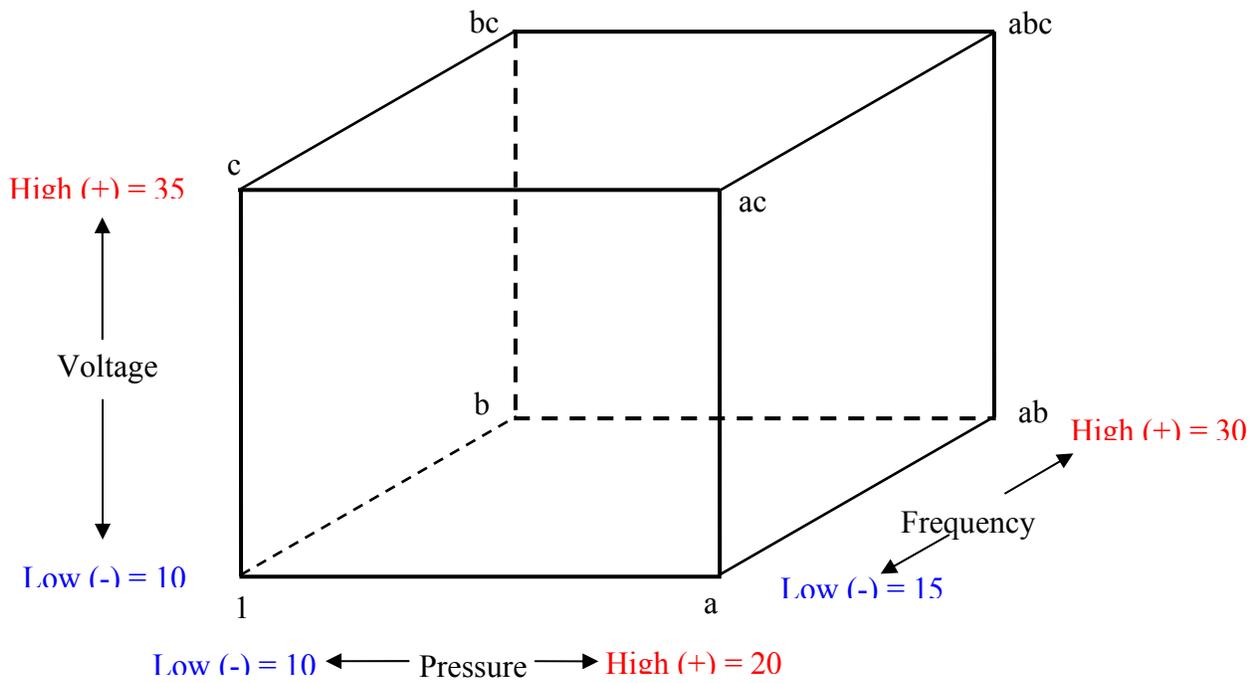
Figure 61: Geometric view of 2^3 factorial design

Table 17: Factorial Design Matrix

No.	Pressure (psi)	Frequency (kHz)	Voltage (V)
1	20	15	10
2	20	15	35
3	20	30	10
4	10	30	10
5	10	15	10
6	20	30	35
7	10	30	10
8	10	30	35
9	20	15	35
10	20	30	35
11	10	15	35
12	10	15	10
13	20	30	10
14	20	15	10
15	10	30	35
16	10	15	35

Table 17 displays the design matrix at low and high levels of the factors in a randomized order.

7.4.1 ANOVA Results

An Analysis of Variance was conducted to determine the significant factors affecting the droplet volume. Table 18 shows the estimated effects and coefficients for Drop Volume in coded units based on an alpha level of 0.05. The R-Sq(adj) value is 99.13% which indicates a well fitted regression model. The R-square statistic represents the proportion of total variation in droplet volume as explained by the regression of droplet volume on the independent variables.

Table 18: Factorial Fit and ANOVA for Drop Volume

Term	Effect	Coef	SE Coef	T	P
Constant		1671.2	22.13	75.52	0.000
Pressure	983.8	491.9	22.13	*22.23*	*0.000*
Frequency	-1383.3	-691.7	22.13	*-31.26*	*0.000*
Voltage	197.1	98.5	22.13	4.45	0.002
Pressure*Frequency	-581.0	-290.5	22.13	*-13.13*	*0.000*
Pressure*Voltage	88.7	44.3	22.13	2.00	0.080
Frequency*Voltage	-66.3	-33.1	22.13	-1.50	0.173
Pressure*Frequency*Voltage	-293.0	-146.5	22.13	-6.62	0.002

Based on a P value of 0.001 and higher T values the significant factors are Pressure and Frequency. Also the two-way interaction between Pressure and Frequency are observed to play a role in the droplet volume. Figure 62 shows the Normal Probability plot of the standardized effects. The significant effects are A: Pressure, B: Frequency, and AB (Pressure-Frequency interaction).
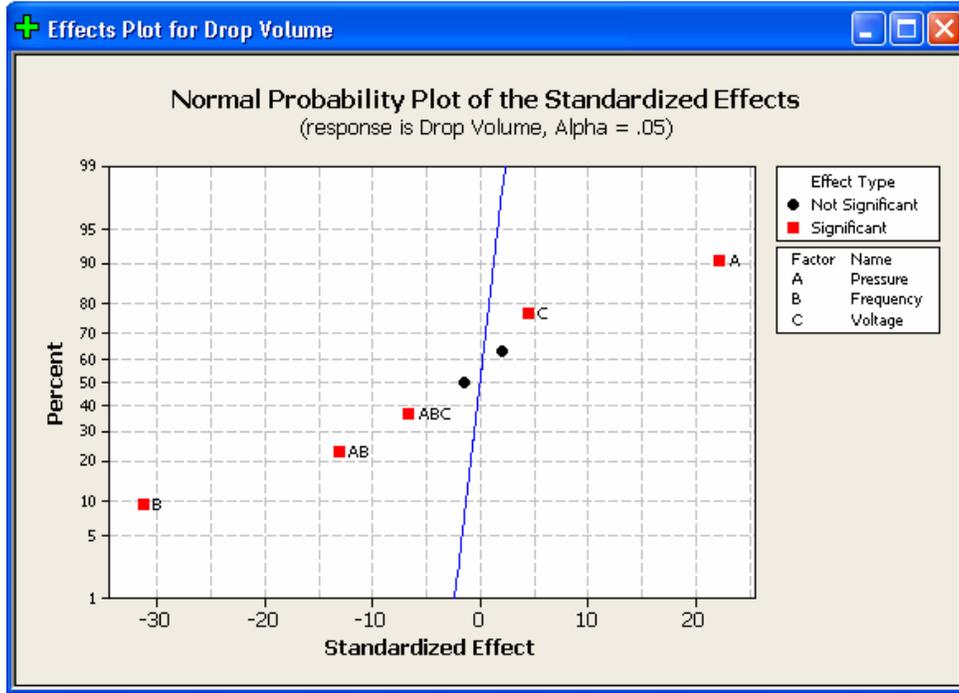
Figure 62: Normality Plot of the standardized effects
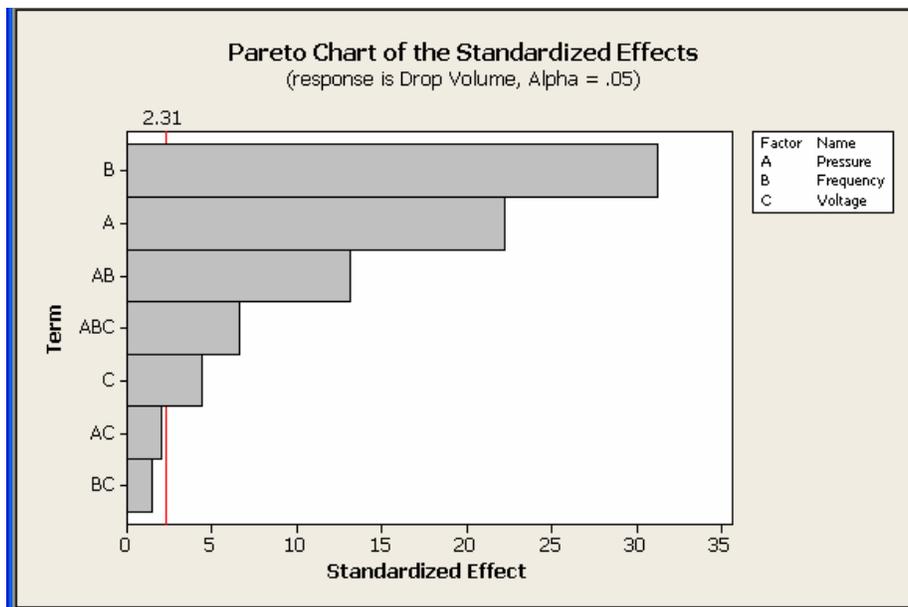
Figure 63: Pareto Chart of the standardized effects

Similarly, the Pareto chart shown in Figure 63 shows that Pressure, Frequency and their interaction significantly affect the droplet volume.
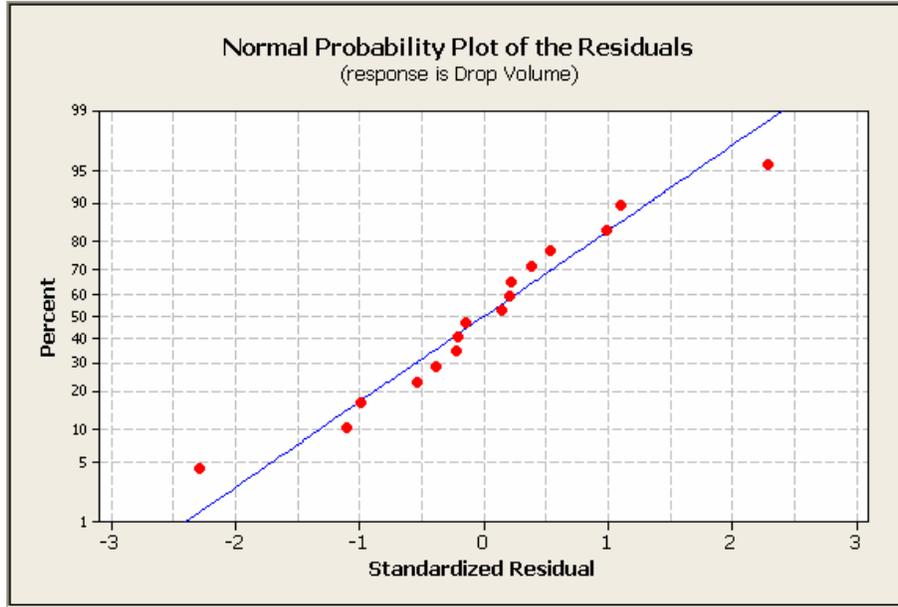
Figure 64: Normal Probability plot of the residuals
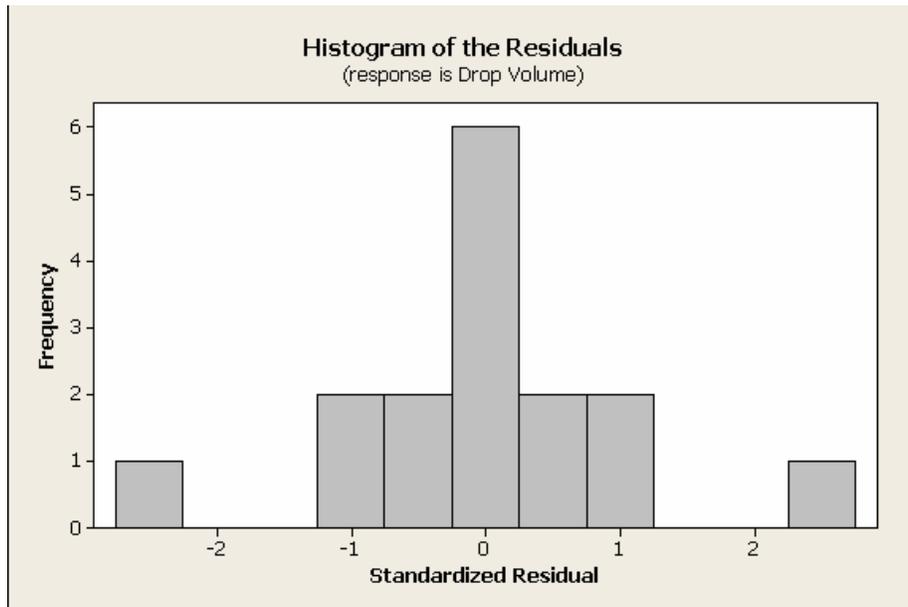
Figure 65: Normal Probability plot of the residuals

As seen from Figures 64 and 65 the normality assumption is justified. The plot of residuals against the order of data shown in Figure 66 validates the random sequence of experimental runs.
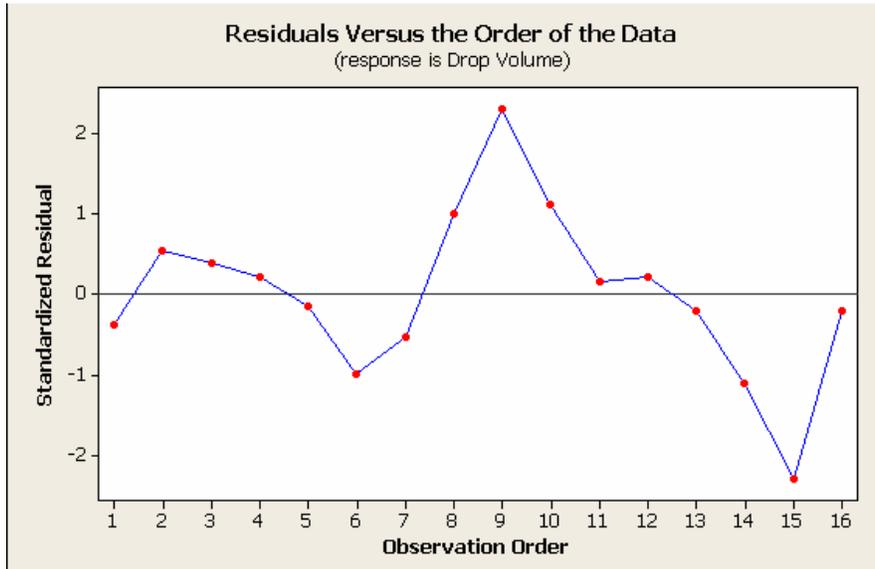
Figure 66: Residuals versus the order of the data

The above experimental design indicates that the Pressure and the Frequency are the significant factors that determine the droplet volume (Response). The next step is to investigate their role on the droplet volume with a Response Surface Design.

7.5   FACTORIAL DESIGN FOR DROPLET VELOCITY

Before proceeding on to the response surface design, a factorial design for Droplet Velocity is evaluated. The factorial design matrix, factor levels and run sequence are identical to the droplet volume design with the exception of the response, which in this case is the Droplet

Velocity. Table 19 shows the ANOVA results for Droplet Velocity in coded units based on an alpha level of 0.05. Based on a P value of 0.001 and higher T value, pressure was the only significant factor among all three factors that affected the Droplet Velocity. The R-Sq(adj) value is 99.66% which indicates a well fitted regression model. R square statistic represents the proportion of total variation in droplet velocity as explained by the regression of droplet velocity on the independent variables.

Table 19: Factorial Fit and ANOVA for Droplet Velocity

Term	Effect	Coef	SE Coef	T	P
Constant		14.2164	0.05384	264.03	0.000
Pressure	7.0847	3.5424	0.05384	*65.79*	*0.000*
Frequency	0.4803	0.2401	0.05384	4.46	0.002
Voltage	-0.0410	-0.0205	0.05384	-0.38	0.713
Pressure*Frequency	0.4721	0.2361	0.05384	4.38	0.002
Pressure*Voltage	-0.4888	-0.2444	0.05384	-4.54	0.002
Frequency*Voltage	0.0480	0.0240	0.05384	0.45	0.668
Pressure*Frequency*Voltage	-0.1807	-0.0904	0.05384	-1.68	0.132
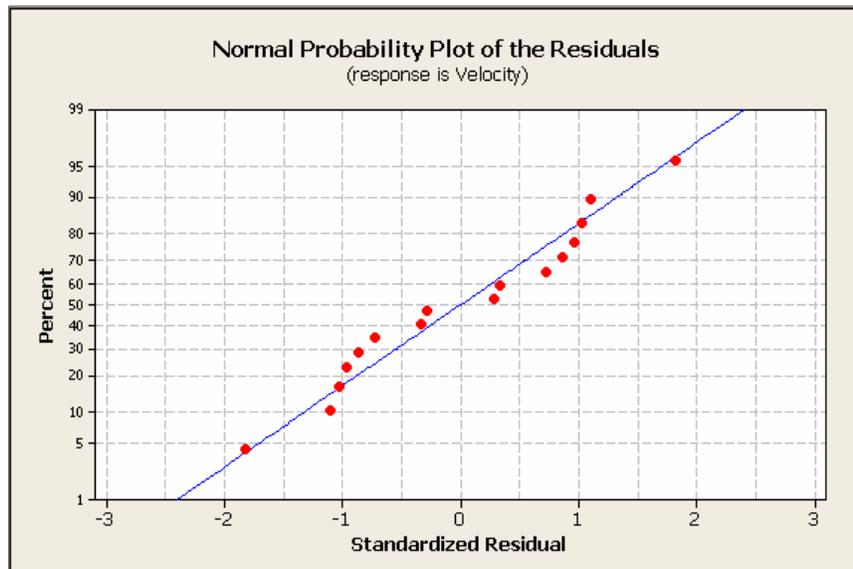
Figure 67: Normal Probability plot of the residuals

Figure 67 shows that the response values have a normal distribution. Figure 68 shows the Pareto Chart of the standardized effects. Fluid pressure within the chamber is the only significant factor affecting the droplet velocity.
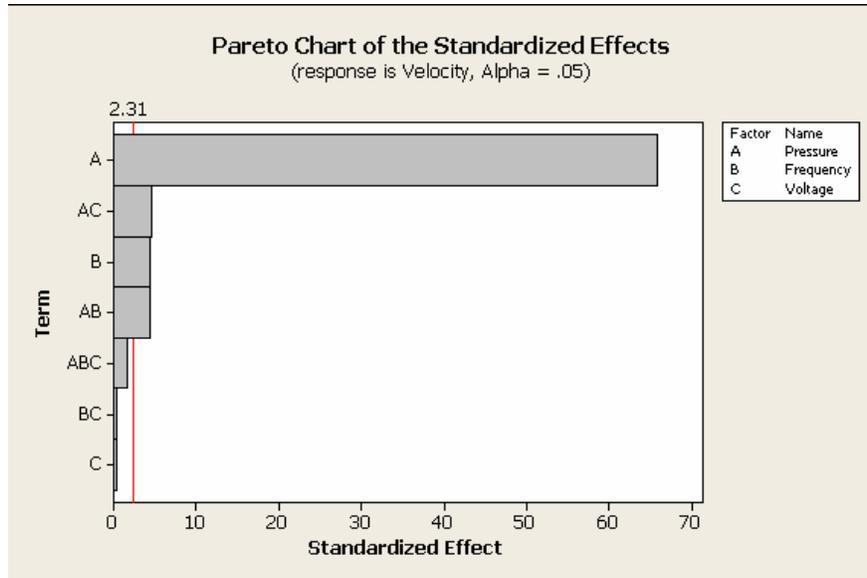
Figure 68: Pareto Chart of the standardized effects

7.6   RESPONSE SURFACE OPTIMIZATION

The factor screening experiment conducted earlier concludes that Pressure and Frequency are the significant factors affecting Droplet Volume. In order to investigate this claim further and establish the trend patterns for Droplet Volume a Response Surface design was employed. A face centered Central Composite Design (CCD) is utilized for fitting a second-order model to the response surface [89]. Table 20 gives the details of the CCD design with two factors.

Table 20: Central Composite Design

Designation	Value
Factors	2
Base Runs	13
Replicates	1
Total Runs	13
Blocks	1
Center axial points	4
Center points	5
Axial points	4
Alpha	1

A geometric view of the design is displayed as shown in Figure 69. The lower, axial and higher levels of each factor are given in parenthesis i.e.; Pressure in psi (20, 30, and 40) and Frequency in kHz (20, 40, and 60).
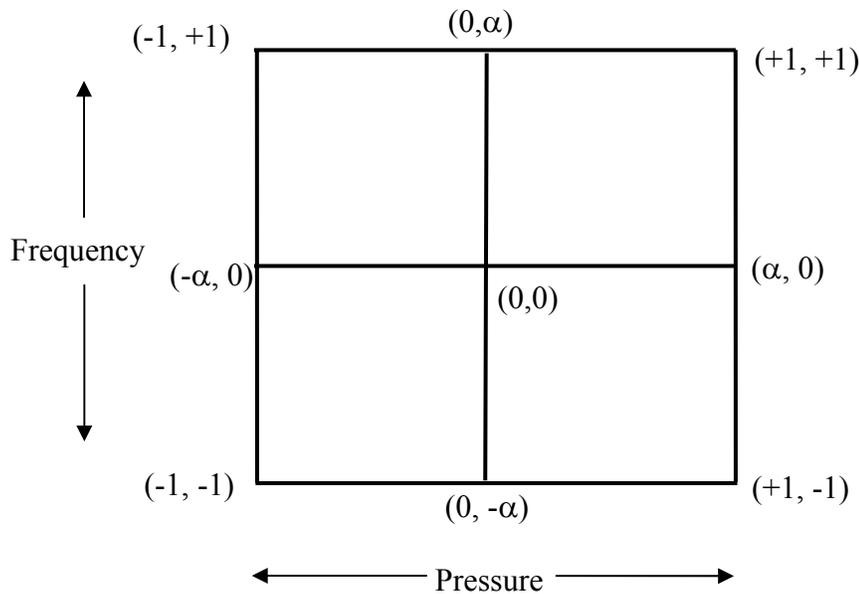
Figure 69: Central Composite Design for Droplet Volume in coded units

Table 21: CCD Design Matrix

No.	Pressure (psi)	Frequency (kHz)
1	40	20
2	30	60
3	40	60
4	30	20
5	30	40
6	40	40
7	20	60
8	30	40
9	30	40
10	20	20
11	30	40
12	30	40
13	20	40

Table 21 displays the design matrix for CCD at lower, axial and higher levels of the factors in a randomized order. The choice of $\alpha = 1$, is because the region of interest is a square.

7.7   SURFACE AND CONTOUR PLOTS FOR DROPLET VOLUME

An ANOVA was conducted to determine the influence of linear and quadratic regression terms on the droplet volume. Figure 70 shows that the response distribution has a valid normal distribution.
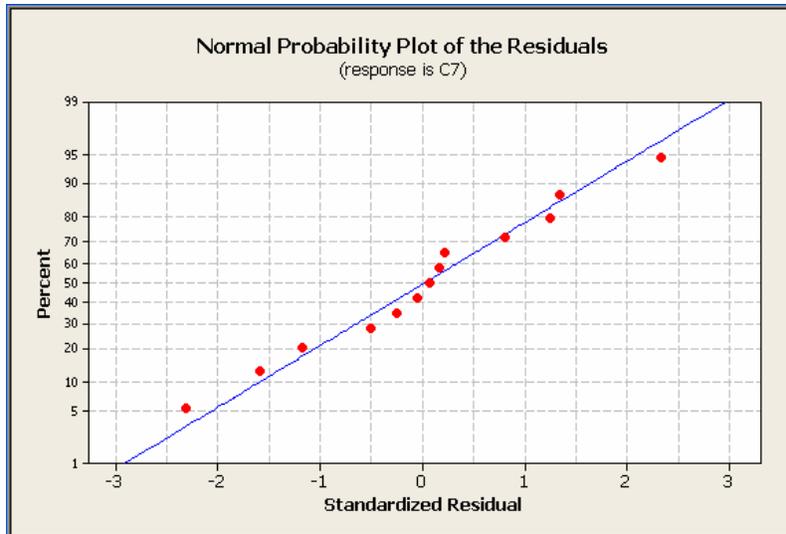
Figure 70: Normality Plot for Response (Droplet Volume)

Figures 71 and 72 show the Response Surface and Contour plots for the response (Droplet Volume). Figure 71 shows that response surface is a second-order model where the droplet volume peaks around 3000 picolitres. It is noted that as the frequency increases to 60 kHz the droplet volume decreases and vice versa. This is because at higher frequencies given that all the parameters remain constant there are higher numbers of drops being formed. As a result the resultant droplet volume per drop is reduced in proportion to the frequency of excitation.

It is also observed that at higher pressures the droplet volume increases assuming that frequency and voltage remain constant. This is because at higher pressure more fluid volume is discharged through the nozzle resulting in higher droplet volume per drop. Thus a combination of higher pressure and lower frequency results in a larger droplet volume.
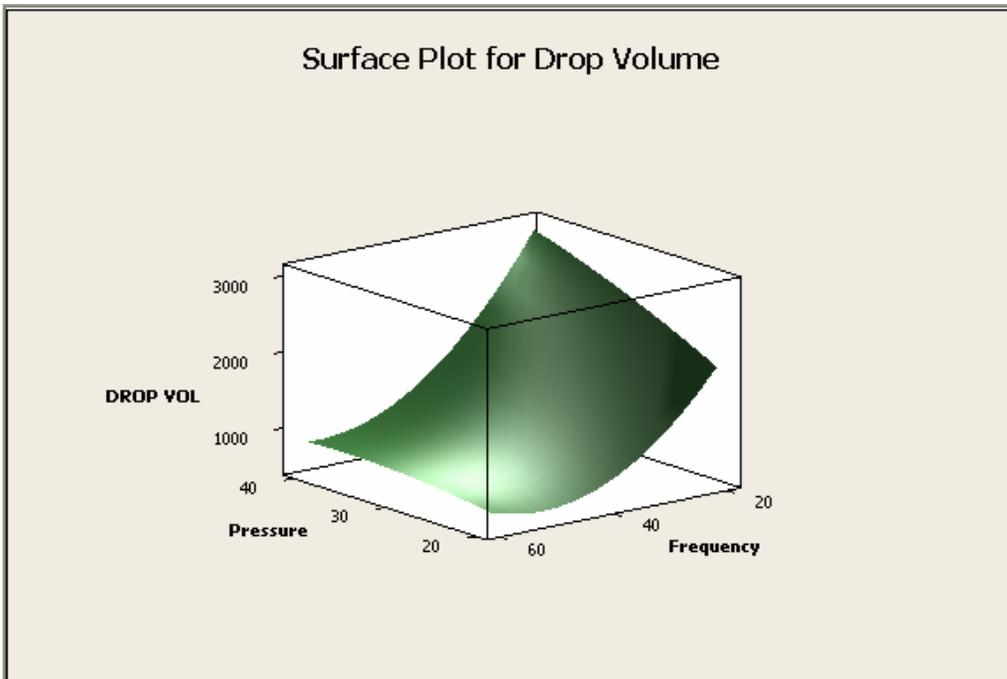
Figure 71: Response Surface Plot for Drop Volume
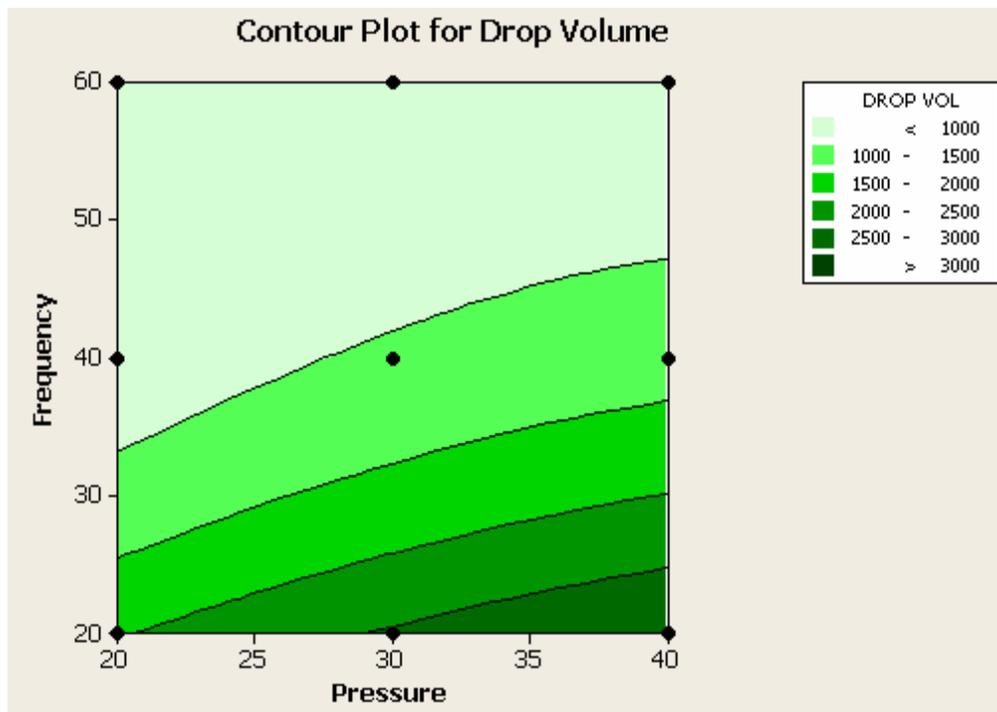
Figure 72: Contour Plot for Drop Volume

The contour plot shown in Figure 72 can be used to interpolate and optimize the droplet volume based on the input parameters. Equation 7.2 gives the droplet volume based on inlet Pressure and Frequency. Thus a researcher can select different levels of input settings along the contour line for Pressure and Frequency to obtain an optimal Droplet Volume. The concept of optimality is a subjective one based on the application area. For example, for semiconductor chip manufacturing the droplet volumes can be to the order of 10 picolitres while the droplet volume for building conductive traces can be to the order of 100 picolitres and higher depending on the trace width.

Drop Volume: DV in picolitres

$$DV = 2396.79 + (114.858*P) - (131.455*F) - (0.677135*P^2) + (1.5103*F^2) - (1.09505*P*F)$$

$$\ldots\ldots (7.2)$$

Where,

P: Pressure in psi

F: Frequency in kHz

8.0   CONCLUSIONS AND FUTURE DIRECTION

This dissertation researches the behavior of Nano-Particulate Fluid Jets (NPFJ) for building three-dimensional devices in free space. The major contribution of the current research is the investigation, development and optimization of the NPFJ. A detailed understanding of the interaction of different fields within the CIJ system is explored using numerical simulations.

A Coupled-Field Finite Element model of the piezoelectric disc explains its static and transient behavior. The Perturbation characteristics applied to different fluids is studied with a Multiphysics analysis. Finally, the CFD analysis conducted describes a thorough understanding of the transport phenomena associated with droplet formation. The parametric nature of all numerical models developed herein lends leverage to the researcher to predict the behavior of NPFJ with minimal modification to the base model.

The use of ultra-high speed photography has enabled the validation of the CFD results. It has complemented the CFD analysis in understanding the drop breakup phenomena. The design of experiments (DOE) conducted in this research have unfolded the relation between input parameters and output response such as drop volume, drop velocity and fluid jet breakup length. These relations are further explored with a Response Surface Methodology for obtaining an optimal drop volume. The significant factors that affect the drop volume are pressure and frequency of excitation. The research contributions from both the numerical simulations and experimental optimization of NPFJ have opened up knowledge that will assist in fine tuning proposed 3D printing technology. Researchers can dare attempt new NPFJ formulations and

study the droplet formation characteristics without expending valuable experimental resources. The hallmark of this research is that it enables the prediction of droplet characteristics for a multitude of fluids under varying input conditions, which is a critical component of the proposed 3D printing technology.

8.1   FUTURE DIRECTION

The numerical models developed in this dissertation can be extended to include the following:

- Modeling of new NPFJ formulations, which include bio-agents.

- Study of the satellite formations under wide range of input parameters. This topic is of interest to almost all inkjet researchers.

- Establish operating characteristics of a CIJ system

- Model the charge dynamics of the droplet in the flight tunnel and while passing through the deflector plates.

The above topics can be addressed through student theses and dissertations. Given the practical application of this work a collaborative industry initiative is expected.

BIBLIOGRAPHY

[1]   Madou, M. K., <u>Fundamentals of Microfabrication</u>, (New York: CRC Press, 1997), pp. 1-20.

[2]   Tang, W. C., DARPA MEMS Program, DARPA/MTO, January 2000.

[3]   MEMS Exchange

[4]   Laudon, M., and Romanowicz, B., <u>Technical Proceedings of the Fifth International Conference on Modeling and Simulation of Microsystems</u>, (Boston: Computational Publications, 2002), pp. 5

[5]   MEMS Exchange: Online source <u>http://www.memsnet.org/mems/</u>

[6]   Forschungszentrum Karlsruhe GmbH Technik and Umwelt, Projekt Mikrosystemtechnik (PMT).

[7]   Maluf, N., <u>An Introduction to Microelectromechanical Systems</u>, (Boston: Artech House Publishing, 2000), pp. 1-13.

[8]   Rai-Choudhury, P., "Chapter 5 – Photomask Fabrication Procedures and Limitations", <u>Handbook of Microlithography, Micromaching, & Microfabrication Vol. 1: Microlithography</u>, (Washington USA: SPIE Press), Vol. 1, 1997.

[9]   Fuller, S. B., Wilhelm, E. J., and Jacobson, J. M., "Ink-Jet Printed Nanoparticle Microelectromechanical Systems," <u>Journal of Microelectromechanical Systems</u>, Vol. 11, No. 1, February 2002, pp. 54-60.

[10]   Hadimioglu, B., Elrod, S., and Sprague, R., "Acoustic Ink Printing: An Application of Ultrasonics for Photographic Quality Printing At High Speed," <u>2001 IEEE Ultrasonics Symposium</u>, pp. 627-635.

[11]   Najafi, N., "MEMS Manufacturing Fabrication: Going Back to Basics", <u>Integrated Sensing Systems (ISSYS) Inc.</u>, Michigan, 2000.

[12]   Miami University, Oxford Ohio

[13]   Michalicek, M. A., "A Brief History and Overview of MEMS Technology and Applications" University of Colorado at Boulder, 2000.

[14]   Varadan, V. K., and Zoelzer, U., <u>RF MEMS and Their Applications</u>, (John Wiley and Sons, 2002)

[15]   Tang, C. W., "MEMS Program at DARPA", Microsystems Technology Office, DARPA, 2001

[16]   Le, H. P., "Progress and Trends in Ink-jet Printing Technology", <u>Recent Progresses in Inkjet Technologies II, The Society for Imaging Science and Technology</u>, 1999, pp. 1-14.

[17]   Jacobson, J. M., Hubert, B. N., Ridley, B., Nivi, B., and Fuller, S., "Nanoparticle-based electrical, chemical, and mechanical structures and methods of making same", <u>United States Patent: 6,294,401</u>, September 25, 2001.

[18]   Szczech, J. B., Megaridis, C. M., Gamota, D. R., and Zhang, J., "Fine-Line Conductor Manufacturing Using Drop-On-Demand PZT Printing Technology," <u>IEEE Transactions on Electronics Packaging Manufacturing</u>, Vol. 25, No. 1, January 2002, pp. 26-33.

[19]   Tseng, FG., Kim, CJ., and Ho, CM., "A Microinjetor Free of Satellite Drops and Characterization of the Ejected Droplets", <u>Symposium on Applications of Micro-Fabrication of Fluid Mechanics, ASME International Mechanical Engineering Congress and expositions 1998.</u>

[20]   Tseng, FG., Kim, CJ., and Ho, CM., "A High-Resolution High-Frequency Monolithic Top-Shooting Microinjector Free of Satellite Drops – Part II: Fabrication, Implementation, and Characterization", <u>IEEE Journal of Microelectromechanical Systems, Vol. 11, No. 5</u>, October 2002, pp. 437-447.

[21]   Garnier F., Hajlaoui, R., Yassar, A., Srivastava, P., "All-Polymer Field-Effect Transistor Realized by Printing Techniques", <u>Science Magazine</u>, Vol. 265, September 1994, pp. 1684-1686.

[22]   Ridley, B. A., Nivi, B., and Jacobson, J. M., "All Organic Field Effect Transistors Fabricated by Printing", <u>Science Magazine</u>, Vol. 286, October 1999, pp. 746-748.

[23]   Carr, W. W., Morris, J. F., Schork, F. J., and Tincher, W. C., "Textile Ink Jet Performance and Print Quality Fundamentals", <u>National Textile Center Annual Report: November 2001</u>.

[24]   Hayes, D. J., Wallace, D. B., and Cox, W. R., "Microjet Printing of Solder and Polymers for Multi-Chip Modules and Chip-Scale Packages", <u>IMAPS 1999</u>, MicroFab Technologies, Inc.

[25]   Shah, V. G., and Hayes, D. J., "Fabrication of Passive Elements using Ink-Jet Technology", <u>IMAPS ATW on Passive Integration</u>, MicroFab Technologies, Inc., June 2002

[26]   S. Li, S. Chen, Analytical analysis of a circular PZT actuator for valveless micropumps, Sensors and Actuators A 104 (2003) 151-161.

[27] L. L. Ries, S. W. Smith, Finite Element of a Deformable Array Transducer, IEEE Transactions on Ultrasonics, Ferroelectrics, and Frequency Control 46 (6) (1999) 1352-1363.

[28] C. J. Morris, F. K. Forster, Optimization of a circular piezoelectric bimorph for a micropump driver, J. Micromech. Microeng. 10 (2000) 459-465.

[29] Q. Li, M. Lovell, J. Mei, W. Clark, A study of displacement distribution in a piezoelectric heterogeneous bimorph, ASME, 2003.

[30] Y. Zhou, A coupled field analysis of an ink jet printhead with shear mode piezo transducer, Recent Progress in Inkjet Technologies II, Chap 3, Piezoelectrically Driven Ink Jet, 147-150.

[31] S. Jun, and Z. Zhaowei, Finite element analysis of a IBM suspension integrated with a PZT microactuator., Sensors and Actuators A 100 (2002) 257-263.

[32] Rayleigh, F. R. S., "On the Instability of Jets", Proceedings of the London Mathematical Society, 10 (4), 1878, pp. 4-13.

[33] Elmqvist, R., "Measuring Instrument of the Recording Type", U.S. Patent 2566443, (1951).

[34] Richards, J. R., Beris, A. N., and Lenhoff, A. M., "Steady Laminar Flow of Liquid-Liquid Jets at High Reynolds Numbers", Phys. Fluids A 5 (7), July 1993, American Institute of Physics, pp. 1703-1717.

[35] Deitz, D., "Connecting the Dots with CFD", Mechanical Engineering, March 1998.

[36] Yeh, JT., "A VOF-FEM and Coupled Inkjet Simulation", Proceedings of ASME Fluids Engineering Division Summer Meeting, New Orleans, 2001.

[37] Nichols, B. D., Hirt, C. W., and Hotchkiss, R. S., "Transient Fluid Flow Free Boundaries", Energy Science & Technology Software Center Software Abstract, Los Alamos National Laboratory, New Mexico, March 2002, pp. 1-3.

[38] Yatsuzuka, K., Saito, K, Asano, K., "Aero-Dynamical Motion of Charged Droplets Ejected from the 26μm Nozzle", IEEE Industry Applications Society Annual Meeting, New Orleans, October 1997, pp. 1845-1850

[39] Keur, R. I., and Stone, J. J., "Some Effects of Fluid Jet Dynamics on Ink Jet Printing", IEEE Transactions on Industry Applications Vol. IA-12, No. 1, January-February 1976, pp. 86-90.0

[40] Wnek, W. J., and Johnson, B. R., "Optimization of Ink-Jets Inks Using Nonlinear Programming", Recent Progress in Ink Jet Technologies II, Chap 4., pp 302-305.

[41] Kalaaji, A., Lopez, B., Soucemarianadin, A., and Attane, P., "Break-up of a Liquid Jet Induced by non-sinusoidal perturbations", <u>Recent Progress in Ink Jet Technologies II</u>, Chap 4., pp 223-227.

[42] Schneider, J. M., "Continuous Ink Jet Technology", <u>Recent Progresses in Inkjet Technologies II, The Society for Imaging Science and Technology</u>, 1999, pp. 246-251.

[43] Sweet, R. G., "High frequency recording with electrostatically deflected ink-jets", <u>Rev. Sci. Instrum</u>, 36, 1965 , pp.131.

[44] Sweet, R. G., "Signal Apparatus with Fluid Drop Recorder", <u>U.S. Patent 3596275</u>, (1971)

[45] Heston, S. F., "CIJ and Experimental Setup Schematics" University of Pittsburgh, Nov 2002

[46] 6000/6200 Series Ink Jet Printer LINX Service Manual, pp. 3.1-3.5

[47] ANSYS Inc, ANSYS Multiphysics/LS Dyna version 8.0.

[48] ANSYS Inc, Theory Reference, Chapter 11.2 Piezoelectrics

[49] Smits, J. G., Dalke, S. I., and Cooney, T. K., "The Constituent Equations of Piezoelectric Bimorphs", <u>Sensors and Actutators A,</u> 28, 1991, pp. 41-61

[50] www.efunda.com/materials/piezo/material_data/matdata_output.cfm?Material_ID=PZT-5A

[51] Morgan Electro Ceramics, PZT-5A Bimorph Disc

[52] ANSYS Inc, Structural Analysis Guide, Chapter 3.13.1 <u>Block Lanczos Method</u>

[53] Yatsuzuka, K., Saito, K, Asano, K., "Aero-Dynamical Motion of Charged Droplets Ejected from the 26μm Nozzle", <u>IEEE Industry Applications Society Annual Meeting, New Orleans,</u> October 1997, pp. 1845-1850

[54] ANSYS Inc, Coupled-Field Analysis Guide, Chapter 3. Fluid-Solid Interaction Solver

[55] ANSYS Inc, Fluid Analysis Guide, Chapter 2.3 Overview of a FLOTRAN analysis

[56] ANSYS Inc, Structural Analysis Guide

[57] ANSYS Inc, Element Reference Library

[58] Nichols, B. D., Hirt, C. W., and Hotchkiss, R. S., "Transient Fluid Flow Free Boundaries", <u>Energy Science & Technology Software Center Software Abstract, Los Alamos National Laboratory</u>, New Mexico, March 2002, pp. 1-3.

[59] ANSYS Inc, ANSYS Multiphysics/LS Dyna version 8.0.

[60] Morgan Electro Ceramics, PZT-5A Bimorph Disc

[61] Lee, E., <u>Microdrop Generation,</u> (CRC Press, 2003), pp 15-18.

[62] Lopez, B., Soucemarianadin, A., and Attane, P., "The Role of Nozzle Geometry on the Break-up of Liquid Jets", <u>Recent Progress in Ink Jet Technologies II</u>, Chap 4., pp 240-244.

[63] Fillmore, G. L., and Van Lokeren, D. C., <u>IEEE-IAS Conference Proceedings</u>, Oct 4-8, 1982

[64] Pierron, P., Normandin, M., Soucemarianadin, A., Clermont, J. R., and Attane, P., "Modeling of Liquid Jet Break-up and Drop Formation", <u>Recent Progress in Ink Jet Technologies II</u>, Chap 4., pp 218-222.

[65] Nakayama, Y., and Boucher, R. F., "Introduction to Fluid Mechanics", (New York: John Wiley & Sons, Inc., 1999), pp. 249-270.

[66] Palm, L., and Nilsson, J., "Impact of Droplet Placement on Paper by the Level of Droplet Flight Stability in a Continuous Ink Jet Printer", <u>Recent Progress in Ink Jet Technologies II</u>, Chap 4., pp 207-213.

[67] ANSYS Inc, Theory Reference, Fluid Flow, Chapter 7.3 - Volume of Fluid Method for Free Surface Flows.

[68] ANSYS Inc, Theory Reference, Fluid Flow, Chapter 7.3 – CLEAR-VOF Advection

[69] Brackbill, J.U., Kothe, D.B., and Zemach, C., "A Continuum Method for Modeling Surface Tension", <u>Journal of Computational Physics</u>, Vol. 100, pp. 335-354 (1992).

[70] Kothe, D.B. and Mjolsness, R.C., "RIPPLE: A New Model for Incompressible Flows with Free Surfaces", <u>AIAA Journal</u>, Vol. 30, pp. 2694-2700 (1992).

[71] Richards, J.R., Lenhoff, A.M., and Beris, A.N., "Dynamic Breakup of Liquid-Liquid Jets", Physics of Fluids, Vol. 8, pp. 2640-2655 (1994).

[72] Sasmal, G.P. and Hochstein, J.I., "Marangoni Convection with a Curved and Deforming Free Surface in a Cavity", <u>Transaction of ASME, Journal of Fluid Engineering</u>, Vol. 116, pp. 577-582 (1994).

[73] Wang, G., "Finite Element Simulations of Gas-Liquid Flows with Surface Tension", <u>Presented at the 2000 International Mechanical Engineering Congress and Exposition</u>, Orlando, FL (11/2000).

[74] Lovell, M. R., "Chapter 15: Arbitrary Lagrangian-Eulerian Formulation", <u>ANSYS Handbook version 7.0</u>, 2002.

[75] ANSYS Inc, Theory Reference, Fluid Flow, Chapter 7.4 – Fluid Solvers

[76] ANSYS Inc, Element Reference Library

[77]   Mei, J., Nano particulate fluid synthesizer, Department of Mechanical Engineering, University of Pittsburgh, 2004.

[78] Scott MacPherson, Swanson Center for Product Innovation (SCPI), University of Pittsburgh

[79] Heston Steve, Department of Mechanical Engineering, University of Pittsburgh

[80] Maina Joshua, Department of Electrical Engineering, University of Pittsburgh

[81] SENSICAM High Speed, CookeCorp Inc., Auburn Hills: Michigan, 2004, http://www.cookecorp.com/bioimaging.html

[82] http://www.opsci.com/index.asp?pagetitle=LensInfo&exten=asp&sku=oinf-kc-standard

[83] Lee, E., Microdrop generation, (Boca Raton, Fla.: CRC Press), 2003.

[84] ImageJ software, NIH, http://rsb.info.nih.gov/ij/index.html

[85] Maruschok, R., A System to Analyze Continuous Ink Jet Droplets, Masters thesis, Department of Electrical Engineering, University of Pittsburgh, 2004.

[86]   Walpole R. E., Myers, R. H., and Myers, S. L., Probability and Statistics for Engineers and Scientists, (New Jersey: Prentice Hall, Inc., 1998)

[87]   Walpole R. E., Myers, R. H., and Myers, S. L., Probability and Statistics for Engineers and Scientists, (New Jersey: Prentice Hall, Inc., 1998)

[88] Montgomery, D. C., Design and analysis of experiments, (New York : John Wiley & Sons, 1997)

[89] Myers, R. H., and Montgomery, D. C., Response surface methodology : process and product optimization using designed experiments, (New York : John Wiley & Sons, 20